Doctoral Dissertation

博士論文

Polarized view on protoplanetary disks: grain dynamics and alignment

（偏波観測を用いた原始惑星系円盤ダストの運動と整列過程の研究）

A Dissertation Submitted for the Degree of Doctor of Philosophy

December 2019

令和元年１２月博士（理学）申請

Department of Astronomy, Graduate School of Science,
The University of Tokyo
東京大学大学院理学系研究科
天文学専攻

Tomohiro Mori
森　智宏

Abstract

The study of planet/planetesimal formation has been attracted special interest for half a century to investigate how the solar system and exoplanets with various properties do form in our galaxy. The birthplace of planets or planetesimals is believed to be protoplanetary disks, which are inevitably formed as a consequence of the angular momentum conservation. To establish the formation scenario, a number of theoretical and observational works regarding the disk structure, dynamics, and grain properties have been conducted.

Theoretically, a plausible pathway of terrestrial planets or planetesimals is the collisional growth of dust grains in protoplanetary disks. However, there are several barriers, which prevents dust grains from growing into planetesimals: Dust grains that have nonzero electrical charge rarely stick to each other due to the repulsive force (charge barrier). Grain collisions do not lead to only grain growth but also rebounds or fragmentation (bouncing barrier and fragmentation barrier). Rapid inward drifting due to gas aerodynamic drag quickly removes the dust grains from the disks (Radial drift barrier). These barriers make the planetesimal formation scenario terrifically complicated.

Recent enhancements of observational quality in sensitivity and spatial resolution have provided us a wealth of information for disk structures and grain properties. One of the most crucial insights obtained on the observations is that disks commonly have substructures such as ring, gap, spiral and so on. These various structures possibly capture the critical step of planet formation and provide solutions to tackle the proposed barriers above. However, the formation mechanisms for such substructures are also highly uncertain. It is because they are thought to invoke complex and various physics regarding gas-grain interactions, which are tightly dependent on grain sizes. Thus, observational constraints on grain sizes and moreover grain dynamics are essential for better understandings of planetesimal formation.

To tackle the difficulties, we conduct continuum polarization observations at millimeter wavelengths of disks. The polarized emission is believed to originate from a combination of grain alignment and scattering. Previously proposed sources that can align grains in disks are magnetic fields, radiative gradients, and gas flow directed on grains. The thermal emission from elongated dust grains aligned with the sources can be observed as polarized emissions. The other mechanism, self-scattering, is scattering-induced polarization where dust grains of sizes comparable to the wavelengths scatter the thermal dust emissions. The relative importance of these processes is sensitive to grain sizes, shape and response to above external

forces acting on grains. This is invaluable information to explore the planetesimal formation. Nevertheless, it is largely unclear (1) which origin dominates, (2) whether just one or multiple origins contribute to the polarization and (3) how large and elongated the grains are. To address the questions, we investigate the origins of polarized emission detected on two disks around HL Tau and AS 209.

First, we conduct detailed modeling for the polarized emission of the HL Tau disk. Polarization features obtained on the HL Tau disk in Band 3 are as follows. (1) Elliptical polarization pattern and (2) uniform polarization fraction in the azimuthal directions. In previous studies, the origin of the polarization was concluded to originate from thermal emission of grains aligned by a radiative gradient in the disk (Kataoka et al., 2017; Stephens et al., 2017). However, Yang et al. (2019) pointed out that the radiative alignment predicts the circular pattern and strong polarization variations in the azimuthal directions, both of which are incompatible with (1) and (2). Alternatively, gas-flow alignment, where aspherical grains aligned by gas-flow with their long axes parallel to the flow, can produce the elliptical pattern. However, it also predicts strong azimuthal polarization variations, which is incompatible with (2). To solve the problem, we perform semi-analytical and radiative transfer modeling that includes the contributions from scattered emission as well as thermal emission of the aligned grains. As a result, we find that the combination of the gas-flow alignment and scattering can reproduce the features (1) and (2), whereas the radiative alignment + scattering cannot reproduce both the features. This result is surprising because the gas-flow alignment has been believed to occur when the velocity of the gas-flow on grains is supersonic while that in disks is subsonic. This raises a question regarding our understanding of alignment processes.

Next, we present 870 μm ALMA polarization observation toward the Class II protoplanetary disk around AS 209. We successfully detect the polarized emission and find that the polarization orientations and fractions have distinct characteristics between the inner and outer regions. In the inner region, the polarization orientations are parallel to the minor axis of the disk, which is consistent with the self-scattering model. This indicates the presence of an order of 100 micron-sized grains in the region. In the outer region, we detect $\sim$1.0% polarization and find that the polarization orientations are almost in the azimuthal directions. Moreover, the polarization orientations have systematic angular deviations from the azimuthal directions with $\Delta\theta \sim 4.^{\circ}5 \pm 1.^{\circ}6$. The pattern is consistent with a model that radially drifting dust grains are aligned by the gas flow against the dust grains. We consider possible scenarios of the grain dynamics at the AS 209 ring which can reproduce the polarization pattern. However, the directions of the observed angular deviations are opposite to what is predicted under the fact that the disk rotates clockwise. This poses a question in our understandings of the alignment processes and/or grain dynamics in protoplanetary disks.

Acknowledgement

First and foremost, I would like to express my sincere gratitude to my supervisor Prof. Takashi Miyata. He accepted my hope to move to the mid-infrared astronomy group from the doctoral course. His support and guidance to my study made my life in the graduate school fruitful and productive. He always took care of me and frequently gave me much advice for my works. I could not complete my Ph.D. study without his help. Someday, when I would become a person who leads a project, his kindness and frankness will remind me of how to build a good relationship with colleagues.

I would also like to express my special thanks to Akimasa Kataoka. As well as knowledge of planet formation theories, I learned a number of things from him such as how to conduct studies, how to appeal myself efficiently in presentations and papers, and desired attitude in studying something new. Through the discussion and conversation with him, I learned how to succeed and fail the projects. All of the things I learned from him will be helpful in the future works other than astronomy. When I was missed what I should do and how I conduct studies, he always encouraged me to overcome such tough situations. The more I thought that I was doing well, his advice became more serious while the more I encounter the tough situation, his advice became more thoughtful and helpful. Broken conversation with him always made me relaxed. The knowledge and experience obtained from him are so huge that I cannot write it all in the short sentences. In the future, I would like to become a scientist or engineer with his personality, which I would like to call "Kataoka-ism".

I am deeply grateful to the member of the mid-infrared astronomy group, Shigeyuki Sako, Takafumi Kamizuka, Ryou Ohsawa, Kentaro Asano, Masahito Uchiyama, Kenichi Tachibana. Regardless of the differences in the studying fields, they always cared about my works and provided me productive questions and suggestions. These are helpful to expand my knowledge and study. Takafumi Kamizuka frequently asked my studies with his wide interest in stellar astronomy. I also intensively worked with him about the instrumentation of the MIMIZUKU camera. He kindly told me how to operate MIMIZUKU and to conduct the experiments for the optics. When we visited Hawaii several times, he leads the laboratory experiments and engineering observations. I learned a lot through the invaluable experiences and his skill and leadership. Ryou Ohsawa was near my desk and gave me fundamental questions and advice when I interrupted his work and presented my latest results. I also felt happy to conduct the detector tests with Shigeyuki Sako when we encountered the unexpected noise of the Aquarius detector in Hawaii. He also invited me to the workshop of Tomo-e Gozen in Kiso,

Nagano, encouraging me to discuss many astronomers working on the time-domain astronomy.

I also thank members of the laboratory building in IoA, Kentaro Motohara, Konishi Masahiro, Yarunori Terao, Kosuke Kushibiki, Jin Beniyama, Aiko Masuhara, and Natsuko Kato. Daily conversations during lunch or breaking time made me feel comfortable in my studying time. I sometimes played basketball with Kosuke Kushibiki, Jin Beniyama, and Yasunori Terao and I was refreshed.

At last, a special thanks to my family. In particular, I am very grateful to my parents Takashi and Junko, for your devoted support, uninterrupted assistance, powerful encouragement, and supportive care; to my little sister, Keiko for inspiring me and making me motivated to be self-disciplined.

For the rest of my life, I hope to create something new, which contributes to society and the lives of human beings by continuously improving myself as a scientist and, more importantly, as a man. Hopefully, my experiences of the study in astronomy would make me a scientist or engineer who can capture the essence of phenomena, where complex physics appears to be underlying. If I would encounter tough situations, I would like to overcome them by steadily performing works to do while I would never forget the huge scale mind learned from the astronomy.

Tomohiro Mori

Department of Astronomy
Graduate school of Science
The University of Tokyo

December 2019

Contents

Chapter 1

Introduction

The study of planet formation is one of the most important fields in modern astronomy. Not only does the study answer the origin of the Solar system, but it also provides a clue to investigate how a number of detected exoplanets with various properties are created. The site of planet formation is thought to be protoplanetary disks, which are inevitably formed as secondary products in star formation processes. The disks comprise gas and a small fraction of dust grains. The dust grains coagulate to form larger and larger aggregates, evolving into planets and planetesimals. The coagulation process is tightly linked to physical processes driving in the disks. Thus, it is essential to clarify the physical processes driving in the protoplanetary disks with both theoretical and observational points of view.

For the past half a century, a number of observational and theoretical studies for protoplanetary disks have brought us a wealth of knowledge about star and planet formation processes. Especially these days, living in the ALMA era, the amount of knowledge has been dramatically increasing owing to the high sensitivity and high spatial resolution of the instrument. At the same time, however, the increase of studies motivated by ALMA also provides us a lot of pivotal questions, which complicate current understandings of planet formation processes.

This study aims at investigating the grain coagulation processes with millimeter-wave polarization observations for the two protoplanetary disks around AS 209 and HL Tau. First, in this chapter, we provide a review of previously obtained knowledge of protoplanetary disks from observational and theoretical studies to explain the background of this study. Then, we provide the results of our study in consecutive chapters 2 and 3. In chapter 2, we present a new 870 μm ALMA polarization observation toward the protoplanetary disk around AS 209 and the results of detailed analysis for the data. In chapter 3, we conduct semi-analytical and radiative transfer modeling for a 3 mm polarization observation toward the HL Tau disk. Finally, we summarize our studies and prospects in chapter 4.

1.1 Outlines of Protoplanetary Disks

To know planetesimal formation scenarios and their difficulties, the knowledge of protoplanetary disks, in which planets and planetesimals are thought

to be formed, is essential. In this section, we introduce (1) what protoplanetary disks are, (2) how they form, evolve and dissipate, (3) their properties (structure, radius, mass and so on) inferred from theories and observations. In subsection 1.1.1, we briefly review the lives of protoplanetary disks. In subsection 1.1.2, we introduce the classical scheme to classify the evolution stage of protoplanetary disks and YSOs based on spectra in optical−infrared wavelengths. in subsection 1.1.3 and 1.1.4, we describe the properties of protoplanetary disks such as geometrical structure and temperature distribution based on theories. We also describe how protoplanetary disks can be observed in multi-wavelengths in subsection 2.1.5. Finally, we introduce observational constrains on basic parameters of the disks in subsection 2.1.6.

1.1.1 Formation, Evolution, and Dissipation of Protoplanetary Disks

We introduce standard scenarios formation, evolution, and dissipation of protoplanetary disks. Because disk formation takes place at collapsing star-forming clouds to form protostars, we briefly describe how star formation occurs at first. Note that this review focuses on low-mass star formation, whose general formation scenario has been already established in comparison to that of a high-mass star.

The processes of star formation involve a variety of size scales. Because of such an extraordinary dynamic range in size scales, there are many physical processes that operate during the star formation. The interstellar medium is composed of gas and dust grains. The typical number density of the gas, which is predominantly neutral hydrogen and helium, is $n_H \sim 1$ cm^{-3}. The dust grains have a typical size of $\sim$0.1 μm and account for 1% mass compared to the gas. The site of star formation is the denser region that is called molecular clouds, where hydrogen is nearly all in the molecular form with the number density of $n_{H_2} \sim 10^4$−10^7 cm^{-3}. The internal structures of molecular clouds are hierarchical, consisting of filamentary or clumpy structures on a wide range of scales. Molecular cloud cores are the densest parts of the interstellar medium with the typical spatial scale of $\sim$0.1 pc and the mass of $\sim 1\ M_\odot$, which are believed to be embryos of individual stars or clusters. The cores are in hydrostatic equilibrium, where internal thermal pressure resists their self-gravity. The densities of gas and grains so high that cores are highly opaque to visible light and are identified as silhouettes against the bright background stars in the optical wavelength (Bok, 1948; Bok, Cordwell, and Cromwell, 1971; Alves, Lada, and Lada, 2001).

The process of star formation starts with the gravitational collapse of molecular cloud cores (Larson, 1969). Initially, gas and dust grains fall onto a point source to form a protostar. As the collapse proceeds, the centrifugal force gets to resist the gravity as a result of the conservation of the angular momentum, leading to form a rotationally-supported disk surrounding a protostar. The disks, which are referred to as protoplanetary disks, are composed of gas and a small fraction of dust grains and are believed to be the birthplace of planets or planetesimals.

The temporal evolution of protoplanetary disks is driven by various and complex physics, which causes disk dispersal from optically thick to optically thin. Most basic physics is outward transport of the angular momentum of the gas, which is induced by gas viscosity (Hartmann et al., 1998; Balbus and Hawley, 1991). The transport of the angular momentum induces the accretion onto a protostar from the inner disks. In parallel, the materials from the outer regions resupply the inner disks, spreading as the angular momentum is transported outward. The origin of the viscosity is thought to be a turbulent motion of the gas. The dominant process to the turbulence is magnetorotational instability (MRI), which is induced by interactions between gas and magnetic fields threatening disks (Gammie, Shapiro, and McKinney, 2004).

Outflows of the gas and grains are also one of the main mechanisms, by which the gaseous disks deplete their mass. Many observational studies have revealed the presence of the outflows in many YSOs in both the class I and II phases (Zapata et al., 2012; Zapata et al., 2015a; Zapata et al., 2015b; Lumbreras and Zapata, 2014). The physical mechanisms to produce the flow is still unclear and being debated, and depends on the evolution phases. One of the possible sources are photoevaporation (Hollenbach et al., 1994; Alexander, Clarke, and Pringle, 2006a; Alexander, Clarke, and Pringle, 2006b; Owen et al., 2010; Gorti and Hollenbach, 2009; Gorti, Dullemond, and Hollenbach, 2009). In the model, far-ultraviolet (FUV) photons from the stars ionize and heat the circumstellar hydrogen to $\sim 10^4$ K. As a result, the thermal velocity of the heated gas exceeds the escape velocity and are dissipated in the form of a wind. Magnetohydrodynamical (MHD) driven wind is also responsible for the gas dynamics (Blandford and Payne, 1982; Kudoh and Shibata, 1997; Ferreira, Dougados, and Cabrit, 2006; Suzuki and Inutsuka, 2014).

The dynamics of solid particles also play a crucial role in the evolution processes. The dynamics of the dust grains are sensitive to the grain size. The initial tiny particles with ~ 0.1 μm in the radius are tightly coupled to gas and follow the gas motions. As the grain growth proceeds, however, they start to decouple to the gas. This decoupling can lead to collisional grain growth or fragmentation and rapid inward drifting, each of which is of importance to discuss the planetesimal formation theories. We will discuss the grain motion in detail in the next section.

The accretion, outflow, and coagulation of grains explained above lead to depletion of the materials in protoplanetary disks, eventually leaving a star and planetary systems. The disk dissipation timescale is inferred primarily by the infrared emission, which is emitted by the dust grains in the inner regions of disks as will explain below. Haisch, Lada, and Lada (2001) and Hillenbrand (2005) have investigated how the occurrence of the near-infrared excess varies with the mean ages of stellar clusters and found that the occurrence steadily decreases from < 1 to ~ 10 Myr. The occurrence of the near-infrared excess is consistent with median disk lifetimes of $\sim 2-3$ Myr. Other studies that rely on longer wavelengths observations from mid-infrared to millimeter-wave derive similar results (Gutermuth et al., 2008; Winston et al., 2007; Lada et al., 2006; Sung, Stauffer, and Bessell, 2009; Hernández et al., 2007; Sicilia-Aguilar et al., 2006; Andre and Montmerle, 1994; Andrews

and Williams, 2005; Andrews and Williams, 2007). As well as solid components, the gas dissipation timescale was also inferred by accretion signatures and found to be the analogous situation to that of the dust dissipation (Fedele et al., 2010). Theoretically, the combination of viscous accretion and photoevaporation models can roughly reproduce the observed disk population explained above (Hollenbach et al., 1994; Gorti and Hollenbach, 2009; Gorti, Dullemond, and Hollenbach, 2009); however, the evolutionary pathways of disks are highly uncertain because there are a number of physical processes are believed to be involved.

1.1.2 Classification of YSOs

Spectral Energy Distribution (SED) enables us to indirectly probe the spatial distribution of dust grains in disks. Lada, Margulis, and Dearborn (1984) has classified the shape of SEDs of YSOs in Ophiuchus star forming region into 3 distinct groups based on whether the excess is rising in mid-infrared, declining but with still excess in longer wavelength, or with almost no excess emission. Subsequently, Lada, Margulis, and Dearborn (1984) and Greene et al. (1994) introduced a classification of the SEDs, in which the YSOs are divided into four classes 0, I, II and III based on the slope of the SEDs in the infrared region. To denote the slope, they defined a parameter α_{IR} as given by

$$\alpha_{IR} = \frac{dlog\nu F_\nu}{dlog\nu} = \frac{dlog\lambda F_\lambda}{dlog\lambda}. \tag{1.1}$$

Conventionally, α_{IR} is measured by fitting SEDs from near-infrared to mid-infrared that is specifically, from 2.2 μm to 10 or 24 μm. Although the boundary of α_{IR} to divide the YSOs, typical classification is described as follows.

Class 0: A protostar is deeply embedded by a surrounding envelope. The emission from a star and circumstellar disk cannot be observed; instead, that from an envelope is observed from far-infrared to millimeter wavelengths.

Class I: Infrared emission is partially transparent and is rising from near- to mid-infrared with $\alpha_{IR} > 0-0.3$. In this phase, a protostar and disk are still almost entirely invisible although strong outflow from a star partially clears an envelope along a direction perpendicular to a disk.

Class II: The emission from a protostar and disk first becomes optically visible. The infrared excess is declining from near- to mid-infrared with the slope of -1.6 $\leq \alpha_{IR} \leq$ -0.3.

Class III: The disk is entirely dispersed by some mechanism, the emission comes from only a stellar photosphere. The slope α_{IR} equals to stellar spectra

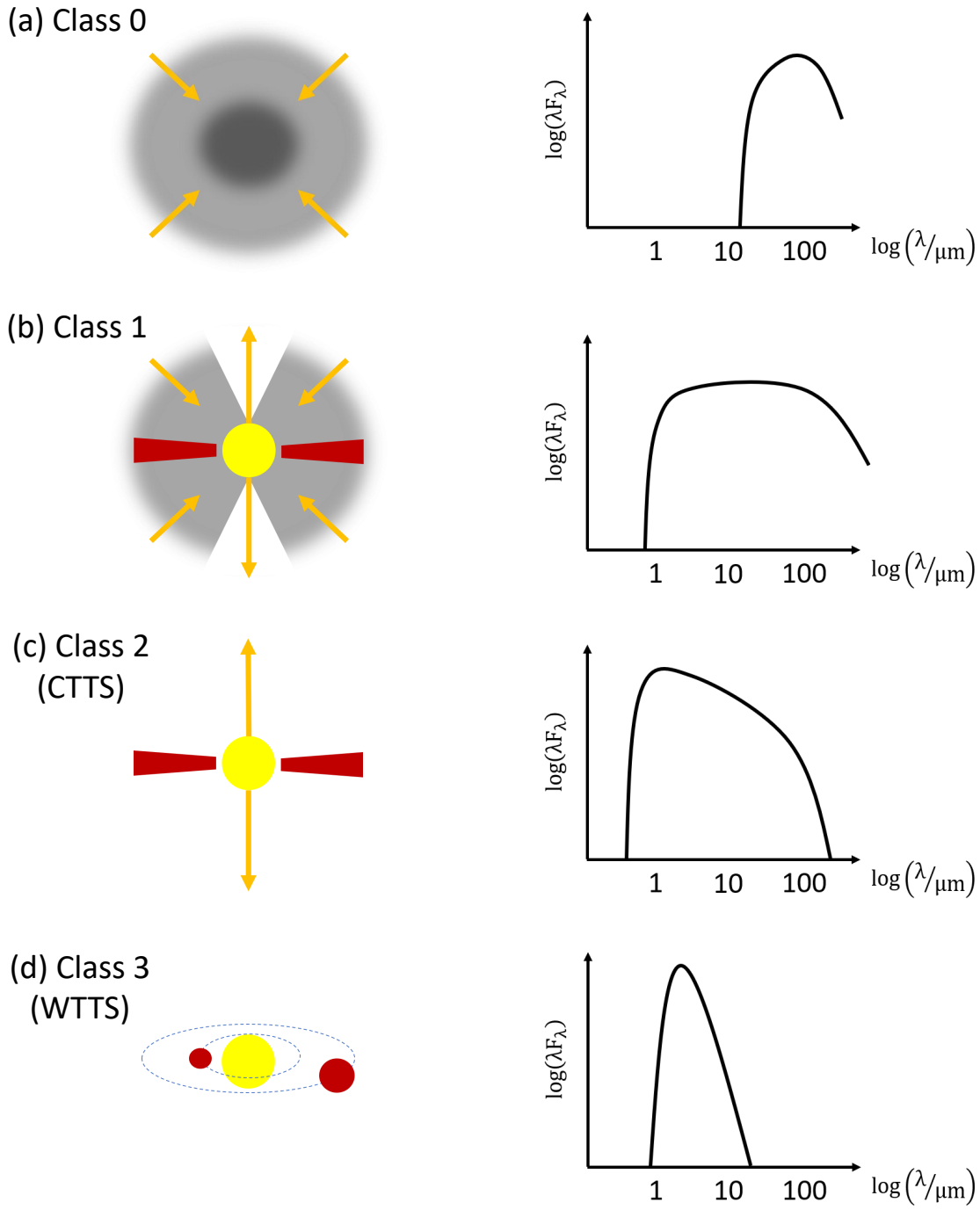

FIGURE 1.1: Classification for Young stellar objects based on the colors in the infrared regions. The left column shows the schematic illustrations depicting the state in each class and the right column shows the corresponding SEDs.

with $\alpha_{IR} <$ -1.6.

In parallel, there is another classification that defines the evolutionary state of central stars based on accretion signatures. A central protostar is fed disk materials by accretion. The accreting materials, which falls onto the star with nearly free-fall velocity, induce a shock on the stellar photosphere, leading to strong ultraviolet or hydrogen recombination lines like Hα. The classification scheme is based on the equivalent width of Hα. Classical T Tauri stars (CTTS) show strong accretion signatures with the Hα equivalent width of $W_{H\alpha} > 10$ Å, whereas Week-lined T Tauri stars (WTTS) show no or only subtle accretion indications.

1.1.3 Spatial Structure of Protoplanetary Disks

To create a model, which describes the spatial distribution of gas and grains in protoplanetary disks, it is reasonable to consider the required materials to form our Solar system. Based on the idea, Kusaka, Nakano, and Hayashi (1970), Weidenschilling (1977b), and Hayashi (1981) have developed the Minimum Mass Solar Nebula (MMSN) model to derive a lower limit of the required materials that have been present in the Solar system. In that model, inferred masses of heavy elements of each planets are divided and distributed to derive the smooth density profile. The amount of gas (Hydrogen and Helium) is derived based on the solar abundance. Following the scheme, the derived surface density scales as $\Sigma \propto r^{-3/2}$. Because there is uncertainties in the amount of the heavy elements, normalization to the profile is somewhat arbitrary, but commonly used profile is given by

$$\Sigma_g(r) = 1.7 \times 10^3 \left(\frac{r}{1\mathrm{AU}}\right)^{-3/2} \quad \mathrm{g\,cm^{-2}}, \tag{1.2}$$

for the gaseous components, and

$$\Sigma_d(r) = 7.1 \left(\frac{r}{1\,\mathrm{AU}}\right)^{-3/2} \quad \mathrm{g\,cm^{-2}} \quad \text{for r} < 2.7\,\mathrm{AU}, \tag{1.3}$$

$$\Sigma_d(r) = 30 \left(\frac{r}{1\,\mathrm{AU}}\right)^{-3/2} \quad \mathrm{g\,cm^{-2}} \quad \text{for r} > 2.7\,\mathrm{AU}, \tag{1.4}$$

for the solid components. The profiles are presented in Figure 1.2. The jump in the density profile for the solid components is due to the presence of icy materials, which appear outside the snowline (r = 2.7 au). Integration of Equation 1.2 out to 30 au yields with the enclosed mass of 0.01 $M_\odot$, which is roughly consistent with mass measured by observations.

Theoretically, the radial structure of accretion disks can be derived by assuming a balance of the viscous and the gravitational torques (Lin and Papaloizou, 1980; Ruden and Lin, 1986; Ruden and Pollack, 1991; Stepinski, 1998). The radial profile of gas surface density can be solved by the

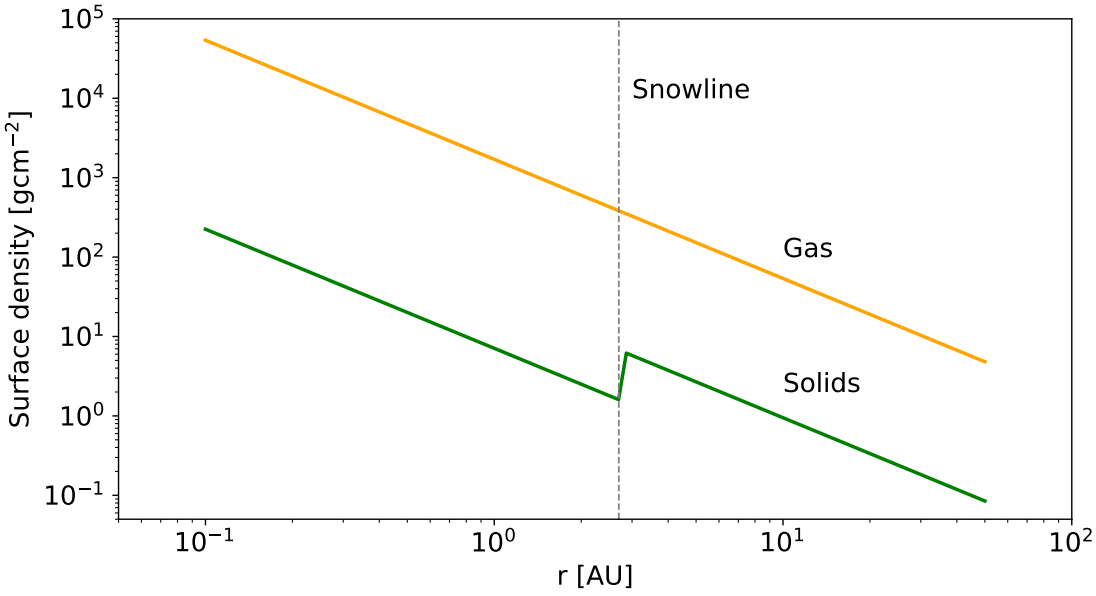

FIGURE 1.2: The surface density profiles of gas and solids in the minimum mass solar nebula (MMSN) model (Hayashi, 1981). The location of the snowline is also indicated with the gray dashed line.

viscous diffusion equation (Lynden-Bell and Pringle, 1974). One of the analytical solution was derived by (Shakura and Sunyaev, 1973) as given by

$$\Sigma(r) = \Sigma_0 \left(\frac{r}{r_c}\right)^{-\gamma} \exp\left[-\left(\frac{r}{r_c}\right)^{2-\gamma}\right], \tag{1.5}$$

where r_c is characteristic radius, from which the surface density exponentially decreases, Σ_0 is surface density at r_c. To first order, the surface density profile of dust grains are assumed to follow that of the gaseous components, although the recent high resolution observations have found distinctive distributions of the two components.

Protoplanetary disks are flared with a vertical scale height that increases with radius there are a certain extent in the vertical directions. The vertical extent for gas is inferred by assuming that the disk is vertical hydrostatic equilibrium,

$$\frac{\partial P}{\partial z} = -\rho g_z, \tag{1.6}$$

where P is the gas pressure and g_z is the gravitational acceleration in z-component. Assuming the ideal gas equation of state, Equation 1.6 is rewritten by

$$\frac{\partial \ln \rho}{\partial z} = -\left[\frac{\mu m_p}{kT}\frac{GM_* z}{(r^2+z^2)^{3/2}} + \frac{\partial \ln T}{\partial z}\right], \tag{1.7}$$

where G is the gravitational constant, μ is the mean molecular weight, m_p is the mass of the proton, and k is the Boltzmann constant. The solution of ρ can be derived by assuming geometrically thin extent ($z \ll r$) with a small

temperature gradient ($\partial T/\partial z \sim 0$) as follows,

$$\rho(z) = \frac{\Sigma}{\sqrt{2\pi}H} \exp\Big[-\frac{1}{2}\Big(\frac{z}{H}\Big)^2\Big], \tag{1.8}$$

where H is the gas scale height, which is the length scale by which the density decreases to 1/e from the midplane of disks, which is given by

$$H = \frac{c_s}{\Omega_K} = \Big(\frac{kT}{\mu m_H}\frac{r^3}{GM_*}\Big)^{1/2}, \tag{1.9}$$

where c_s denotes the sound speed and Ω_K is the Keplerian angular velocity.

1.1.4 Temperature Distribution

The temperature of the solid components in disks are different in location to location. In the surface layer of disks, dust grains are directly exposed to stellar irradiation. The absorbed starlight in the ultraviolet to optical wavelengths is re-radiated out to space and deeper into the disk structure. The dust grains are in thermodynamic equilibrium, where the irradiation heating and re-radiation cooling is in balance, as written by

$$\frac{L_*}{4\pi r^2}\pi a^2 = 4\pi a^2 \sigma_{SB} T_s^4 \epsilon, \tag{1.10}$$

where L_* is the stellar luminosity, r is the distance, a is the grain radius, T_s is grain temperature, σ_{SB} is the Stefan-Boltzmann constant and ϵ is the grain emissivity. The grain temperature is derived with Equation 1.10 as

$$T_s = 280\Big(\frac{r}{1\mathrm{AU}}\Big)^{-1/2}\Big(\frac{L_*}{L_\odot}\Big)^{1/4}, \Big(\frac{\epsilon_{opt}}{\epsilon}\Big)^{1/4}\mathrm{K} \tag{1.11}$$

where ϵ_{opt} is the emissivity at the optical wavelength.

In the midplane, on the other hand, the disk is so opaque to starlight that the temperature is not determined as in the surface layers. Instead, part of the thermal emission from the grains in the upper surface layers heats the grains in the midplane. This results in a vertical temperature gradient, where T increases with z (Chiang and Goldreich, 1997; Chiang et al., 2001).

Gas temperature is not necessarily identical to that of dust grains and highly sensitive to gas density and radiation field of ultraviolet stellar light. In the midplane of disks, the gas number density is high enough to frequently collide with the grains in the disks. This leads to thermal coupling between the gas and grains and results in the common temperature of the two components.

In the upper layer of the disks, however, the gas number density sharply drops and the frequency of the collision with grains also decreases. As a result, the energy exchange between gas and grains through the collisions becomes insufficient, leading to thermal decoupling. Thus, other processes that determine the temperature are involved in the surface layer. One of the

dominant heating sources is photoelectric heating, where the stellar ultraviolet photons eject electrons from uncharged grains to heat the gas. The dominant coolant is typically CO, which is the most abundant molecule that has a permanent electric dipole and hence efficiently radiates. The temperature in the surface layers is determined by the balance between these heating and cooling.

1.1.5 Observational Appearance of Protoplanetary Disks

To review the observational constraints on the disk structure and mass, it is useful to describe how the disks with the explained structures, mass and temperature can be measured with the multiwavelength observations. Thus, we quickly introduce the principles in the following.

Thermal and Scattered emission from dust grains:
The main contributors to the continuum emission from disks are thermal and scattered emission. The specific intensity at frequency ν along a direction of line of sight s is derived with the radiative transfer equation,

$$dI_\nu = \rho\kappa_\nu(S_\nu - I_\nu)ds, \tag{1.12}$$

where ρ is the density of dust grains, κ_ν is the opacity considering both the absorption and scattering, and S_ν is the source function. If we assume that (1) the scattered emission is negligible compared to the thermal emission and can be neglected, (2) the grains are in thermodynamic equilibrium ($S_\nu = B_\nu(T)$), and (3) the temperature is constant along the line of sight (applicable condition for geometrically thin disks), the specific intensity I_ν is derived as follows,

$$I_\nu = B_\nu(T)(1 - e^{-\tau_\nu}) \tag{1.13}$$

This indicates that the optically thick emission ($\tau_\nu \gg 1$) is identical to the blackbody ($I_\nu = B_\nu(T)$) coming from $\tau = 1$ surface, while the optically thin emission ($\tau_\nu \ll 1$) is a product of thermal blackbody and optical depth ($I_\nu = \tau_\nu B_\nu(T)$).

The principal above suggests that the excess emission in the SEDs are composed of multiple temperature components. The thermal emission in the near-infrared ($2-5$ μm) originates from the hottest solids in the innermost regions of the disks. Because the density is high and the emission is optically thick in the regions, the flux density in the SEDs is sensitive to the temperature and area of emitting regions. As explained in subsection 2.1.4, the temperature decreases with the distance and thus the emission at the longer wavelengths comes from the outer regions of the disks. Because the mid-infrared emission ($5-20$ μm) is still optically thick, it traces the layer on a few au scales. Far-infrared emission is partially optically thin and probes colder grains near the midplane in the outer disks ($\sim$tens of au). (Sub)millimeter emission can access the cold solids in the midplane, although optically thick emission still partially remains.

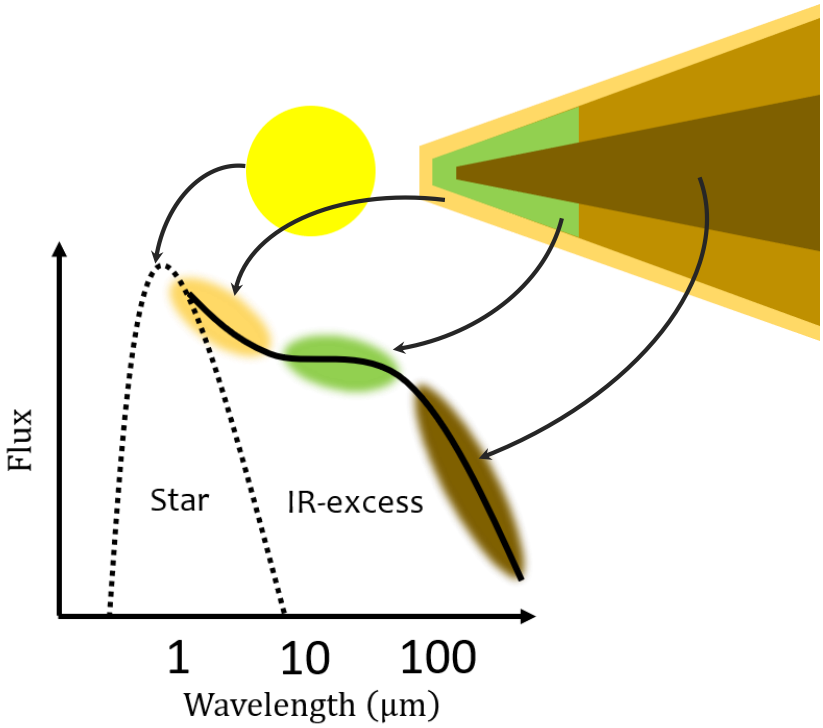

FIGURE 1.3: Schematic illustrations of protoplanetary disks and typical SED. The emitting regions of infrared excess at infrared to millimeter wavelengths are indicated with the arrows

Scattered emission also contributes to the observed emission in the wide wavelength range. The small ($\sim\mu$m) grains in the upper layer of the disks effectively scatter the incoming radiation whose wavelengths are comparable to grain sizes. Thus, the scattered emission in the optical to near-infrared probes the scattering grains near the surface layer. The scattered emission in longer wavelengths has believed to be negligible especially at (sub)millimeter wavelengths. It is because that stellar radiation to be scattered is subtle in the wavelengths. However, a recent study showed that the thermal emission of dust grains can be scattered and polarized when some conditions are satisfied (Kataoka et al., 2015). We will explain the mechanism in section 2.4.

Emission from Gaseous disks:
Gas observations are essential to probe not only the structures but also the dynamics of gaseous disks. Although the dominant constituent of gaseous disks is atomic hydrogen, it rarely emits by itself because it does not have the permanent electric dipole. Instead, the studies of gaseous disks often rely on observations of CO isotopologues at millimeter wavelengths (e.g. Dartois, Dutrey, and Guilloteau, 2003; Rosenfeld et al., 2013a; Williams and Best, 2014; Miotello et al., 2016; Miotello et al., 2017; Miotello et al., 2018). Their abundance is sensitive to the temperature of the gaseous components. The molecules in the uppermost layers are photodissociated by the strong UV radiation while they are frozen out in the cold midplane (Aikawa et

al., 2002). Thus, the molecules are thought to be abundant in the warm layer, where photodissociation and frozen-out are avoided. Not only the CO molecules, but various molecules are used to probe the other regions of disks such as N_2H, HCO^+, and so on (see Figure 1 in Öberg et al. (2011)).

1.1.6 Observational Constraints on the Structure, Radius, Mass, and Grain Size

Based on the theories described above, we review constraints on the basic parameters of the disks (structure, radius, and mass) obtained on previous multiband observations.

Disk structure and radial/vertical extent:
Resolved continuum observations at millimeter wavelengths enable to directly constrain the disk structures. As is explained in subsection 1.1.5, the emission is optically thin, and thus traces the surface density of dust grains. Surface density profile is derived for disks in the nearest stellar clusters such as Taurus (Isella, Carpenter, and Sargent, 2009; Isella, Carpenter, and Sargent, 2010; Piétu et al., 2006; Piétu et al., 2014; Guilloteau et al., 2011) and Ophiuchus (Andrews et al., 2009; Andrews et al., 2010). With these observations, the exponent of the surface density profile γ is derived to be $\gamma \approx 0-1$, which is shallower than that of that Hayashi model (γ = 1.5), and the characteristic radius (r_c) of $r_c \approx 5-200$ au. Note that the substantial diversity of the presented values partially comes from different modeling approaches between the studies.

The aspect ratio of solid components is inferred by scattered light images obtained at primarily optical and near-infrared. The images are modeled with Equation 1.8 to derive $H/r \approx 0.1-0.2$ with a small radial dependence $\propto r^{0.05}$ (e.g. Avenhaus et al., 2018).

Mass:
Since the millimeter continuum emission probes the density of solid particles, the mass of dust disks M_{dust} also can be measured by the integrated flux at millimeter wavelengths as

$$M_{dust} = \frac{F_\nu d^2}{\kappa_\nu B_\nu(T)}, \tag{1.14}$$

where d is the distance to the source, F_ν the flux density. The many disks in the nearby star clusters were measured based on the principles (Andrews et al., 2009; Andrews et al., 2013; Lee, Williams, and Cieza, 2011; Williams et al., 2013; Carpenter, Ricci, and Isella, 2014; Ansdell, Williams, and Cieza, 2015; Ansdell et al., 2016; Ansdell et al., 2017). A near-complete imaging survey toward the Lupus and Taurus star-forming region, both of which have similar ages ($\sim$1$-$2 Myr), revealed that the mean dust mass in Taurus and Lupus is $15 \pm 3\ M_\oplus$ and $15 \pm 2\ M_\oplus$, respectively (Andrews et al., 2013; Ansdell et al., 2016). On the other hand, Upper sco, whose age is older than the two

regions ($\sim$5$-$10 Myr), has the mean dust mass of $5 \pm 3\ M_{\oplus}$, which is significantly 3 times lower than that of the younger clusters, indicating that the disk clearing proceeds with time (Barenfeld et al., 2016).

Directly measuring the gas content in disks is still challenging because atomic hydrogen H rarely emits by itself. Instead, observations of CO lines enable us to infer the gas mass by assuming ISM-like [CO]/[H_2] abundance. Recent high sensitivity observations using ALMA enable to conduct synthetic studies for disks in various clusters as was done for dust content. Ansdell et al. (2016) conducted ^{13}CO and C^{18}O line survey for class II disks in the Lupus star-forming region and constrained the gas content to roughly a Jupiter mass, which is significantly lower than that of the MMSN model.

Grain size:
As indicated above, the spectral indices $\alpha_{mm} = 2 + \beta$ provide basic tool to constrain the grain sizes in disks. In the last two decades, unresolved photometric observations at millimeter wavelengths showed that β in disks is $\beta \approx 0.5-1$ (e.g. Beckwith and Sargent, 1991; Mannings and Emerson, 1994; Wilner et al., 2000; Testi et al., 2001; Testi et al., 2003; Natta et al., 2004; Wilner et al., 2005; Andrews and Williams, 2005; Rodmann et al., 2006; Ricci et al., 2010), which is significantly lower than that in the ISM $\beta_{ISM} \approx 1.7$ (Li and Draine, 2001). This decrease is explained best by the presence of larger grain in disks relative to that in the ISM (Miyake and Nakagawa, 1993; Draine, 2006; Natta et al., 2007).

The interpretation of β values needs to be taken with some caution because local optically thick emission can contribute to the total emission in such unresolved observations, which can impact on the grain size measurement (Ricci et al., 2012). Thus, it is crucial to spatially resolve disks to avoid the optically thick components. The radially resolved multiband images revealed that the β profile shows radial gradients for several disks, suggesting radius-dependent grain sizes (Pérez et al., 2012; Carrasco-González et al., 2016; Tazzari et al., 2016; Tsukagoshi et al., 2016; Dent et al., 2019). Moreover, recent observations reported anomalously low β at 0 or even lower (Carrasco-González et al., 2016; Tsukagoshi et al., 2016; Liu et al., 2017; Huang et al., 2018a; Dent et al., 2019). Although the origin of such shallow slopes is debated, Liu (2019) and Zhu et al. (2019) pointed out that the inclusion of scattered emission can make the emission fainter, resulting in the low α and β.

The modeling studies for obtained α revealed that the low α can be reproduced if maximum grain sizes a_{max} in a power-law distribution are in $\sim$mm or cm ranges (Draine, 2006; Natta et al., 2007). However, one problem is that the relationship between α and a_{max} is not necessarily unique because derivations of specific a_{max} are highly sensitive to the assumptions on grain composition, shape, and internal density (Pollack et al., 1994; Min, Hovenier, and de Koter, 2005), all of which are poorly constrained yet. This uncertainty has been identified as a difficult task, which prevents us from precisely constraining the grain sizes in disks.

1.2 Planet/Planetesimal Formation

One of the ultimate goals of studies for protoplanetary disks is understanding the planet/planetesimal formation. As explained above, the initial size of the dust grains is believed to be $\sim$0.1 μm. The dust grains stick to each other in protoplanetary disks to form kilometer-sized planetesimal and ultimately to form a planet, with the size of $\sim$100,000 km. In other words, the planet formation is extraordinary grain growth with the size and mass range of $\sim 10^{13}$ and $\sim 10^{40}$, respectively. A huge number of theoretical, observational studies and laboratory experiments have been conducted to clarify how such evolution can be realized. Nevertheless, we are still far from fully understanding the physics.

In this section, based on previously developed theoretical studies, we first review gas and grain motions in subsection 2.2.1 and proposed pathways of grain growth in subsection 2.2.2. Then, we introduce barriers, which limit the grain growth in subsection 2.2.3. Finally, we introduce possible solutions to avoid the barriers in subsection 2.2.4.

1.2.1 The Motions of Gas and Dust Grains

To investigate the grain growth processes, it is essential to know the gas and grain motions in protoplanetary disks. To first order, dust grains in protoplanetary disks rotate with the Keplerian velocity v_K, which is determined by the balance between stellar gravity and centrifugal force.

The gas motion, on the other hand, is not identical to that of the dust grains. One difference is that gas feels pressure gradient, resulting in deviations from the Keplerian motion. Assuming the stationary axisymmetric flow, the radial component of the momentum equation is given by

$$\frac{v_{\phi,\mathrm{gas}}^2}{r} = \frac{GM_*}{r^2} + \frac{1}{\rho}\frac{dP}{dr}, \tag{1.15}$$

where $v_{\phi,\mathrm{gas}}^2$ denotes the orbital velocity, P denotes the pressure. Because the pressure near the disk mid-plane decreases with the distance, the second term on the right side is negative and the orbital velocity is slightly reduced from the Keplerian velocity. To derive the orbital velocity, radial variations of pressure is assumed to be power-law near some fiducial radius r_0 as given by

$$P = P_0\left(\frac{r}{r_0}\right)^{-n}, \tag{1.16}$$

where P_0 is the pressure at r_0 given by $P_0 = \rho_0 c_s^2$. By substituting Equation 1.16 to 1.15, the orbital velocity is derived as

$$v_{\phi,\mathrm{gas}} = v_K\left(1 - n\frac{c_s^2}{v_K^2}\right)^{1/2}. \tag{1.17}$$

Due to the velocity difference, the dust grains feel the headwind from the gas. The gas headwind induces the aerodynamic force acting on the dust grains. In calculating the force, there are two physical regimes to consider, which are dependent on the relationship between the grain size a and mean free path of the gas λ.

Epstein drag:
One is Epstein drag regime that is applicable when $a \lesssim \lambda$. In this regime, the net aerodynamic force is determined by the frequency of collisions between the grains and gas molecules. The frequency equals to the product of the collisional cross section, relative velocity, and number density of gas molecules. The gas molecules move with the thermal velocity, which is given by

$$v_{\rm th} = \sqrt{\frac{8k_BT}{\pi\mu m_p}}. \tag{1.18}$$

We consider the aerodynamic force acting on a dust grain moving with velocity v. The gas relative velocity seen from the particles are given by $v_{\rm th} + v$ and $v_{\rm th} - v$ for the front and rear side of the particles, respectively. Thus, the grain collide with the molecules with the frequency of

$$f_+ \simeq \pi a^2 (v_{\rm th} + v)\frac{\rho}{\mu m_p} \tag{1.19}$$

for the front side of the grains, and

$$f_- \simeq \pi a^2 (v_{\rm th} - v)\frac{\rho}{\mu m_p} \tag{1.20}$$

for the rear side. The change of the momentum per collision is approximately given by $2\mu m_p v_{th}$, and thus the net drag force F_D scales as

$$F_D \propto -\pi a^2 \rho v_{\rm th} v \tag{1.21}$$

As is presented in Equation 1.21, the force is proportional to the surface area of the particles, relative velocity, thermal speed of molecules. Note that this formulation is appropriate when the grain velocity is subsonic ($v \lesssim v_{\rm th}$).

Stokes drag:
The law of the aerodynamic force switches to the Stokes drag regime when $a \gtrsim \lambda$. The interaction with the gas in the regime is treated in fluid terms without invoking the molecular nature of the gas, unlike the Epstein law. The drag force in the regime scales as

$$F_D \propto -\pi a^2 \rho v^2 \tag{1.22}$$

The proportional constant, which scales Equation 1.22 is dependent on the shape of the dust grains and on the fluid Reynolds number. Weidenschilling (1977a) has derived the constants for some ranges of Reynolds number.

To derive the grain motion, we need to define a parameter that denotes how well the grain motion is coupled to that of the gas. Here, we introduce a friction time $t_{\rm fric}$, in which the grain motion relative to the gas is stopped by the aerodynamic drag force. Previous observations indicate that the size of dust grains in protoplanetary disks is mostly $\sim$0.1 μm$-$1 mm, to which the Epstein drag is applicable. Thus, with Equation 1.22, we define $t_{\rm fric}$ as

$$t_{\rm fric} = \frac{mv}{F_D} = \frac{\rho_s}{\rho}\frac{a}{v_{\rm th}}. \tag{1.23}$$

The last modification in Equation 1.23, we insert $m = (4/3)\pi s^3 \rho_s$, where ρ_s denotes the material density, into Equation 1.23.

As is indicated by Equation 1.23, the friction time is proportional to the grain size and inversely proportional to gas density. When we assume Hayashi disk model, the friction time for a particle of size a = 1 μm at 1 au ($\rho = 10^{-9}$ gcm^{-3}, ρ_s = 3 gcm^{-3}, and $v_{\rm th}$ = 10^5 cms^{-1}), is derived as

$$t_{\rm fric} \simeq 3\ s, \tag{1.24}$$

indicating that the small grains tightly coupled to the gas.

For the following discussions, we introduce an additional parameter, Stokes number (St), which is a product of the friction time and Keplerian angular velocity Ω_K as

$$St = \Omega_K t_{\rm fric}. \tag{1.25}$$

This denotes the ratio of the friction timescale to the Keplerian timescale. Of course, small St (St $\ll$ 1) indicates the strong coupling with the gas, while large St (St $\gg$ 1) indicates the weak coupling with the gas. Assuming the Epstein drag, Equation 1.25 is rewritten by

$$St = \frac{\rho_s}{a}\frac{\rho}{v_{\rm th}} = \frac{\pi}{2}\frac{a\rho_s}{\Sigma_g} \tag{1.26}$$

Stokes number is also proportional to the grain radius a and inversely proportional to the gas surface density.

1.2.2 Pathways of Grain Growth

A plausible pathway of planet/planetesimal formation is collisional grain growth. Here, we assume that the collisions always lead to the sticking of the grains. To the collisions take place, the dust grains need to have nonzero relative velocity against other grains. Proposed mechanisms, which can arise the relative velocity, is Brownian motion, differential sedimentation, radial drift. Which process dominates the growth process is determined by how rapidly the grains become larger via each process. This can be described with the growth speed with $\dot{m}$, which is the time derivative of the grain mass, which is given by

$$\dot{m} = \pi a^2 \rho f \Delta v, \tag{1.27}$$

where ρ is gas mass density, f is the dust-to-gas ratio and Δv is the relative velocity between two grains. The growth timescale $t_{\rm grow}$, which denotes the required time to form grains with the mass of m is given by

$$t_{\rm grow} = \frac{m}{\dot{m}} = \frac{4}{3}\frac{\rho_s}{\rho f}\frac{a}{\Delta v}, \tag{1.28}$$

where we substitute $m = (4/3)\pi a^3 \rho_s$ to the second equation. The process with the shortest $t_{\rm grow}$ dominantly influences the growth process. If we fix the gas density ρ, grain volume density ρ_s, and dust-to-gas ratio f, the timescale is determined only by the relative velocity $v_{\rm rel}$ at a given grain radius a. In the following, we describe each process and growth timescale predicted by Equation 1.28.

Brownian motion:
In the initial stage of the grain growth processes, the tiny grains with a size of $\sim$0.1 μm are thought to be distributed in the whole disks. Under the condition, the dominant growth process is the Brownian motion, where gas with a temperature of T introduces a random velocity on the order of $(1/2)mv^2 \sim k_B T$. The collision velocity of the grains with the mass of m is given by

$$\Delta v \sim 4\sqrt{\frac{k_B T}{\pi m}}. \tag{1.29}$$

By substituting Equation 1.29 to Equation 1.28, the collision timescale in the Brownian motion regime $t_{\rm grow,\,Brownian}$ is derived as

$$t_{\rm grow,Brownian} = \frac{2\pi\rho_s^{3/2} a^{5/2}}{3\rho f\sqrt{3k_B T}}. \tag{1.30}$$

To yield the rough estimation, we consider a grain at 1 au and substitute $\rho = 10^{-10}$ gcm^{-3}, $\rho_s = 3$ gcm^{-3}, $f = 10^{-2}$, and $T = 300$ K, which are typical numerical values for conditions in the inner protoplanetary disks to Equation 1.30. The resultant timescale is

$$t_{\rm grow,Brownian} \simeq 24\left(\frac{a}{1\ \mu m}\right)^{5/2} \quad \text{year}, \tag{1.31}$$

which is a very short timescale compared to that of the disk evolution, suggesting that the Brownian motion efficiently works to lead to grain growth in the small grain size range. The timescale rapidly increases with grain size as indicated in Equation 1.30($t_{\rm grow,Brownian} \propto a^{5/2}$). For example, substituting $a \sim 1$ mm, the timescale is derived as $\sim$30 Myr, which is much longer timescale compared to that of disk evolution. In fact, Brauer, Dullemond, and Henning (2008) has conducted numerical simulations of the grain growth and revealed that the grain size reaches as small as $\sim$10 μm via Brownian motion within 1 Myr. This indicates that other mechanisms need to be invoked for further grain growth.

Differential settling:
This process is related to the grain motion in the vertical directions. As explained above, when the grain is small, where St $\ll 1$, the grains are almost completely coupled to the gas and follow the same distributions of the gas in the vertical directions. However, as the grains become larger, they become decoupled to the gas and settle toward the midplane. This introduces the settling velocity, which is determined by the balance between the stellar gravity and the pressure gradient in the vertical directions.

We consider the balance of the force acting on a small dust grain at height z. The downward force is the stellar gravity while the upward force is the aerodynamic drag as written by

$$m\Omega_K^2 z = \frac{4\pi}{3}\rho s^2 v_{\rm th} v, \tag{1.32}$$

where we assume Epstein drag 1.21 for the right side of Equation. The equation yields the terminal settling velocity $v_{\rm settle}$ of

$$v_{\rm settle} = \frac{\rho_s}{\rho}\frac{a}{v_{\rm th}}\Omega_K^2 z = z\Omega_K t_{\rm fric}, \tag{1.33}$$

where the second equation is replaced with Equation 1.23 This equation indicates that two grains with different sizes have nonzero relative velocity.

By substituting Equation 1.33 to Equation 1.27, the growth speed is derived as

$$\dot{m} = \frac{3}{4}\frac{\Omega_K^2 f}{v_{\rm th}} z m \tag{1.34}$$

and the growth timescale $t_{\rm grow,settling}$ is given by

$$t_{\rm grow,settling} = \frac{3}{4}\frac{v_{\rm th}}{z\Omega_K^2}\frac{1}{f}. \tag{1.35}$$

It is worth noting that the growth timescale for the differential settling is inversely proportional to gas-to-dust ratio, indicating that the assumption on that parameter has substantial impact on the growth process.

We derive a specific timescale by substituting the numerical values appropriate for $z = 3 \times 10^{11}$ cm at 1 au ($\rho = 6^{-10}$ gcm^{-3}, $c_s = 10^5$ cms^{-1}, $\rho_s = 3$ gcm^{-3}, $f = 10^{-2}$) to Equation 1.35. As a result, the timescale of the grain growth is derived as

$$t_{\rm grow,settling} \simeq 600 \text{ year}, \tag{1.36}$$

which is much shorter timescale compared to that of the disk evolution, indicating that the settling efficiently works for the grain growth.

The differential settling dominates the Brownian motion for the grain growth process in the larger size range. Roughly speaking, the critical radius, where the settling becomes to influence the grain growth, can be derived by comparing the relative velocity produced via each process. Equating the Brownian velocity (Equation 1.29) and the settling velocity (Equation

1.33), we find that the critical radius is given by

$$a < \left(\frac{4}{\pi^{3/2}}\frac{6}{\mu m_H}\frac{\rho}{\rho_s^{3/2}}\frac{kT}{\Omega_K^2 z}\right)^{2/5}. \tag{1.37}$$

Substituting the same parameters above ($\rho = 10^{-10}$ gcm^{-3}, $c_s = 10^5$ cms^{-1}, $\rho_s = 3$ gcm^{-3}, $f = 10^{-2}$, T = 300 K), the specific value is derived as

$$a < 1\mu m. \tag{1.38}$$

Above this size range, the differential settling (or radial drift explained below) is dominant process for the grain growth.

As indicated in the short timescale in the two processes, the grain growth rapidly takes place as long as the fragmentation is neglected. Brauer, Dullemond, and Henning (2008) has revealed that the combination of the two processes promote rapid grain growth as large as a $\sim 10^4$ cm at $\sim$1 au and submicron-sized particles are mostly cleared due to the growth. It is not consistent with the fact that the scattered light from the submicron-sized particles is ubiquitously observed, suggesting that long-lived small grains remain in protoplanetary disks.

Radial drift:
As well as the vertical directions, dust grains can also radially drift due to the aerodynamic force from gas. Although we explained that the angular velocity of the grains approximately equal to the Keplerian velocity, we here need to include the effect of the gas drag acting on the grains for the momentum equations as follows.

$$\frac{dv_{\rm r}}{dt} = \frac{v_\phi^2}{r} - \Omega_K^2 r - \frac{1}{t_{\rm fric}}(v_r - v_{\rm r,\,gas}), \tag{1.39}$$

where v_r and $v_{r,\,gas}$ is the radial component of the velocity for the grains and gas, respectively. The effect of drag force is included in the third term of the right-hand side. The azimuthal component v_ϕ of the grain velocity is derived by considering the torque induced by the gas drag as given by

$$\frac{d}{dt}(rv_\phi) = -\frac{r}{t_{\rm fric}}(v_\phi - v_{\phi,\rm gas}) \tag{1.40}$$

where v_ϕ and $v_{\phi,\,\rm gas}$ are the azimuthal component of the velocity for the grains and gas, respectively. Equation 1.40 can be simplified by assuming that grain angular velocity v_ϕ is nearly the Keplerian velocity and time-independent.

$$\frac{d}{dt} \approx v_r \frac{d}{dr}(rv_K) = \frac{1}{2}v_r v_K. \tag{1.41}$$

By substituting Equation 1.41 to Equation 1.40, we obtain

$$v_\phi - v_{\phi,\,\mathrm{gas}} \approx -\frac{1}{2}\frac{t_{\mathrm{fric}} v_r v_K}{r}. \tag{1.42}$$

For the radial component of the momentum equation, we substitute for Ω_K by Equation 1.17 and retain only the first order terms.

$$\frac{dv_r}{dt} = -\eta\frac{v_K^2}{r} - \frac{2v_K}{r}(v_\phi - v_{\phi,gas}) - \frac{1}{t_{\mathrm{fric}}}(v_r - v_{\mathrm{r,gas}}). \tag{1.43}$$

Assuming the steady state, the term dv_r/dt is negligible. By substituting Equation 1.42 for (v_ϕ - $v_{\phi,gas}$) in Equation 1.43, we obtain

$$v_r = \frac{(r/v_K)t_{\mathrm{fric}}^{-1} v_{\mathrm{r,\,gas}} - \eta v_K}{(v_K/r)t_{\mathrm{fric}} + (r/v_K)t_{\mathrm{fric}}^{-1}}. \tag{1.44}$$

Substituting Equation 1.25 to Equation 1.44, the drifting velocity is simplified as

$$v_{\mathrm{r}} = \frac{St^{-1} v_{\mathrm{r,gas}} - \eta v_K}{\mathrm{St} + \mathrm{St}^{-1}}. \tag{1.45}$$

v_ϕ is also derived by substituting Equation 1.45 to 1.42 as follows

$$v_\phi = \frac{v_{\mathrm{r,gas}} - \eta \mathrm{St} v_K}{\mathrm{St} + \mathrm{St}^{-1}}. \tag{1.46}$$

When we assume the grains with $\mathrm{St} \ll 1$, where the grains are small and strongly coupled to the gas, Equation 1.45 is rewritten by

$$v_{\mathrm{r}} \approx v_{\mathrm{r,gas}} - \eta \mathrm{St} v_K. \tag{1.47}$$

The equation indicates the dust grains can have drifting velocity relative to the gas, which is proportional to the Stokes number.

The drifting velocity peaks at St = 1, where the grains are intermediately coupled to the gas. The peak drifting velocity is derived as

$$v_{\mathrm{r,\,peak}} = \frac{1}{2}\eta v_K = \frac{1}{2}\frac{n c_s^2}{v_K} \tag{1.48}$$

Substituting the same values above (c_s = 10^5 cms^{-1}), the peak velocity is as large as $\sim$50 cms^{-1}, which is much faster than that of gas drifting velocity due to the viscosity. On the other hand, when $\mathrm{St} \gg 1$, since the dust grains are tightly coupled to the gas, the dust grains do not feel the gas drag, resulting in small drifting velocity. When $\mathrm{St} \ll 1$, since dust grains tightly coupled to gas, the motion of grains are almost identical to that of gas, also resulting in the small drifting velocity. Therefore, the dust grains with $\mathrm{St} \sim 1$ have fast drifting velocity, which induces the grain collisions and growth. However, the process can also prevent the growth by rapidly removing the grains in protoplanetary disks as we will show in the next subsection.

1.2.3 Barriers Against Planetesimal Formation

We have explained that if the collisions always lead to grain growth, the grain size easily reaches as large as kilometer-sized bodies. However, there are barriers, which make it difficult to realize the coagulation.

Charge barrier:
Dust grains can acquire nonzero charges because protoplanetary disks are weakly ionized by cosmic rays and X-rays from central stars. Such ionized particles can have a repulsive force acting on colliding counterparts. This can disturb the grain growth (Okuzumi, 2009; Okuzumi et al., 2011a; Okuzumi et al., 2011b).

Bouncing barrier:
The outcome of grain collisions is not only sticking. Colliding particles can bounce each other rather than stick together at moderate collision velocity (e.g. Güttler et al., 2010). It is due to the reason that the impact energy of colliding grains can exceed the attractive surface force of the grains. Laboratory experiments actually showed bouncing of grains made of silica or water ice (e.g. Güttler et al., 2010; Wada et al., 2011). If this is the case in disks, it could limit the grain growth (Zsom et al., 2010; Zsom et al., 2011).

Fragmentation barrier:
High-speed grain collisions even lead to grain fragmentation. The fragmentation velocity, beyond which the collisions induce the grain fragmentation, is dependent on the grain properties. It is problematic in the growth process because the dust grains are thought to primarily composed of silicate whose fragmentation velocity is as low as few ms^{-1} (Blum and Wurm, 2008; Wada et al., 2009; Güttler et al., 2010). Because the relative velocity of grains can easily reach as high as a few tens of ms^{-1} by the differential settling or radial drift, the fragmentation at high-speed collisions limits the growth.

Through N-body collision experiments, Wada et al. (2009) has revealed that aggregates made of 0.1 μm sized icy grains can avoid the barrier because their fragmentation velocity can be up to $35-70$ ms^{-1}. This provides one solution for the fragmentation barrier outside the snowline in protoplanetary disks.

Radial drift barrier:
The inward drifting of the dust grains can lead to collisional grain growth. However, the drifting motion can also remove the dust grains from the disks by dropping them onto the stars and limit the grain growth at a certain size. The drifting timescale in which the grain fall on to the stars are given by

$$t_{\mathrm{drift}} = \frac{r}{|v_r|} \tag{1.49}$$

With Equations 1.49 and 1.44, we plot the drifting timescale at 1 au as a function of St. As shown in the Figure, the dust grains with the order of $\mathrm{St} \sim 1$

rapidly fall onto stars.

On the other hand, the growth rate and timescale of a dust grain of a radius a that collides primarily with smaller grains are derived by inserting the drifting speed (Equation 1.44) into Equations 1.27 and 1.28, respectively. How large the dust grain can grow within the drifting timescale can investigated by comparing the drifting timescale to the growth timescale. The condition of $t_{\rm grow,drifting} < t_{\rm drift}$ is satisfied if grain size is

$$a \lesssim \frac{3f}{4\sqrt{2\pi}} \left(\frac{h}{r}\right)^{-1} \frac{\Sigma}{\rho_s} \tag{1.50}$$

As done in the subsection 1.2.3, we substitute the numerical values appropriate at 1 au (f = 0.01, $\Sigma = 1.7 \times 10^3$ gcm^{-2}, ρ_s = 3 gcm^{-3}, and h/r = 0.05) and find that the grain size is limited at $a \sim 1$ m. This implies that the dust grains initially can coagulate to form larger aggregates via collisions; however, as they become larger and decoupled to gas, they start to rapidly fall to stars. One possible solution to tackle the barrier is grain trapping as we will explain in the next subsection.

1.2.4 Possible Solutions to Overcome the Barriers

A number of theoretical studies to overcome the barriers have been conducted. The fragmentation barrier is problematic when dust grains mainly composed of silicate particles whose fragmentation velocity is as low as a few m s^{-1} (Blum and Wurm, 2008; Wada et al., 2009; Güttler et al., 2010). In contrast, the dust grains composed of water ice particles can avoid the fragmentation unless the collisional speed is so high. It is because their fragmentation velocity is as high as 35−70 m s^{-1}, making the collisional growth easier. The bouncing barrier is also less problematic when the dust aggregates with high porosity are assumed (Wada et al., 2011).

The radial drift barrier is problematic when the gas pressure decreases with radii to make the gas rotate with the sub-Keplerian. Naively thinking, creating a positive pressure gradient can be a solution to avoid the barrier. One promising scenario is stopping the dust drift at local pressure maxima, concentrating the dust grains to a narrow extent. This scenario is indicated by the substructure of dust disks, which are, for example, multi-ringed structure, crescent-like structure, spiral-like structure, as we will explain in Section 1.3. Multiple theories to drive the gas pressure enhancements are proposed, which are for example, vortex instabilities (e.g. Barge and Sommeria, 1995; Klahr and Henning, 1997), perturbing planet-like companions (e.g. Whipple, 1972; Pinilla, Benisty, and Birnstiel, 2012) and some MHD effects (Johansen, Youdin, and Klahr, 2009; Bai and Stone, 2014; Simon and Armitage, 2014) and vortices.

We here explain the trapping scenario assuming the radial pressure bump. At the outside of the gaps, radial profiles of pressure are considered to have bump structures. Outside the pressure maxima, the gas rotates with the sub-Keplerian due to the negative pressure gradient and forces the grain to fall

to the maxima. Inside the maxima, on the other hand, the positive pressure gradient makes the gas rotate with super-Keplerian. The grains gain the angular momentum from the gas and outwardly drift. As a result, the grains drift to the pressure maxima, leading to form concentric rings made of dust grains.

Not only does the process halt the drifting grains, but it can also concentrate the dust grains in the narrow range, leading to form a dust clump. Such localized dust concentrations can increase the dust-to-gas ratios, approaching unity, which can induce the streaming instability (Youdin and Goodman, 2005; Johansen et al., 2007), which accelerates to form the clump structures. This can eventually lead to gravitational collapse and form planetesimals and planet (Goldreich and Ward, 1973; Youdin and Shu, 2002).

1.3 Observations for Class II Disks

Theoretically, the coagulation process through the collisions is far from fully understanding. Thus, observational constraints on the geometrical structure and grain properties in protoplanetary disks are essential to Here, we primarily review the previous observations for class II disks. For two decades, high-resolution observations from near-infrared to millimeter wavelengths have revealed that disks in the phase have various geometrical structures, such as a cavity, ring, gap, and lopsided. Such geometrical structures possibly reflect the environment of early planet formation. Because of this possible connection, a number of observations aiming to constrain the geometrical structures have been intensively conducted.

Transition disks have been first identified as objects with dips in the infrared spectra, which is a lack of near-infrared excess with remaining strong excess at longer wavelength (Strom et al., 1989; Wolk and Walter, 1996). The lack of near-infrared excess implies the presence of the cavity extending a few to tens of au, where the dust grains are cleared by some mechanisms. Based on the diagnostic with the infrared spectra, such types of disks have supposed to comprise a small fraction of the disk population in nearby star-forming regions (Cieza et al., 2007; Muzerolle et al., 2010). If all protoplanetary disks were to experience such clearing, the small fraction indicates that the timescale of the inner disk depletion is rapid compared to the lifetime of protoplanetary disks. Photoevaporative wind and interaction with planet-mass companions are proposed to explain such rapid evolution.

The recent enhancements of the observational quality in the spatial resolution and sensitivity enable us to directly resolve and characterize the cavity structures, which have been indirectly probed by the spectra. The resolved studies revealed that such morphological features are more common than expected from the spectra (Andrews et al., 2011). The result is also supported by re-analysis for the infrared spectra. Through detailed modeling for the infrared spectra Espaillat et al. (2007b), Espaillat et al. (2007a), Espaillat et al. (2008), and Espaillat et al. (2010) revealed the presence of small infrared excess and silicate feature. This indicates that the cavity is not empty; rather, gapped structures, where the small amount of dust grains remains in

the innermost region. Even the low mass of dust grains can emit strongly in the infrared so that the dip signatures are erased, resulting in the small fraction of transitional disks in the previous studies (Isella, Carpenter, and Sargent, 2010; Isella et al., 2010; Andrews et al., 2011). These observational features and population of transitional disks imply that the dynamical interactions with low-mass companions are preferred rather than the photoevaporative wind that is predicted to drive inside-out clearing.

One of the most prominent topics in recent observational studies on class II disks is characterizing geometrical substructures. Recent resolved studies have revealed the presence of various substructures in both of the azimuthal and radial directions. Lopsided structures, where the dust grains concentrate to a certain extent in the azimuthal directions, are one example identified by ALMA (Casassus et al., 2013; Fukagawa et al., 2013; van der Marel et al., 2013; Rosenfeld et al., 2013b; Pérez et al., 2014). The preferential theory to produce such structures is the concentration of dust grains in azimuthal gas pressure maxima, which is planet-induced vortex instabilities (Barge and Sommeria, 1995; Klahr and Henning, 1997; Wolf and Klahr, 2002; Regály et al., 2012; Lyra and Lin, 2013; Zhu et al., 2014; Zhu and Stone, 2014). As other explanations, global gravitational modes (Mittal and Chiang, 2015), unresolved spiral structures (e.g., Pérez et al. (2014)) are proposed mechanisms to produce the lopsided structures.

Spiral structures have also been observed in many disks primarily with the scattered light in the infrared (Clampin et al., 2003; Fukagawa et al., 2004; Fukagawa et al., 2006; Muto et al., 2012; Canovas et al., 2013; Garufi et al., 2013; Grady et al., 2013; Avenhaus et al., 2014). The spatial extents of the structures are typically from the inner working angle ($\sim$10 au) to outer $\sim$100 au. The observations probe the geometrical structure in the upper layer of the disks and imply the driving physics, which shapes at the surface. As well as in the surface layers, such spiral structures were also detected in the midplane of the protoplanetary disks by the millimeter continuum emission (Pérez et al., 2016; Boehler et al., 2018; Dong, Najita, and Brittain, 2018; Huang et al., 2018b). The driving physics to produce the structures is yet unclear and being debated. As is the case for the lopsided structures, the perturbation from unseen planet-mass companion possibly drives in such disks (Muto et al., 2012; Dipierro et al., 2015).

Ringed or gapped structures are another representative substructures ubiquitously observed on class II disks. The first resolved observation of a multi-ringed structure was obtained on the HL Tau disk (ALMA Partnership et al., 2015), which displays multiple and concentric ringed structures. Subsequently, a number of such multi-ringed disks have been observed (Andrews et al., 2016; Isella et al., 2016; Tsukagoshi et al., 2016; Cieza et al., 2017; Fedele et al., 2017; Fedele et al., 2018; Clarke et al., 2018; Dipierro et al., 2018; Long et al., 2018; van Terwisga et al., 2018; Guzmán et al., 2018). The preferential scenario to produce such ringed structures are grain trapping at gas pressure maxima as is the case for the other substructures. Proposed scenarios to make the gas pressure maxima are, for example, rotating planet (Kanagawa et al., 2015; Kanagawa et al., 2016; Bae, Zhu, and Hartmann, 2017;

Dong et al., 2017; Huang et al., 2018b; Fedele et al., 2018), some MHD effects (Johansen, Youdin, and Klahr, 2009; Bai and Stone, 2014; Simon and Armitage, 2014) and secular gravitational instability (Takahashi and Inutsuka, 2014; Tominaga, Inutsuka, and Takahashi, 2018).

As explained above, the multiband and high spatial resolution observations have revealed that the various spatial structures are prevalent, and these are possibly connected with the early stage of the planet or planetesimal formation. At the same time, however, there are a number of physical processes involved in producing such various morphology and which mechanism dominates the evolution is still highly unclear. To disentangle the driving physics, it is essential to put constraints on the grain properties including size, shape and so on. It is because that all proposed mechanisms are directly linked to the interactions between gas and dust grains, where the grain property is crucial parameters. In this study, we employ a distinct observational way, continuum polarization observation in millimeter-wave to further constrain the grain properties and disk environment.

1.4 Millimeter-wave Polarization

The high spatial resolution observations explained above have revealed that the substructure is common and various in the protoplanetary disks. The substructures reflect the underlying physical processes, which are possibly connected to planet/planetesimal formation. A number of complex physical processes are probably involved in producing such various substructures. To address the physics driving in disks, the observations relying only on the high spatial resolution is not sufficient. Thus, other observational tracers are necessary. In this paper, we employ a new observational tool, dust polarization at millimeter wavelengths. As we will discuss below, millimeter-wave polarization observations can provide us special opportunities to constrain the grain properties.

The presence of dust polarization has been indicated by polarized emission of starlight through the interstellar medium at optical wavelengths (Hiltner, 1949). Subsequent studies also detected the polarized emission at longer wavelengths from infrared to millimeter wavelengths (e.g. Cudlip et al., 1982) The origin of the polarization is elongated grains aligned by magnetic fields (Davis and Greenstein, 1951; Cho and Lazarian, 2007). At optical wavelengths, the absorption and scattering by the aligned grains make the emission partially polarized. At longer wavelengths, on the other hand, the thermal emission of the aligned grains are also polarized. This picture is supported by the fact that polarization orientations nearly orthogonal to each other between optical and longer wavelengths (Cudlip et al., 1982). Owing to such property of the dust grains, the polarization especially at millimeter wavelengths, where we suffer less from the dust extinction, have provided us the strong tool to constrain the directions or strength of the magnetic field in interstellar medium (ISM) and star-forming clouds (e.g. Planck Collaboration et al., 2015; Planck Collaboration et al., 2016; Pattle et al., 2017; Coudé et al., 2019).

The presence of dust polarization of protoplanetary disks at submillimeter/millimeter wavelengths have been indicated for several protostars and T Tauri stars with the James Clerk Maxwell Telescope (JCMT) single-channel polarimeter (Akeson and Carlstrom, 1997; Tamura, Hough, and Hayashi, 1995; Tamura et al., 1999). However, for two decades, spatially resolved polarization has not been obtained due to the lack of the sensitivity and spatial resolutions of the instruments (Hughes et al., 2009; Hughes et al., 2013) until the first millimeter polarization detection for the HL Tau disk by (Stephens et al., 2014). Nowadays, ALMA dust polarization observations have enabled us to obtain the polarization for various class II protoplanetary disks, showing the various polarization morphology and polarization fraction (Bacciotti et al., 2018; Cox et al., 2018; Girart et al., 2018; Harris et al., 2018; Hull et al., 2018; Lee et al., 2018; Ohashi et al., 2018; Sadavoy et al., 2018a; Sadavoy et al., 2018b; Harrison et al., 2019). In the next subsection, we review the millimeter-wave polarization with the theoretical and observational points of view.

1.4.1 Origins of Millimeter-wave Polarization of Protoplanetary Disks

Here, we introduce the proposed theories that can produce polarized emission at millimeter wavelengths from protoplanetary disks. The mechanisms producing millimeter-wave polarization in disks are grain alignment and scattering as we discuss below.

Grain alignment:
Here, we assume dust grains with elongated along a direction, which looks like a needle. The proposed alignment mechanism can be divided into two cases: alignment with spinning and without spinning. We first explain the alignment processes with spinning. The grain alignment starts with the spinning of the elongated grains induced by external torque from the flow of gas or photons. The spinning leads to the precession motion of a grain, where the angular momentum vectors become to be aligned with a precession axis. In protoplanetary disks, possible precession axes are magnetic fields, gas flow or radiative gradient. The dust grains become aligned with the axes with the shortest precession timescale. If the Lamor precession is the shortest, dust grains become aligned with the magnetic fields, otherwise they become aligned with the gas flow or radiative gradient. Inversely, the grain spinning can be randomized by, for example, gaseous damping. If the damping timescale is the shortest compared to all the precession timescales, the grains quit precession, resulting in the random orientations of dust grains.

Subsequently, the spinning becomes stabilized with their shortest axes parallel to the precession axes, where the rotational kinetic energy of spinning grains is the lowest. The kinetic energy is partially converted into heat by internal energy dissipation. There are multiple dissipation process proposed thus far: Barnett relaxation (Purcell, 1979), nuclear relaxation (Lazarian and Draine, 1999), superparamagnetic Barnett relaxation (Lazarian and

Draine, 1999; Hoang and Lazarian, 2008), and inelastic relaxation (Purcell, 1979; Lazarian and Efroimsky, 1999).

The emitter of the polarization is the dust grains aligned by some external force explained above. Since the short axes of the aligned grains are parallel to the force, the polarization orientations are predicted to be perpendicular to the force.

Next, we explain another case, alignment without the spinning of dust grains. The dust grains can also be aligned with their long axes parallel to an external force without the spinning. The possible force, in this case, is gas flow acting on the dust grains (Gold, 1952). Unlike the helicity-induced alignment, the resultant polarization vectors are predicted to be parallel to the alignment axes if the model is effective. In general, the process is supposed to be negligible in disks because it arises when the velocity of the gas flow on grains is supersonic while that in disks is subsonic (Gold, 1952).

For the following explanation, we introduce two types of shapes for the elongated grains, oblate and prolate grains. The shape of the prolate grains is infinitely thin and elongated (or "needle"-like), while that of the oblate grains is ellipsoid (or "dorayaki"-like). One important note is that helical prolate grains that spin about the alignment axis are regarded as "effectively" oblate grains. Thus, in the Gold alignment model, the prolate grains are aligned by the gas-flow with their long axes parallel to the flow. On the other hand, in the helicity-induced alignment models, oblate or prolate grains with a certain helicity are aligned by photon- or gas-flow with their long axes perpendicular to the flow. Figure 1.4 visualizes the explanations for the three cases. In the following, we refer to the assumed grains in the Gold alignment as prolate grains and in the helicity-induced alignment models as the oblate grains.

Self-scattering:
Recent studies have revealed that scattering-induced polarization also plays a crucial role in the polarized emission. The dust grains scatter and polarize the incoming emission when the following two conditions are satisfied. One of the conditions is related to the grain size. As predicted in the Rayleigh scattering regime, where the dust grains are smaller than the observation wavelength, the scattering opacity is low compared to the absorption opacity but polarization fraction is high. On the other hand, if dust grains are larger than the observation wavelength, the scattering opacity dominates over the absorption opacity while the polarization fraction is low. Considering the dependence on grain size, one can predict that the polarized emission is expected to be important when the grain size is comparable to the observation wavelength. Precisely speaking, dust grains with a size of $a \sim \lambda/2\pi$ is expected to preferentially polarize the incoming emission.

The other condition is related to the flux distribution around scattering grains. In the self-scattering model, the incoming emission to be scattered is the thermal emission of grains surrounding the scatterers. If the incoming flux is entirely isotropic, the intensity of polarized scattered light in one direction is as same as that in the direction different by 90°. This cancels cancel

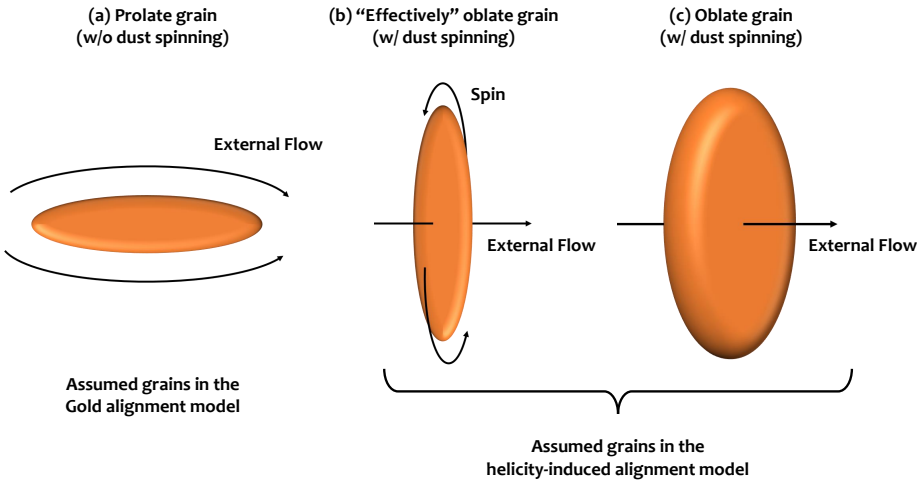

FIGURE 1.4: Schematic views of the assumed grain models. (a) The prolate grains without helicity and aligned by the gas flow with their long axes parallel to the flow. This grain model is assumed in the Gold alignment model. (b) The prolate grains with a certain helicity and are aligned by the flow with their long axes perpendicular to the flow. This is regarded as an "effectively" oblate grain. (c) The oblate grains aligned by the flow. We regard the (b) and (c) models as the oblate grain model, which is assumed in the helicity-induced alignment model.

each other out and results in no polarized emission in total. If the flux distributions are anisotropic, on the other hand, the polarized emission in the two directions is not perfectly canceled out. As a result, the partially polarized emission is predicted to be observed as a residual.

Summarising the explained theory, the dust grains whose size is comparable to the observation wavelengths efficiently scatter and polarize the incoming flux. Theoretically, Kataoka et al. (2015) predicted that the polarization fraction reaches as high as 2%−3% when the grain population has a single power-law with the maximum grain size of $a_{max} \sim \lambda/2\pi$. In other words, we can use the polarization observations as another prove to measure the grain size.

1.4.2 Expected Polarization Pattern in the Alignment and Self-scattering Model

The grain alignment and self-scattering models predict the intrinsic polarization pattern. Thus, the polarization pattern is one of the probes to distinguish the polarization origins. First, we explain the expected pattern in the grain alignment model for face-on disks. Although the pattern is predicted to be modified in inclined disks, we will explain the pattern in the distinctive sections, where the specific objects (AS 209 and HL Tau) are discussed. Then, we explain the polarization pattern predicted in the self-scattering model. The

pattern is predicted to be highly sensitive to the disk inclination and thus we also explain the pattern in the inclined and edge-on disks.

Grain alignment:

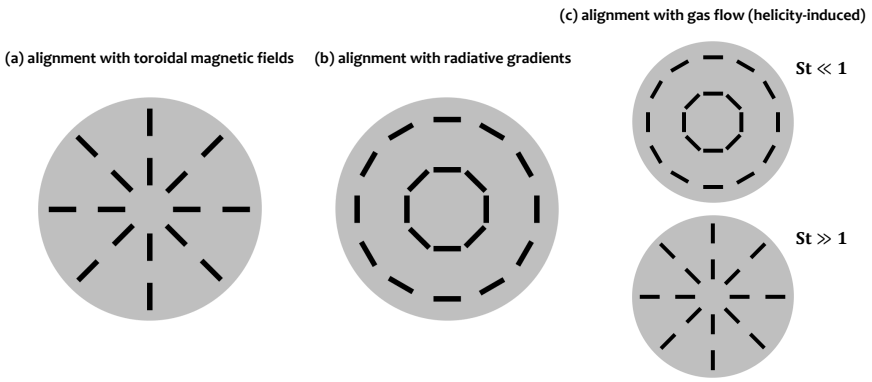

FIGURE 1.5: Schematic views of polarization vectors predicted by the grain alignment models for face-on disks. Note that the intensity profile of the disks is assumed to be smooth and axisymmetric.

We briefly discuss the expected pattern in the alignment model with the help of the illustration as shown in Figure 1.5. As explained above, the helical grains tend to be aligned with some external force, which is magnetic fields, radiative gradient or gas flow on the grains. The magnetic fields in disks are predicted to be toroidal due amplification via magnetorotational instability (Brandenburg et al., 1995; Fromang and Nelson, 2006; Bai and Stone, 2013; Suzuki and Inutsuka, 2014). Thus, if the magnetic fields efficiently align the grains, the resultant polarization pattern would show a radial pattern. On the other hand, the radiation gradient points in the radial and thus the pattern would be an azimuthal (circular). In the case of gas-flow alignment, the expected pattern would not be unique because the directions of gas flow on grains are sensitive to the gas-grain interactions, which is dependent on the grain size and gas density (i.e. Stokes number). The case is the same in the Gold alignment model. Therefore, we will discuss the expected pattern in the gas-flow and Gold alignment models in Section 2.4 and 3.1.

Self-scattering:
We discuss the expected pattern in the self-scattering model for face-on, inclined and edge-on disks as shown in Figure 1.6. The polarization orientations in the self-scattering model are in directions where the difference of incoming flux between one direction and the direction different by 90° becomes maximum. In the face-on disks, where the intensity profile is assumed to be smooth and axisymmetric, the polarization vectors are in the azimuthal directions. It is because that the radiation gradients are in the radial directions. In contrast, the polarization vectors orients in the minor axes of the disks because the flux coming from the directions are much stronger than other directions. In the inclined disks, the polarization pattern would be a

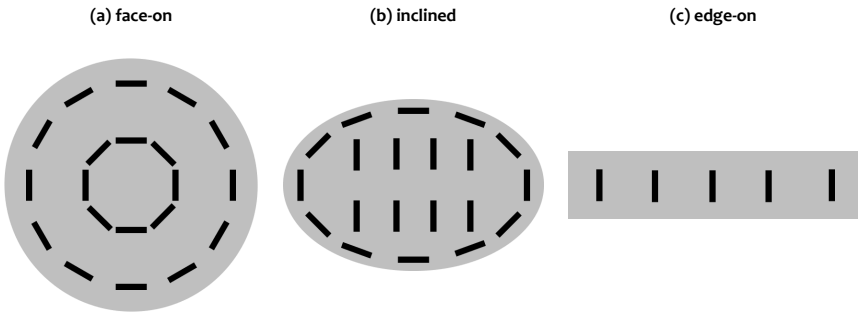

FIGURE 1.6: Schematic views of polarization vectors predicted by the self-scattering model for face-on, inclined, and edge-on disks. The assumed intensity profile is smooth and axisymmetric as in Figure 1.5.

combination of patterns in the face-on and edge-on disks: the polarization vectors orient in the minor axes in the central region, while they are in the azimuthal directions in the outer regions.

1.4.3 Summary of Previous Polarization Observations

The detection of millimeter-wave polarization of protoplanetary disks was achieved for several protostars and T Tauri stars with the James Clerk Maxwell Telescope (JCMT) single-channel polarimeter (Akeson and Carlstrom, 1997; Tamura, Hough, and Hayashi, 1995; Tamura et al., 1999). Tamura et al. (1999) significantly obtained $\sim 3\%$ polarization toward the disks around GM Aur and DG Tau, which was interpreted to come from magnetically aligned dust grains as this is the case in ISM or star-forming clouds. Spatially resolved millimeter-wave polarization observations, in contrast to the above observations, have been difficult to obtain for a long time due to the lack of sensitivity.

The spatial distribution of the polarization fraction and vectors first obtained on the HL Tau disk with Combined Array for Millimeter-wave Astronomy (CARMA) (Stephens et al., 2014). Subsequently, in the ALMA era, the number of the resolved polarization observations have been dramatically increasing owing to its unprecedented sensitivity and angular resolution (Bacciotti et al., 2018; Cox et al., 2018; Girart et al., 2018; Harris et al., 2018; Hull et al., 2018; Lee et al., 2018; Ohashi et al., 2018; Sadavoy et al., 2018a; Sadavoy et al., 2018b; Harrison et al., 2019). As was interpreted in Tamura, Hough, and Hayashi (1995) and Tamura et al. (1999), the polarized emission was considered to originate from the magnetically aligned grains in disks. However, various observations have revealed that the picture is not necessarily correct and showed that the scattering-induced polarization frequently appears especially in the inclined disks (Bacciotti et al., 2018; Cox et al., 2018; Girart et al., 2018; Harris et al., 2018; Hull et al., 2018; Lee et al., 2018; Ohashi et al., 2018; Sadavoy et al., 2018a; Sadavoy et al., 2018b; Dent et al., 2019; Harrison et al., 2019; Ohashi and Kataoka, 2019). Even in the nearly face-on disk,

Kataoka et al. (2016b) and Ohashi et al. (2018) found the self-scattering feature in the north region of the HD 142527 disk. These results indicate the presence of the order of $\sim$100 micron-sized grains in the many transitional disks.

Those observational works indicate that the scattering emission plays a major role in polarized emission from disks. However, in several points, we are still far from a fully understanding of the origins of the polarization. One difficulty is that several disks show features that are incompatible with the self-scattering model (Kataoka et al., 2017; Stephens et al., 2017; Yang et al., 2019). Some grain alignment models may be involved in the polarization; however, it is unclear which alignment mechanism dominantly contribute to the polarization. For example, the HL Tau disk in Band 3 shows the azimuthal polarization pattern. The possible origin of the polarization is radiative alignment or gas-flow alignment, which is yet uncertain. More complexity is that several disks show features to which multiple polarization origins possibly contribute (Kataoka et al., 2015; Stephens et al., 2017; Bacciotti et al., 2018). In Band 6, the HL Tau disk shows a feature that possibly originates from the combination of the scattering and aligned grains whose relative importance was not yet analyzed in detail (Stephens et al., 2017).

As we described in subsection 1.4.1, which alignment model works is intimately connected with grain properties such as size, shape, composition, and the interactions between solids and some external force induced by the photons, gas flow, or magnetic fields. Thus, it is important to exactly address the relative importance of the scattering/alignment models and the dominant alignment models.

To tackle the tasks, we need to investigate the distributions of the polarization angles and polarization fraction, which have been insufficiently conducted despite the importance. In this study, we conduct detailed analysis toward individual objects, AS 209 and HL Tau, both of which are known to have concentric ringed and gaped structures.

1.5 This Thesis

We summarize the described introduction thus far and motivations for this study. In protoplanetary disks, submicron-sized dust grains coagulate to form larger aggregates, and eventually to form planets. However, there are several long-standing questions, which make it difficult to realize the coagulation. Recent high resolution observations have revealed the presence of various disk substructures, which possibly captures the crucial step of planet/planetesimal formation processes. To understand the formation mechanism of substructures, the grain properties (size, shape, and composition) and interaction between the grains and external force are invaluable information. Millimeter-wave polarization can provide a new method to obtain such information. However, the origins of millimeter-wave polarization are still being debated. Keeping in mind such backgrounds, this study aims to investigate the following questions.

1. Where does the polarization originate from?

2. The observed polarization can be explained by just one theory or multiple theories?

3. How the grain properties and disk environment can be linked to the polarization origins?

4. Do the questions above provide indications for the formation theories of substructures and planetesimal?

The rest of this paper is organized as follows.

Chapter 2:
We present 870 μm ALMA polarization observation toward the Class II protoplanetary disk around AS 209, which has concentric, multiple gaps and rings. We successfully detect the polarized emission and find that the polarization orientations and fractions have distinct characteristics between the inner and outer regions. This indicates the spatial segregation of the origin of polarized emission. We conduct a detailed analysis of the polarization pattern to address the origin by investigating the polarization angle distribution.

Chapter 3:
In Chapter 3, we conduct detailed modeling for a 3 mm polarization observation observed on the HL Tau disk. The observational results have been already published by Kataoka et al. (2017) and Stephens et al. (2017). However, a recent study pointed out that current theories including alignment and scattering models cannot reproduce the observed features for the HL Tau disk (Yang et al., 2019). To solve the difficulty, we investigate a possibility that combined models of the alignment and scattering can reproduce the HL Tau polarization. First, we re-construct semi-analytical models of the grain alignment and self-scattering, which were previously developed (Yang et al., 2016; Yang et al., 2019). We combine the two models and examine if the model can produce the observed feature. Subsequently, we construct radiative transfer models of the grain alignment, self-scattering, and their combination. The further analysis enables us to confirm the results of the semi-analytical model and constrain the grain size, shape and alignment efficiency.

Chapter 4:
Based on the obtained results through the two studies, we summarize the insights regarding the grain properties, dynamics, and grain alignment process. We emphasize that this study contributes to better understandings of the polarized emission of disks. The implications for the planetesimal formation and promising future works are also discussed.

Chapter 2

Semi-analytical and radiative transfer modeling for polarized emission on the HL Tau disk

2.1 Introduction

2.1.1 Previous Observations for the HL Tau Disk

HL Tau is a protostar in the Taurus star-forming complex 140 pc away from the solar system (Rebull, Wolff, and Strom, 2004). The SED of the object shows a Class I/II feature, indicating that the surrounding envelope is not entirely cleared yet (Robitaille et al., 2007). Although the central protostar is obscured by surrounding molecular ridge and is invisible at the optical wavelengths (Welch et al., 2000; Anglada et al., 2007), active star formation in the region is indicated by jets and outflows (Lumbreras and Zapata, 2014). Due to the large visual extinction of the object, determinations of stellar properties above have substantial uncertainties. Based on high dispersion spectroscopy, the spectral type of the object is classified as K5 $\pm$ 1 (White and Hillenbrand, 2004). The SED modeling finds the bolometric luminosity of 3.5$-$15 $L_{\odot}$.

At the (sub)millimeter wavelengths, unlike at the optical wavelengths, the object suffers less from the extinction. Moreover, the HL Tau disk is one of the brightest objects at the wavelength region (Andrews and Williams, 2005). Owing to its brightness, the object has been intensively observed at the wavelength region (Sargent and Beckwith, 1991; Mundy et al., 1996; Lay, Carlstrom, and Hills, 1997; Kitamura et al., 2002; Looney, Mundy, and Welch, 2000; Guilloteau et al., 2011; Kwon, Looney, and Mundy, 2011). The resolved images of the HL Tau disk showed that the disk mass is 0.14 $M_{\odot}$, the characteristic radius 79 au, the inclination 40° and the position angle 136° (Kwon, Looney, and Mundy, 2011). A notable feature of the HL Tau disk, which was revealed by ALMA long baseline observation, is the concentric multi-ringed structure with the spatial scale of $\sim$100 au (ALMA Partnership et al., 2015).

The grain size in the disk was measured by the multi-band observations at the millimeter wavelengths. The spectral index β computed with the Band 6 and 7 continuum exhibits radial gradients (ALMA Partnership et al., 2015): low β is low at the rings and in the central region ($\sim$ 2) and high β at the gap ($\sim$ 3.5). The low β indicates that the rings and the central regions are

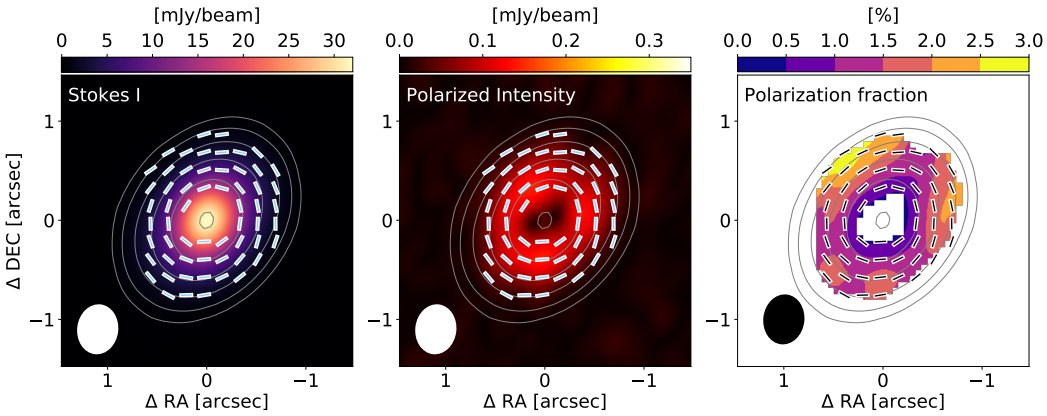

FIGURE 2.1: ALMA Band 3 (λ = 3.1 mm) polarimetric observations of the HL Tau disk, which has been previously reported by Kataoka et al. (2017) and Stephens et al. (2017). The left panel shows the Stokes I intensity in color, the central panel shows the polarized intensity, and the right panel shows the polarization fraction. The solid contours in the three panels are equivalent and represent the intensity with the levels of (10, 25, 60, 150, 366, 900) times the noise level, which is σ_I (= 34 μJy beam^{-1}). The overlaid line segments represent the polarization vectors where the polarized intensity is larger than 3 times the noise level of the polarized intensity, which is σ_{PI} (= 5.3 μJy beam^{-1}). Note that the length of the polarization vectors is set to be equal. The beam has a size of 0.″51 $\times$ 0.″41 and position angle of -6.°76, which is represented in the bottom left as an ellipse.

at least partially optically thick at the wavelengths (Jin et al., 2016; Pinte et al., 2016). Combining the ALMA observations with subsequent observations at longer wavelengths with Very Large Array (VLA), Carrasco-González et al. (2016) showed that the emission at 7 mm is optically thin and spectral index varies location to location indeed. Detailed radiative transfer modeling for the ALMA and VLA images found that the rings are filled with relatively larger grains compared to the gaps (Liu et al., 2017).

2.1.2 Polarized Emission at (Sub)Millimeter Wavelengths on the HL Tau Disk

Given its brightness and intriguing feature (i.e. ringed structure), the polarization observations at millimeter wavelengths on the HL Tau disk have been intensively conducted at multiple wavelengths. We here explain the polarization feature obtained on the disk at 870 μm (Band 7), 1.3 mm (Band 6), and 3.1 mm (Band 7) based on the previous studies (Kataoka et al., 2017; Stephens et al., 2017).

The polarization morphology is strongly dependent on the observation wavelengths, indicating the distinct origins depending on the wavelengths (See Figure 1 in Stephens et al. (2017)). The polarization morphology at 870 μm is mostly parallel to the minor axis of the disk. These features are well reproduced by the self-scattering model for the inclined disk (Kataoka et al., 2016a). This indicates that the size of dust grains reaches as large as $\sim$150 μm in radius (Kataoka et al., 2017; Stephens et al., 2017).

In this study, we investigate the origin of the 3.1 mm polarization on the disk, which is not well understood. Figure 2.1 shows the Stokes I intensity, polarized intensity, and polarization fraction, all of which are overlaid with the polarization vectors. The 3.1 mm polarization morphology is azimuthal. This can be reproduced by grain alignment models, where, for example, some external force directs in the radial directions align the oblate grains with their short axes parallel to the force. However, which alignment force (magnetic fields, radiative gradient, and gas flow) aligns the dust grains is uncertain and being debated. Moreover, Yang et al. (2016) poses a question that the alignment model cannot perfectly reproduce the polarization features obtained on the disk, which we will explain below. The 1.3 mm polarization morphology appears to be a superposition of those at 3.1 mm and 870 μm. The origin of this polarization is also uncertain as well as that at 3.1 mm.

As explained above, what produces the polarized emission is still uncertain especially at 3.1 mm. To ascertain the polarization origin, detailed modeling toward the polarization is necessary. Thus, we employ two approaches, semi-analytical and radiative transfer models. First, we investigate models that can reproduce the polarization features obtained on the HL Tau disk by reconstructing semi-analytical models, which are originally developed by Yang et al. (2016) and Yang et al. (2019). Then, to further investigate and constrain the grain size and shape, we also construct radiative transfer models by using RADMC-3D (Dullemond et al., 2012). Perhaps, one does not need to construct the semi-analytical model for the questions. However, the advantage of the semi-analytical models is to enable us to understand the physics of each model while the radiative transfer modeling is a somewhat black box, and thus we employ the semi-analytical models.

2.2 Method (Semi-analytical and Radiative Transfer Modeling)

In this section, we briefly describe the outlines of semi-analytical and radiative transfer models constructed in this study. First, we describe the semi-analytical models, which are previously developed by (Yang et al., 2016; Yang et al., 2019). Then, we also describe our new radiative transfer models. Note that we describe minimum information to avoid one's confusion and we give a detailed explanation for how to construct the semi-analytical and radiative transfer models in Appendix A and B, respectively.

2.2.1 Semi-analytical Models

In this subsection, we explain the outlines of the semi-analytical models developed by Yang et al. (2016) and Yang et al. (2019). To set a disk model, on which the alignment and self-scattering models are computed, we first introduce a coordinate system. At the system, we assume models of the surface density and temperature profiles, which were derived by Kwon, Looney, and Mundy (2011), which reproduced the continuum observation on the HL Tau disk at 1.3 mm and 2.7 mm obtained with CARMA. We distinctively reconstruct the alignment and self-scattering model on the disk model.

Alignment model:
In the alignment model, two kinds of the non-spherical grains, which are oblate and prolate, are assumed. We also the directions of the external force, which aligns the dust grains. To reproduce the azimuthal polarization morphology obtained on the HL Tau disk, the directions of the force are radial for the oblate grains while those are azimuthal for the prolate grains.

The polarization angle at each location is given by computing to the directions of the force projected on the sky plane. The polarization orientations for the oblate grains are perpendicular to the projected force while parallel to the force for the prolate grains.

We also compute the polarization fraction of the thermal emission coming from the aligned grains at each location. That depends on a viewing angle, which is composed of an alignment axis and the line of sight. The polarization fraction for the oblate grains with a disk-like shape was theoretically derived by Lee and Draine (1985) as

$$p_{ob}(x,y) = \frac{p_0 \times \sin^2 i_d(x,y)}{1 + p_0 \times \cos^2 i_d(x,y)}, \tag{2.1}$$

where p_{ob}(x, y) is expected polarization fraction at a location (x, y), p_0 is maximum polarization fraction and $i_d(x,y)$ is the viewing angle. The maximum polarization p_0 is expected when they are viewed edge-on (i_d = 90°), while no polarization is expected when viewed face-on (i_d = 0°). Lee and Draine (1985) also derived the polarization fraction p_{pro} for the prolate grains with needle-like shape as give by

$$p_{pro}(x,y) = \frac{p_0 \times \sin^2 i_d(x,y)}{1 - p_0 \times \cos^2 i_d(x,y)} \tag{2.2}$$

The polarization fraction reaches maximum when the long axes of the grains are parallel to the plane-of-sky, whereas no polarization are expected when the axes are perpendicular to the plane-of-sky.

Computing the viewing angle at each location, we can predict the spatial distribution of the polarization fraction with Equations 2.1 and 2.2. In these models, the polarization fraction is determined only by the maximum polarization efficiency p_0. Thus, p_0 is the changeable parameter in the alignment model (for both the oblate and prolate grains).

Self-scattering model:
We next construct the self-scattering model. The model assumes that dust grains scatter incoming thermal emission from surrounding grains whose temperature is T. By using radiative transfer equations, we compute the incoming thermal emission around a dust grain and scattered emission The resultant polarization can be computed by solving the radiative transfer equations as we explain in detail in Appendix A. To facilitate the computation of the model, the model put three assumptions: (1) the emitting region is the vertically thin plane, and thus the incoming emission from z-direction is neglected, (2) the emission is optically thin at all radii, (3) the only last scattering contributes to resultant scattered emission. The resultant Stokes I intensity is proportional to the absorption opacity κ_{abs}, and Stokes Q and U intensities are proportional to both absorption opacity κ_{abs} and the scattering opacity κ_{sca}. Thus, to change the contribution from the scattered emission, we

Combined (alignment + self-scattering) model:
To create the combined model, we compute the sum of Stokes Q and U intensity derived for each model. When combining the models, the controllable parameters that determine the intensity of scattered and thermal emission of the aligned grains are absorption/scattering opacity (κ_{abs} and κ_{sca}) and the intrinsic polarization fraction of the aligned grains (p_0). The polarization fraction and morphology in the combined model are determined by how the alignment and scattering contribute to the polarized emission. Between the three parameters, the absorption opacity κ_{abs} determines the absolute intensity for both the emission but does not determine the flux contribution from each emission because the parameter is equally involved in both of the emission. On the other hand, the scattering opacity κ_{sca} and the intrinsic polarization fraction p_0 are involved only in the intensity of scattered and thermal emission of the aligned grains, respectively. Therefore, the resultant polarization fraction and morphology can be modified by changing the parameter κ_{sca} and p_0. We construct the combined model with changing the parameters and compare it with the observed images after the beam averaging is adopted.

2.2.2 Radiative Transfer Models

We construct an axisymmetric disk model that reproduces the stokes I image obtained on the polarization observation at 3.1 mm (Kataoka et al., 2017; Stephens et al., 2017). By assuming that the Stokes I emission at 3.1 mm is optically thin, we construct the radial profile of the optical depth at 3.1 mm with the form of

$$\tau_{model}(r) = \tau_0 \left(\frac{r}{1\,\mathrm{au}}\right)^{-\gamma_1} \exp\left[\left(\frac{r}{r_c}\right)^{-\gamma_2}\right], \tag{2.3}$$

with the temperature profile of $\mathrm{T(r)} = 310\,(\mathrm{r/1\,AU})^{-0.57}$ K (Okuzumi and Tazaki, 2019).

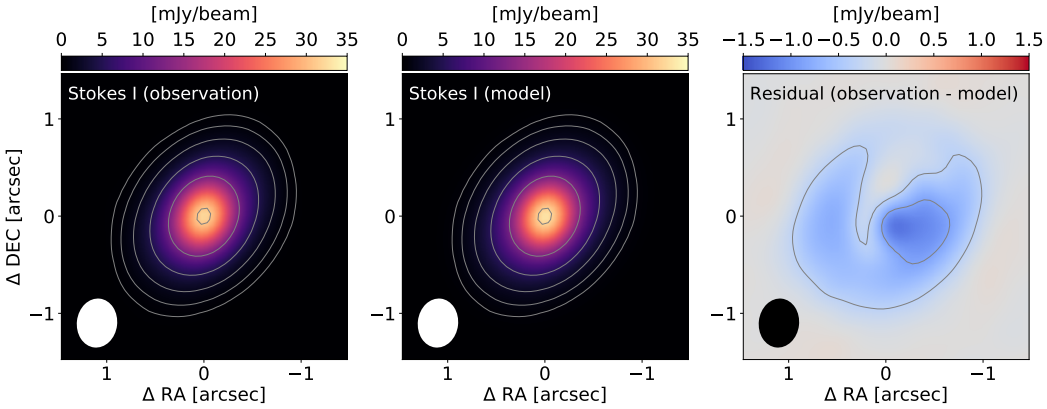

FIGURE 2.2: The left panel shows the Stokes I image of the observations, the central panel shows the model image, and the right panel shows the residual map where the observed Stokes I subtracted with the model image. The contours of the left and the central panels are the same as Fig.2.1 and the contour of the right panels show the residual levels of (-10, -25) $\times$ σ_I

.

We adopt the parameter set of $((\tau_0, r_c, \gamma_1, \gamma_2))$ = (1.0, 129.2, 6.6, 9.0), which reproduces the Stokes I emission. Figure 2.2 shows the images of observed and modeled Stokes I produced assuming the parameter set and residual.

While the residuals are still significant, they show axisymmetric distribution. For this study, we aim at reproducing the continuum emission with an axisymmetric model for simplicity, and thus we do not further search the parameter sets.

We use a grain composition model developed by Birnstiel et al. (2018), where the grains are the mixture of silicate, troilite, organics, and water ice. The refractive index used in the calculation is as follows: Draine (2003) for astronomical silicate, Henning and Stognienko (1996) for troilite and refractory organics, and Warren and Brandt (2008) for water ice. We compute the mixture of them with the effective medium theory using the Maxwell-Garnett rule (e.g., Bohren and Huffman (1983) and Miyake and Nakagawa (1993)). We assume the grains have a power-law-size distribution with a power of q = -3.5 (Mathis, Rumpl, and Nordsieck, 1977) with the maximum grain size of a_{max}, while the minimum grain size is fixed at a_{min} = 0.05 μm.

To reproduce polarization, we consider both alignment and scattering induced polarization. For the alignment-induced polarization, we consider both prolate and oblate grains. We assume the axes ratio of the grains to be $\alpha = 0.9$ for prolate grains and $\alpha = 1.1$ for oblate grains and that the alignment efficiency to be $\epsilon = 0.6$ (see Appendix B for the details). We further assume that the oblate grains are aligned with their short axis parallel to the radial direction of the disk while the prolate grains are aligned with their long axis parallel to the azimuthal direction of the disk. Note that theoretical

studies suggest oblate grains, which have two longer axes than the other, to be considered because the spinning motion of dust grains leads to be an effectively oblate shape. As we will show in the following, however, considering prolate grains, which have one longer axis than the other two, is essential in explaining the HL Tau polarization.

The scattering-induced polarization is included by turning on the scattering in the radiative transfer simulations. We treat the full phase function and take into account the multiple scattering. The controlling parameter of the scattering is the maximum grain size, a_{max}. The self-scattering polarization is the most effective when the maximum grain size is $a_{max} \sim \lambda/2\pi$.

We assume spherical dust grains for computing self-scattering while we assume oblate or prolate grains for computing alignment-induced polarization. These are not consistent but we neglect the effects of scattering by non-spherical grains for simplicity. The angle-averaged absorption opacity of oblate/prolate grains is set to be the same as the spherical grains.

We also note a technical treatment. The radiative transfer code RADMC-3D allows users to compute the alignment-induced polarization only when the dust scattering is turned on. To reproduce the alignment-induced polarization without scattering, therefore, we use $a_{max} = 50$ μm with the scattering turned on, where the scattering-induced polarization is negligible.

2.3 Results

In Section 2.2, we have reconstructed the semi-analytical alignment and self-scattering models, originally developed by Yang et al. (2016) and Yang et al. (2019). We have also developed new radiative transfer models. First, by using the semi-analytical models, we examine whether (1) the alignment model reproduce the HL Tau polarization in Band 3, if not, (2) the observed polarization can be reproduced by adding the scattering to the alignment model, and we finally discuss (3) which the oblate or prolate grains is preferred. Then, by using the radiative transfer models, we further examine the above questions and set constraints on the grain properties including size and shape.

2.3.1 Can the Alignment Models Reproduce the HL Tau Polarization ?

First, we discuss whether the alignment models can produce the HL Tau polarization observation in Band 3 without invoking the self-scattering model. Yang et al. (2019) showed that the HL Tau polarization observation cannot be reproduced only by the alignment models. Here, we independently check the statement with our reconstructed analytical models. We compare the observation with the reconstructed models concerning the polarization morphology and fraction.

Figure 2.3 shows images of the polarized intensity and polarization fraction assuming the oblate and prolate grain models, where $p_0 = 0.1$ (10%).

To facilitate the comparison with the polarized intensity images, the polarization fraction is shown only where the distance is within 1.″1, where the polarized intensity is larger than $\sim$ 5 mJy/beam, for both the models. We note that the beam position angle is rotated with 90° because the disk position angle is assumed to be 90° in the analytical model. We examine both the models in terms of the polarization pattern and fraction.

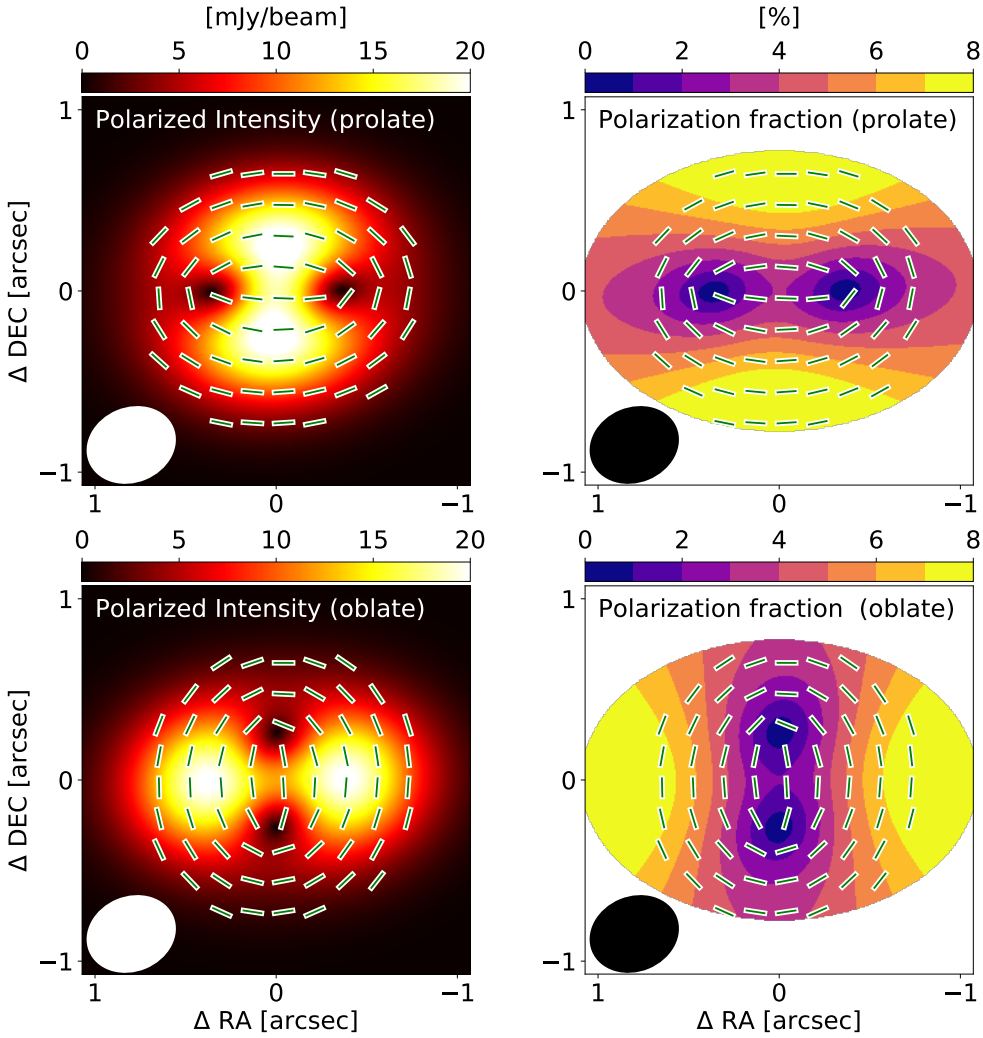

FIGURE 2.3: Semi-analytical models of the HL Tau disk polarization assuming the prolate and oblate grain models with p_0 = 0.1 (10%). The images of polarized intensity and polarization fraction are shown in the left and right columns, respectively. The polarization vectors are also overlaid with the image for respective grain model.

The polarization morphology shown in the images reflects the differences in the directions of the flow and grain alignment axes. The prolate grains are aligned by the azimuthal flows with their major axes parallel to the flow. The azimuthal flows viewed at inclined appears to be elliptical flow for the observer, and thus the resultant morphology is elliptical. The oblate grains, on

the other hand, the radial flows align the grains with their major axes perpendicular to the flow. The radial flows always directs from the central regions even if the flows are viewed at inclined, resulting in the circular pattern. We note that beam dilution affects the pattern particularly in the inner regions of the disk of oblate grain models. We confirm that the elliptical pattern, which is compatible with the observed pattern can be reproduced by the prolate grain model whereas it cannot be reproduced by the oblate grain model.

The polarization fractions and polarized intensity, however, show strong variations in the azimuthal directions for both the models. The prolate grain model shows higher polarization along the minor axis. It is because that the alignment axes of the grains are perpendicular to the line of sight in the minor axis, whereas those are inclined concerning the line of sight in the major axis. The oblate grain models, on the other hand, shows higher polarization along the major axis. It is because contrary to the prolate grain model, the alignment axes of the grains are perpendicular to the line of sight in the major axis whereas those in the minor axis are viewed inclined. The predicted difference in the polarization fraction between the two axes reaches $\sim$50%, which would be large enough to be observed. Therefore, we confirm the statement by Yang et al. (2019) that neither the prolate and oblate grain models cannot reproduce the observed polarization on the HL Tau disk.

2.3.2 The Combination of the Alignment and Scattering Models

Next, we discuss a possibility that a mixture of the alignment and self-scattering models can reproduce the HL Tau polarization, which has not been examined so far. Moreover, we also discuss which oblate or prolate grains are preferable to the observation.

In the combined models, the polarization pattern and fraction are determined by how degree the self-scattering and alignment models contribute to the polarization. The intensity of the thermal emission of the aligned grains is controlled by the intrinsic polarization fraction p_0 and the absorption opacity κ_{abs}. On the other hand, the intensity of the scattered emission is controlled by the scattering opacity κ_{sca} as well as κ_{abs}. Since both the models equally depend on κ_{abs}, the contribution from scattered emission relative to the thermal emission is determined only by κ_{sca} at a given p_0. Changing the three parameters, we can modify the relative importance of the two models as well as the absolute intensity of the polarized emission. Note that we intend not to reproduce the absolute intensity of the polarized emission but to reproduce the observed pattern and azimuthally uniform intensity, which is dependent only on κ_{sca} when p_0 is fixed. Thus, we change the contributions of the scattering model by changing just κ_{sca} while we fix the other parameters at $\kappa_{abs} = 1.$ and $p_0 = 0.1$ (10%).

First, we show the results of combined models, where the prolate grains are assumed.

Figures 2.4 and 2.5 show polarized intensity and polarization fraction of mixture model, where the prolate grains are assumed. From the top-left to

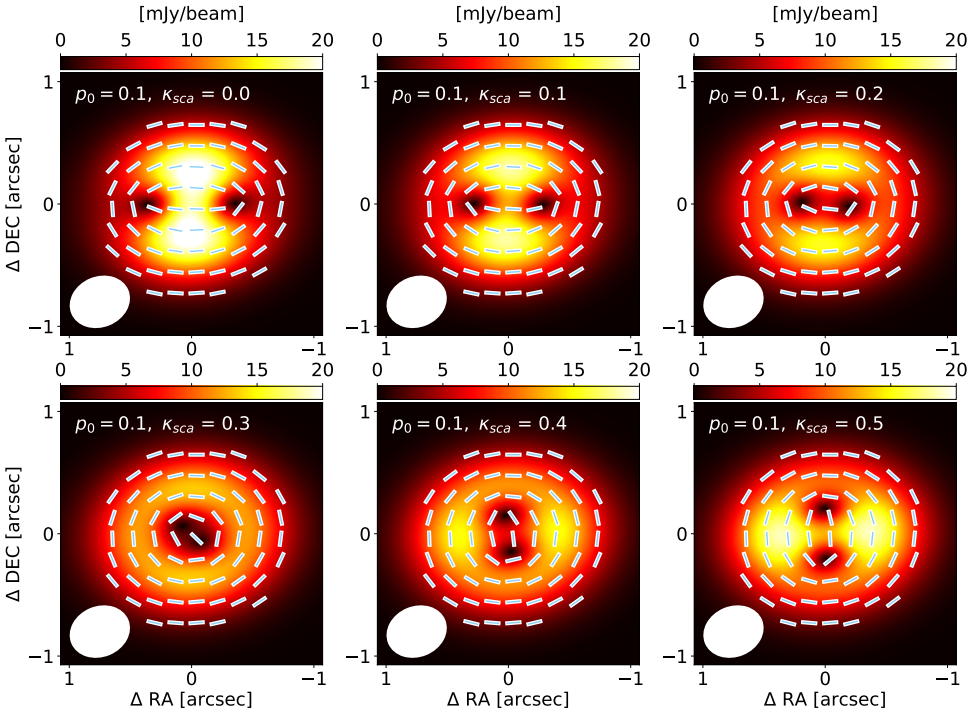

FIGURE 2.4: The polarized intensity of models that combine the grain alignment (prolate grains) and self-scattering, each of which is convolved with the beam displayed with the white ellipse. The contribution of the scattered emission increases with κ_{sca} from top-left to the bottom-right panels.

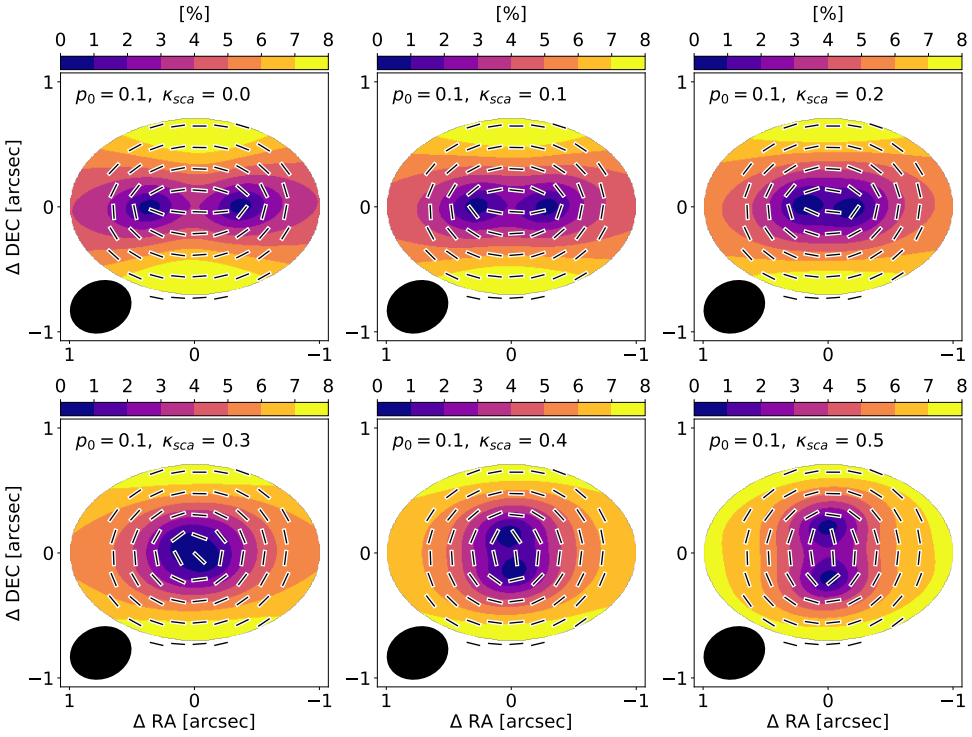

FIGURE 2.5: Same as Figure 2.4 but for polarization fraction.

the bottom-right, the scattering components are increased by increasing the scattering albedo from $\kappa_{sca} = 0$ (no scattering) to $\kappa_{sca} = 0.5$.

The images of no self-scattering model (the top-left images) are identical to upper panels of 2.3. As κ_{sca} increases, the scattered emission contributes to the total polarization especially along with the major axis. This gradually compensates the polarized emission in the major axis, where the prolate grain model produces weaker polarization compared to the minor axis, approaching the azimuthally uniform polarization. At $\kappa_{sca} = 0.3$ model (bottom-left), the images of the polarized intensity and polarization fraction exhibit azimuthally uniform polarization, both of which capture the observed feature. At more larger κ_{sca}, the scattering components start to exceed the thermal emission, resulting in the elongated distribution along with the major axis.

In all the images, the elliptical polarization pattern is almost sustained in the outer region although that is modified in the inner regions probably due to beam dilution. Therefore, we find that there is at least one solution to reproduce the polarization feature obtained on the HL Tau disk (elliptical pattern and uniform polarization fraction in the azimuthal directions) when we assume the grain aligned by a flow and a certain fraction of scattering emission.

We also develop combined models assuming the oblate grains aligned by the radial flow. The results are shown in Figures 2.6 and 2.7 as done in the prolate grain model. Unlike the prolate grain model, even if the scattering components increase, the polarization becomes higher in the major axis but not in the minor axis. This is a natural consequence of the fact that both of the self-scattering and alignment models (oblate grain) produce polarization elongated distributions along with the major axis. Moreover, the polarization patterns in the outer regions remain almost circular in all the images, which is also inconsistent with the observed pattern. Therefore, for both of the polarization morphology and polarization fraction, there are no solutions to reproduce the polarization feature on the HL Tau disk as long as we assume the oblate grain model.

We here summarize that (1) oblate grain model + radial flow can be excluded as an appropriate model for the HL Tau disk (2) the prolate grain model + azimuthal flow has the solution to reproduce the HL Tau polarization by including the scattered emission. As a next step, we investigate appropriate grain parameters such as grain size, grain shape, and alignment efficiency. The semi-analytical model computed so far is inappropriate to conduct parameter search with wide dynamic ranges. Therefore, in the next section, we develop radiative transfer models and constrain the grain property by comparing RAT models and observation.

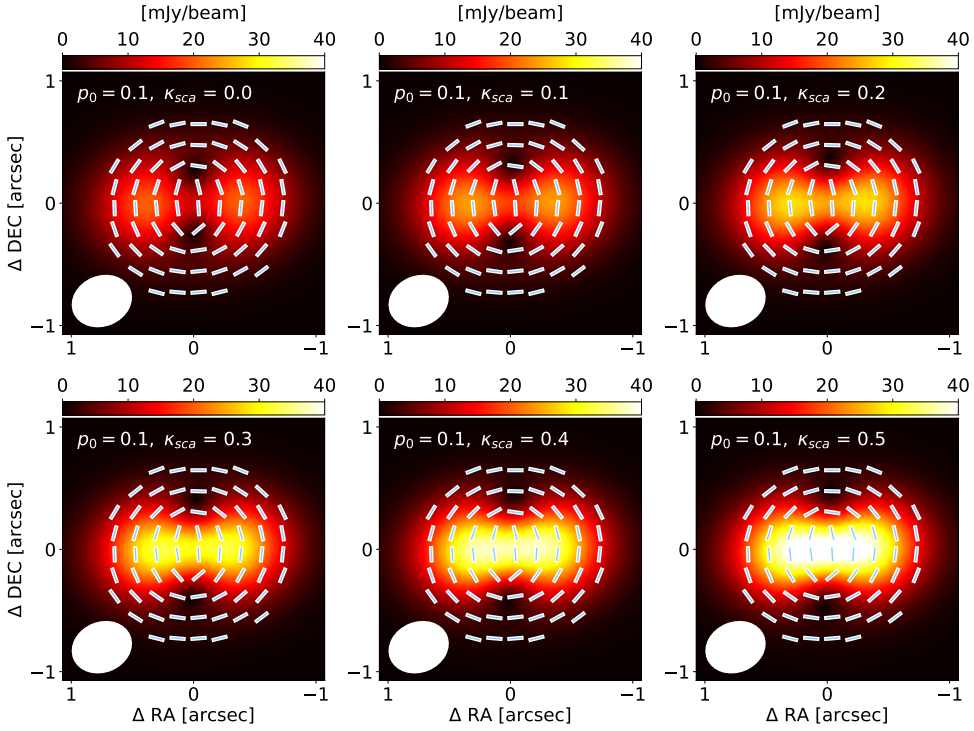

FIGURE 2.6: The polarized intensity of models that combine the grain alignment (oblate grains) and self-scattering. The contribution of the scattered emission is gradually increased as in Figure 2.4.

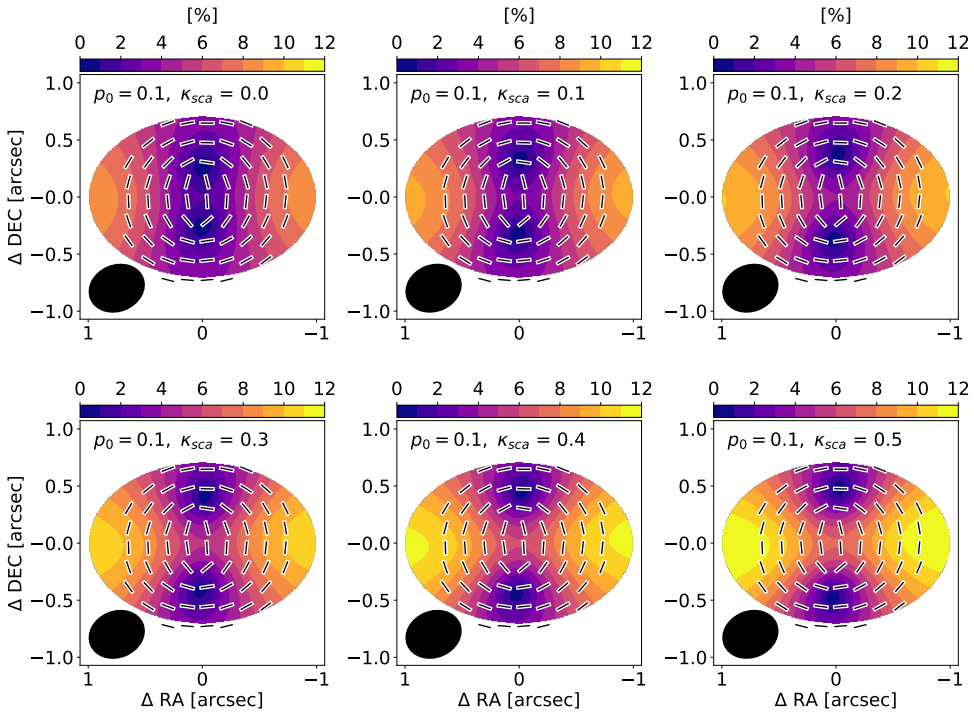

FIGURE 2.7: Same as Figure 2.6 but for polarization fraction.

2.3.3 The Radiative Transfer Models Assuming just the Grain Alignment

With the semi-analytical models, we have already shown that the grain alignment models cannot reproduce the HL Tau polarization. In the models, however, we fixed the grain properties, which determine the degree of the azimuthal polarization variations. On the other hand, our radiative transfer models enable us to change the three parameters, the grain size a_{max}, grain axis ratio α, and grain alignment efficiency ϵ. The parameter α determines the degree of the polarization azimuthal variations in the azimuthal directions. Therefore, to confirm that the alignment model cannot produce the uniform polarization in the azimuthal directions indeed, we investigate a possibility that almost spherical grains ($\alpha \sim 1$) produce azimuthally uniform polarization for both the prolate and oblate grain models.

First, we examine if the prolate grain model can reproduce the azimuthally uniform polarization fraction. Figure 2.8 shows images (left column) and corresponding radial profiles (right column) of polarization fraction. The profiles show the radial distributions along with the major (red) and minor axes (blue). The observed polarization fraction along with the two axes is also presented. From top to bottom rows, the grain shapes become almost spherical by reducing the axis ratio from $\alpha = 1.15$ to $\alpha = 1.05$, while ϵ is fixed at unity. As the grains become spherical, the polarization fraction in the whole disk decreases because the differences of the absorption opacities along with the long and short axes of the dust grains decrease.

These images and profiles obviously show that the azimuthal variations of the polarization fraction remain even if the grain shape is almost spherical. The profile of the major axis with $\alpha = 1.1$ (second row) shows good agreement with the observed profile, but that of the minor axis does not consistent with the observed profile. When the grain becomes more spherical, the model profile of the minor axis agrees well with the observed profile, but instead that in the major axis does not consistent with the observation. Therefore, we conclude that the alignment model with the oblate grains cannot reproduce the observed polarization.

Next, we assume oblate grains in the alignment model. Figure 2.9 shows the images and profiles as in Figure 2.8. The grain shape approaches spherical from the upper to bottom panels as in Figure 2.8 from $\alpha = 0.85$ to $\alpha = 0.95$. As well as the prolate grains, the models with the oblate grains also predict the azimuthal variations in the azimuthal directions. Therefore, we conclude that azimuthally uniform polarized emission cannot be reproduced by the grain alignment models whether the grains are oblate or prolate. This is the same conclusion as described in Yang et al. (2019) and the former subsection.

2.3.4 Combined Model (Grain Alignment + Self-scattering)

Since we confirm that the alignment models cannot reproduce the HL Tau polarization by themselves, we construct the model that combines the alignment and scattering models. With the semi-analytical model, the oblate grain

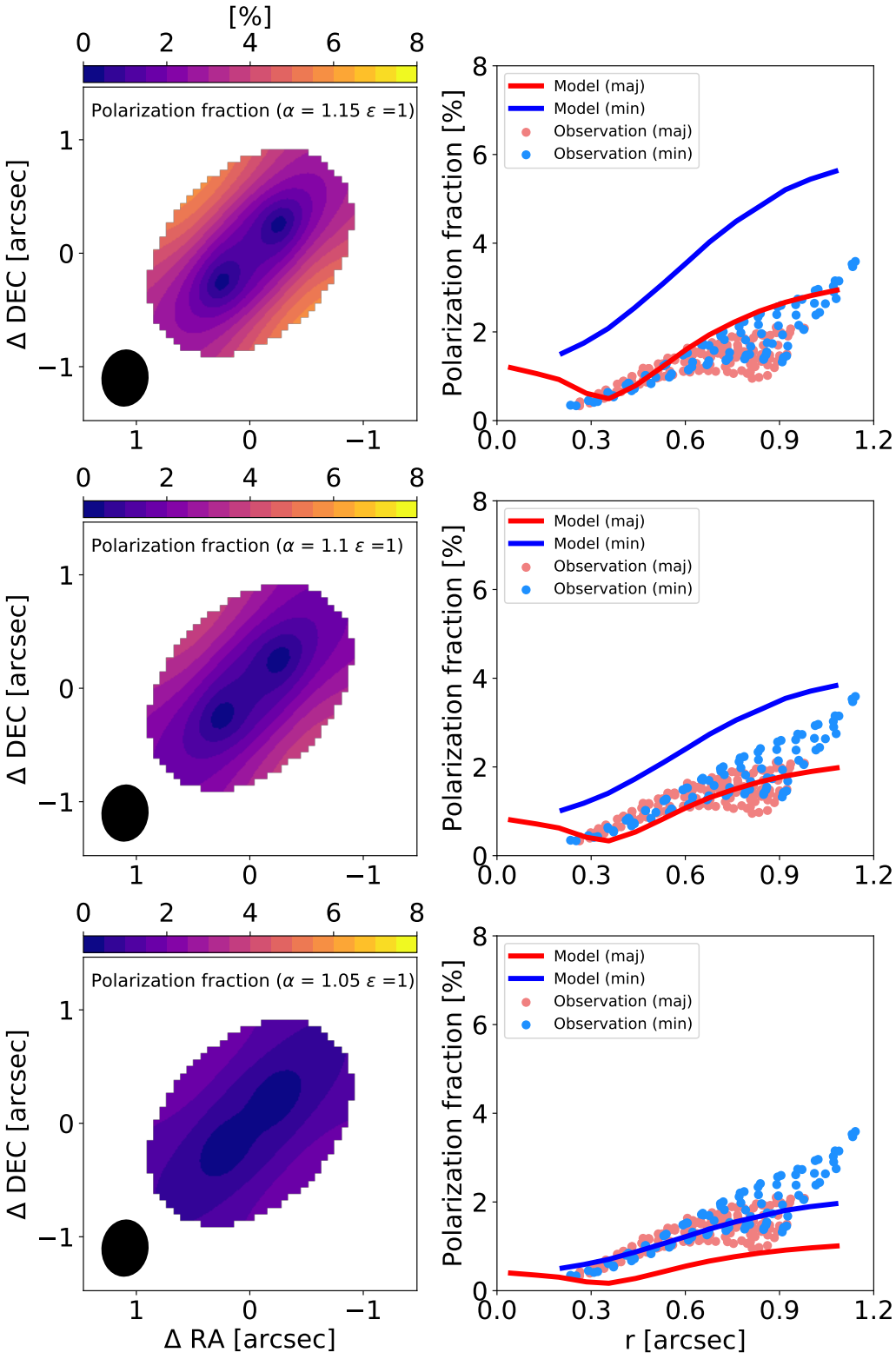

FIGURE 2.8: Left columns: Polarization fraction of models with prolate grains. From upper to bottom panels, the grain shape approaches spherical with decreasing α while the alignment efficiency is fixed at $\epsilon = 1$. Right columns: Radial profiles of the polarization fraction of the left images. The red and blue solid lines represent the profiles along with the major and minor axes, respectively. The observed polarization fraction in the major and minor axes are also shown with red and blue dots, respectively.

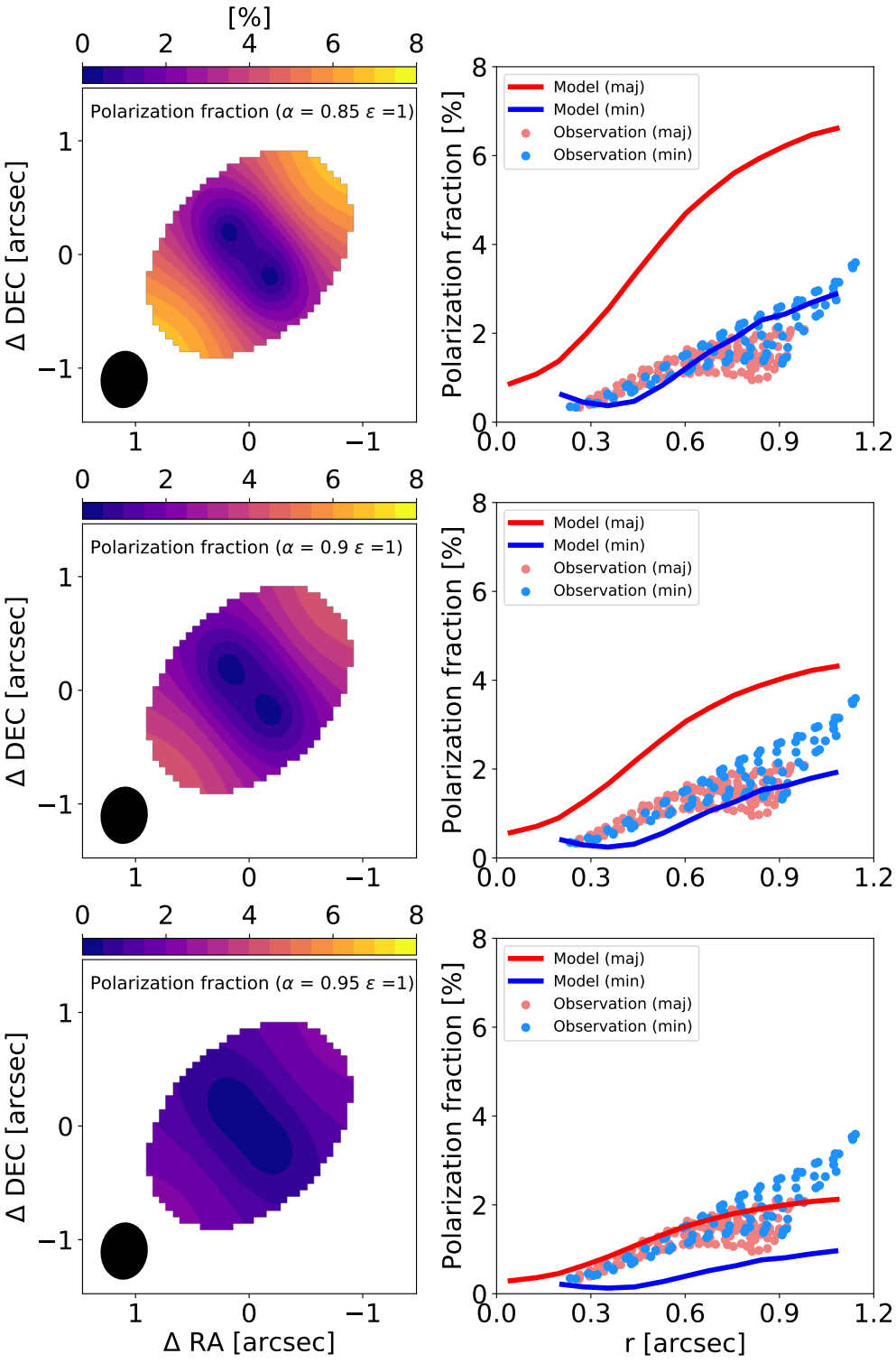

FIGURE 2.9: Left columns: Polarization fraction of models with prolate grains. From upper to bottom panels, the grain shape approaches spherical with increasing α while the alignment efficiency is fixed at $\epsilon = 1$. Right columns: Radial profiles of the polarization fraction of the left images. The red and blue solid lines represent the profiles along with the major and minor axes, respectively.

model has been already excluded, and thus we assume only the prolate grain model in the following.

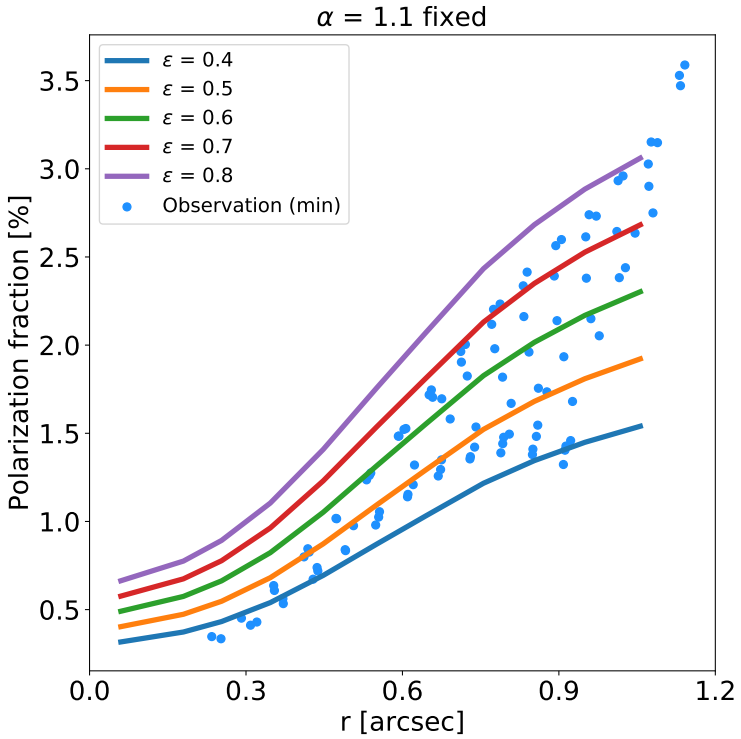

FIGURE 2.10: Radial profiles of the polarization fraction along the minor axis. The blue dots show the observed radial distribution along with the minor axis. The solid lines show the same profiles produced by the RAT models with $\epsilon = 0.4-0.8$.

With the constructed radiative transfer models, we distinctively execute the ray-tracing for the alignment and self-scattering models, and then we combine the two models. As explained in Section 3.3, the polarized emission in the outer regions dominantly comes from the aligned prolate grains along the minor axis and the scattering grains along the major axis. Thus, we first roughly fit the polarization fraction profile in the outer region of the minor axis only with the alignment model.

The changeable parameters in the alignment model are α, ϵ, and a_{max}. Of these parameters, we cannot find a unique solution for α and ϵ. This is because they degenerate to each other: almost spherical grains ($\alpha \sim 1$) + high ϵ and elongated grains + low ϵ should predict similar polarization fraction. Thus, we temporarily fix the grain shape to almost spherical with $\alpha = 1.1$ and search for appropriate ϵ that best reproduce the profile along the minor axis.

The maximum grain size a_{max} is another parameter, which determines the polarized intensity. However, because ray-tracing of the grain alignment model with RADMC-3D always computes grain scattering, we cannot simulate the polarized emission that purely comes from the aligned grains. Therefore, to virtually switch off the scattering, we fix the size at $a_{max} = 50$ μm for the alignment model, where the scattering opacity is negligible relative to the absorption opacity.

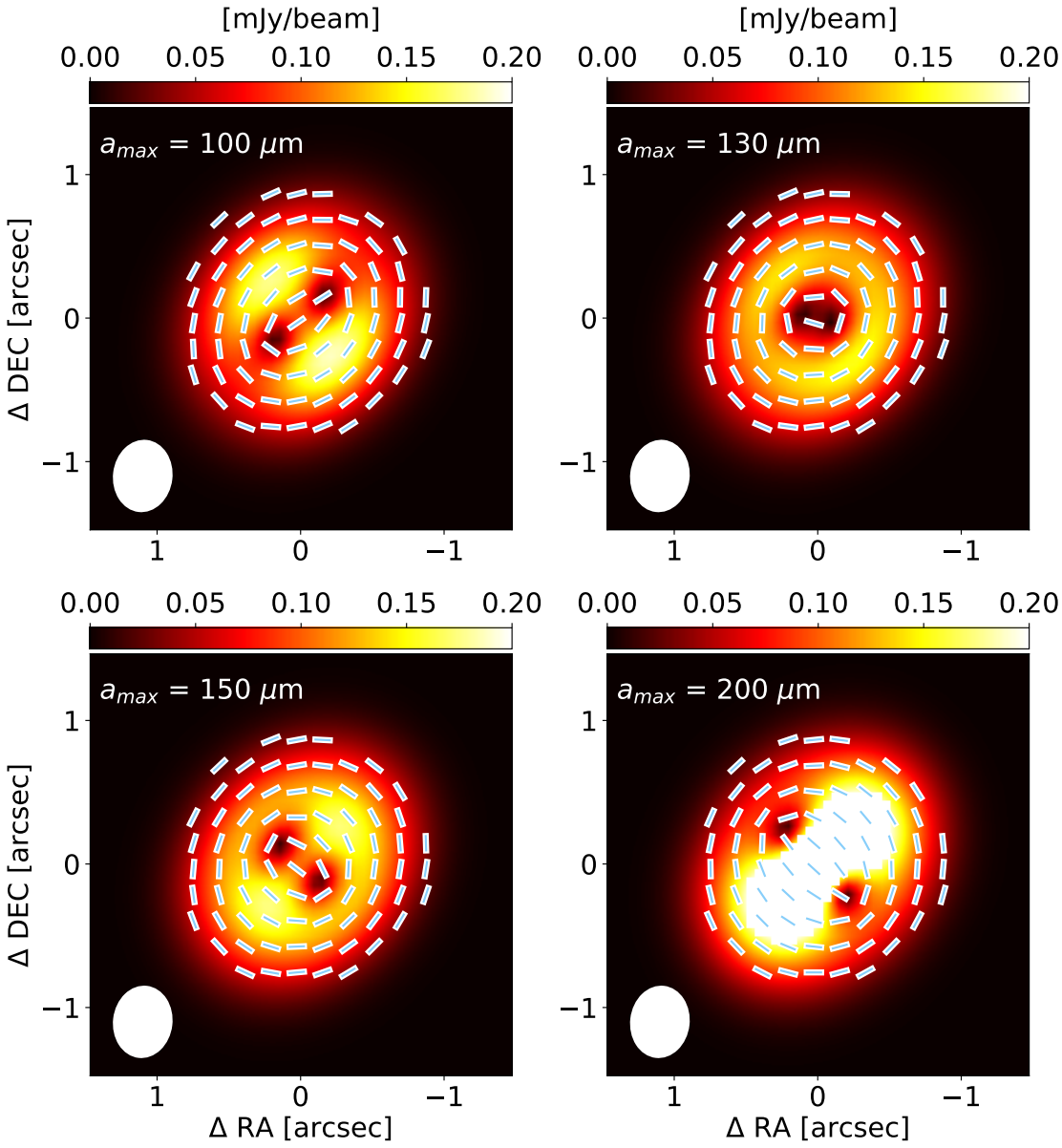

FIGURE 2.11: Polarized Intensity of models that combine the grain alignment (prolate) and self-scattering. The contribution of the scattered emission gradually increases with a_{max} = 100 μm, 130 μm, 150 μm, and 200 μm from top-left to bottom-right.

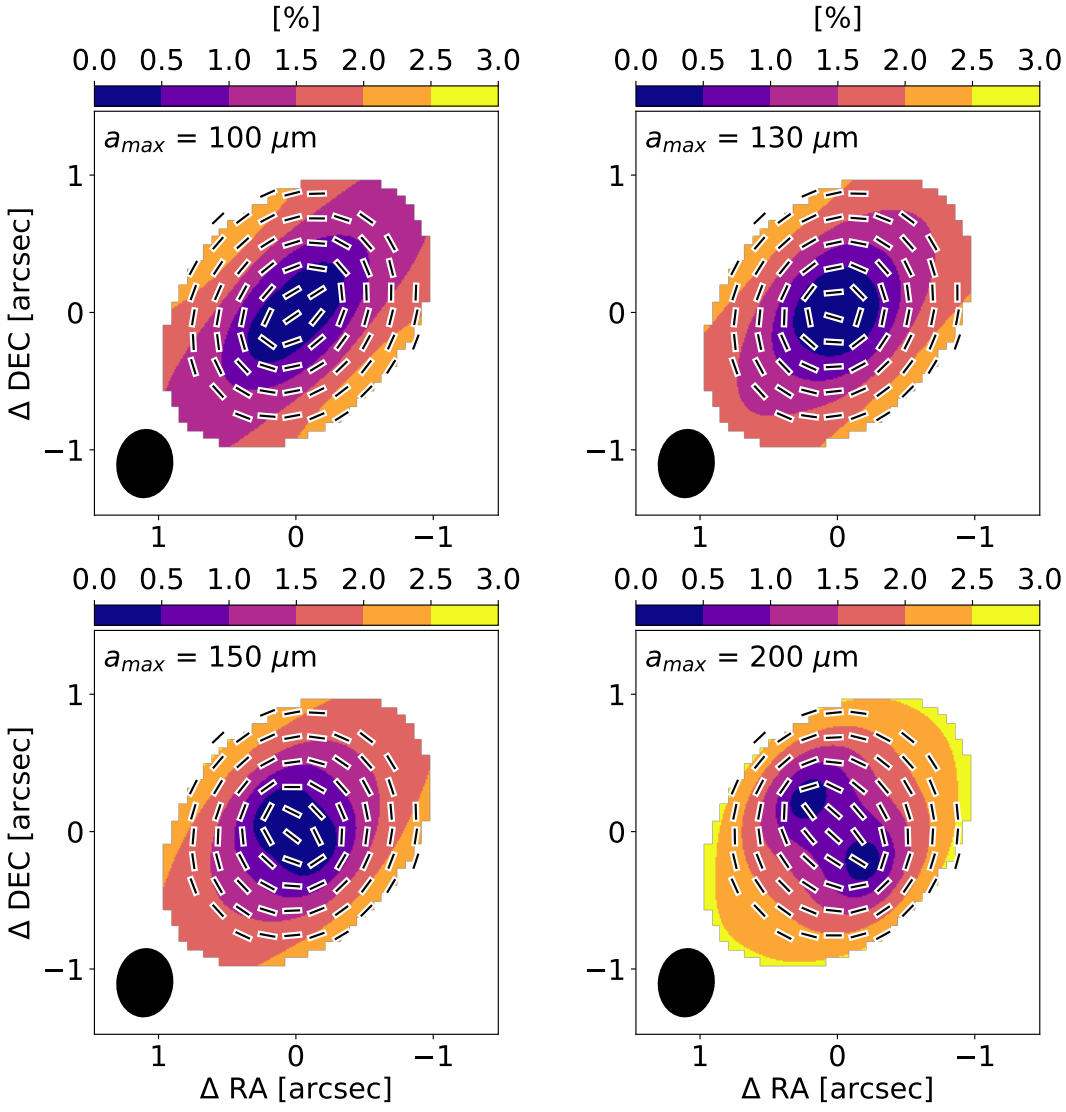

FIGURE 2.12: Same as Figure 2.11 but for polarization fraction.

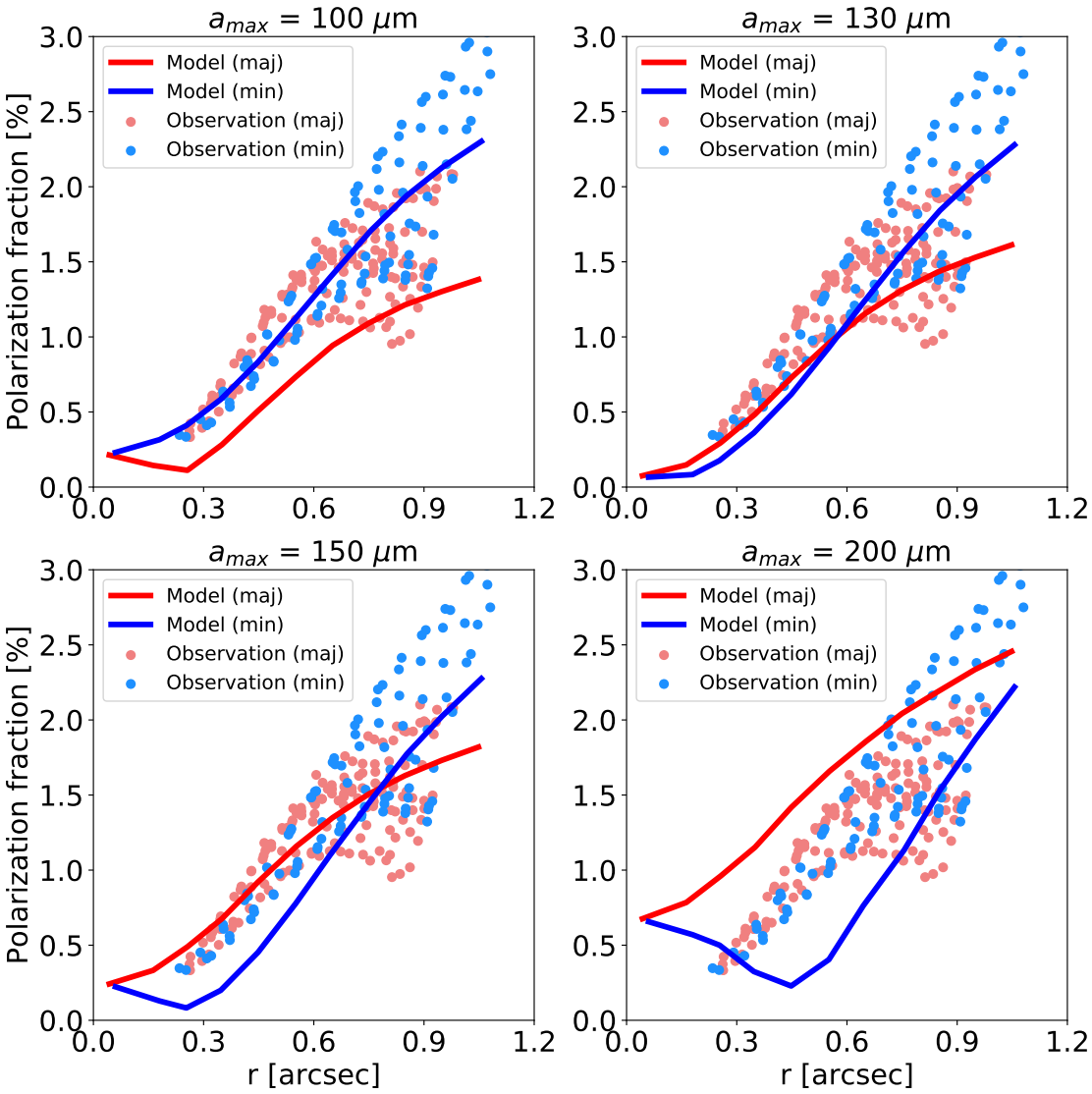

FIGURE 2.13: Radial profiles of the polarization fraction in Figure 2.12 along the major (red) and minor (blue) axes. The observed polarization fractions in the major and minor axes are also presented in red and blue, respectively.

Figure 2.10 shows the profiles of the polarization fraction along the minor axis produced by the alignment model with $\epsilon = 0.4-0.8$. The observed radial distribution of the polarization fraction is also shown in the Figure. This represents the acceptable ϵ range when grain shape is fixed at $\alpha = 1.1$. From this figure, we find that the models with $\epsilon = 0.4-0.8$ roughly consistent with the observed radial distribution. In the following, we adopt $\epsilon = 0.7$ as the representative value in the alignment model.

Finally, we compute the scattering model. The polarization fraction in the scattering model is determined by the maximum grain size of a_{max}. The polarization fraction is predicted by self-scattering model reaches maximum when $a_{max} \sim \lambda/2\pi$. Thus, the contribution of the scattered emission can be increased by increasing a_{max} until it reaches $a_{max} \sim 500$ μm. We gradually add the scattered emission to the alignment model with $\alpha = 1.1$ and $\epsilon = 0.7$ and search for a_{max} of the scattering grains that best reproduce the azimuthally uniform polarized fraction while the other parameters.

Figures 2.11 and 2.12 shows the images of the polarized intensity and polarization fractions for the combined models. From the upper-left to the bottom-right images, the contribution of the scattered emission gradually increases with a_{max}. As shown in Figures 2.11 and 2.12, when the grain size is $a_{max} = 100$ μm, where the contribution from scattering is smaller than that from the aligned grains, resulting in the stronger polarized emission in the minor axis compared to the major axis. As the grain size of the scattering grains increases, the scattered emission becomes comparable to the thermal emission of the aligned grains. Consequently, the azimuthally uniform polarization fraction is realized when $a_{max} = 130$ μm. As shown in the bottom two images, the models with $a_{max} = 150$ μm and $a_{max} = 200$ μm predict the azimuthal variations and fail to reproduce the observed azimuthal distribution.

We also find that the polarization pattern sustains the elliptical pattern even in the combined model. Therefore, we find that the combined model assuming prolate grain and scattering can produce the uniform polarization in the azimuthal directions. Moreover, the maximum grain size is $a_{max} = 130$ μm which reproduce the observed polarized intensity and polarization fraction.

2.4 Discussion

Our main findings on the HL Tau polarization through the semi-analytical and radiative transfer modeling are as follows.

1. The HL Tau polarization can be reproduced with the combination of the alignment and self-scattering models.

2. The preferable alignment model is that prolate grains are aligned by some external sources in the azimuthal directions.

3. In contrast, the model where the oblate grains aligned by radial sources

are excluded from the HL Tau polarization.

4. The maximum grain size that is constrained to be a_{max} = 130 μm, which can reproduce the azimuthally uniform polarization fraction.

In the following, we discuss the grain properties, disk environment and implications for planetesimal formation based on our results.

2.4.1 The Alignment Model

Theoretically, the external sources, which can align the dust grains are magnetic fields, radiation gradient, and gas flow. As explained in Section 1.4, the possible models to produce the azimuthal polarization morphology is (1) oblate grains aligned by radiation gradient or gas flow in the radial directions and (2) prolate grains aligned by gas flow in the azimuthal directions (Gold alignment). Since our results prefer the prolate grain aligned by azimuthal sources, we find that the promising theoretical model is the Gold alignment model, and thus the alignment source is the gas flow acting on the dust grains.

This means that (1) the timescale of the Gold alignment is short enough compared to that of gas damping timescale to efficiently align the grains; moreover (2) the timescale of the Gold alignment is the shortest in the other alignment processes with the dust spinning (oblate grain models). As described in Section 1.4, the helical grains tend to be aligned with the axes with the shortest precession timescale. Roughly speaking the precession timescale is determined by the strength of an external force working on dust grains and helicity of dust grains. Of these parameters, the helicity of dust grains has been poorly constrained and has large uncertainty (Lazarian and Hoang, 2007; Das and Weingartner, 2016; Hoang, Cho, and Lazarian, 2018). The fact that the Gold alignment model is preferred indicates that the dust grains do not spin around any external sources but instead points to the gas flow.

However, this interpretation has some difficulties in terms of theories of grain alignment and dynamics. One difficulty is that theoretically, the Gold alignment occurs only when the gas speed on the dust grains is supersonic whereas that is generally subsonic in protoplanetary disks (Cho and Lazarian, 2007). Our results and interpretation contradict the theoretical prediction, posing a question in the general grain alignment theories.

The other difficulty is the directions of the gas flow on the dust grains. The gas velocity on dust grains is determined by the Stokes number, which is the grain friction time normalized by the local Keplerian time. Figure 2.14 presents the the radial and azimuthal components of relative velocity of dust grains against gas, which is derived with Equation 1.45 and 1.46 in Section 1.2. Note that the radial distributions of the density and temperature were assumed to be smooth when the two equations were derived.

With Equation 1.26, we can obtain the Stokes number as follows. We have already estimated the grain size to a_{max} = 130 μm in the outer region with

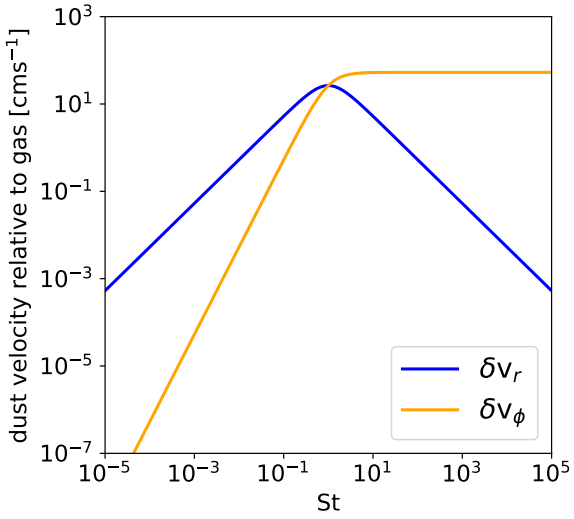

FIGURE 2.14: The radial and azimuthal components of the relative velocity of dust grains against gas. ηv_K in Equation is 1.45 and 1.46 assumed to be 50 ms^{-1}.

the assumed grain internal density of ρ_s = 3 gcm^{-3}. We estimate another parameter, gas surface density by multiplying the dust surface density by the canonical dust-to-gas ratio (=100). In the outer region, the dust surface density was estimated to be $\Sigma_d \sim 0.2$ gcm^{-2} (Pinte et al., 2016; Carrasco-González et al., 2019), and thus the gas surface density is derived to be $\Sigma_g \sim$ 20 gcm^{-2}. Inserting those values to the equation 1.26, the Stokes number is derived to be St = 5×10^{-3}, which is much smaller than unity.

In such a small St range, as shown in Figure 2.14, the directions of gas velocity on grains are predicted to be radial ($\delta v_r \gg \delta v_\phi$) when we assume the smooth surface profile for the surface density and temperature. However, our modeling has found that the directions of the relative velocity are dominantly in the azimuthal directions ($\delta v_r \ll \delta v_\phi$), which is incompatible with the theory.

We here summarize that although the Gold alignment is a unique model to reproduce our obtained results, the model also has difficulties. This pose questions our understandings of the grain alignment and dynamics theories. Future theoretical works need to investigate other models to explain our results without the contradictions to the theory explained above. At the same time, observational works that investigate the origins of azimuthal morphology for other targets as conducted in this work are also necessary. Our models are applicable to other disks just by changing the disk parameters.

2.4.2 The Dust Size in the HL Tau Disk

The grain size in the HL Tau disk has been constrained with the continuum observations at millimeter wavelengths. As explained in Section 1.4, the polarized emission was detected in Band 7 (λ = 870 μm) and Band 6 (λ = 1.3 mm) as well as Band 3 (λ = 3.1 mm). The polarization pattern in Band 7 is

parallel to the disk minor axis with the polarization fraction of $\sim$0.6$-$0.8%. This suggests that the scattering-induced polarization dominates the polarized emission at the wavelength and the presence of grains with a size of $\sim$150 μm (Kataoka et al., 2015; Stephens et al., 2017). With the spectrum of the polarization fraction obtained at λ = 870 μm, 1.3 mm and 3.1 mm, Kataoka et al. (2016a) and Kataoka et al. (2017) estimated the grain size and reached similar results with $a_{max} = 100 - 150$ μm. Although there is a certain difference in the estimation possibly due to differences of assumed disk or grain models, the studies using millimeter-wave polarization as well as this study all find that $a_{max} = 100-150$ μm.

Note that the polarization pattern in Band 6 appears to consistent with the combination of the alignment and scattering model (Stephens et al., 2017), showing a transition from the scattering-dominated polarization in Band 7 to the alignment-dominated polarization in Band 3. This indicates that the contribution from thermal emission of the aligned grains gets to be comparable to that from the scattered emission and further supports the above estimation result. It is because bigger dust grains produce scattered emission at the longer wavelengths, resulting in the same pattern in Band 7. As future works, simultaneous modeling for the polarized observation in Band 3, 6 and 7 as is done in this study may provide further constrain the grain properties like grain composition or internal density.

Spectral indices are the conventional way to constrain the grain sizes and have been measured for various disks. However, one drawback of the measurement is that optically thick emission contributes to the continuum emission, which makes it difficult to constrain the grain sizes. In fact, in the HL Tau disk, Pinte et al. (2016) and Liu et al. (2017) have revealed that the emission is partially optically thick especially in the central regions and rings. To avoid the effect, besides the ALMA images, the latest radiative transfer modeling conducted by Carrasco-González et al. (2019) includes the high resolution observation at 7.0, 9.0 and 13.0 mm obtained on VLA, in which the emission is revealed to be optically thin (Carrasco-González et al., 2016). They conducted detailed SED analysis, which also considers the effect of scattered emission, and found the radial gradient of the grain sizes from a_{max} = 1.5 mm in the inner region to a_{max} = 500 μm in the outer region. Since we have obtained $a_{max} \sim 130$ μm in the outer region, estimation from the spectra is five times larger than that from polarized emission. When we put such large grains in the outer region, the resultant polarization is dominated by scattering-induced polarized emission, which is far from the observed features.

Primary differences between Carrasco-González et al. (2019) and our study are that we analyze the image with coarse angular resolution compared to the images in Carrasco-González et al. (2019) and that we assume the profile of the optical depth and temperature whereas Carrasco-González et al. (2019) analyze the emission profile without such assumptions. Of course, these differences could partially explain the discrepancy in the grain size measurements. As well as such basic differences, the assumption on grain compositions also can affect the measurement.

One possible solution without modifying those assumptions in these works is a model with several grain populations with different a_{max}. The grain population of the maximum size of a_{max} = 500 μm inferred from the spectrum is thought to be settled down while the other population with a_{max} = 130 μm is stirred up relative to the large population. The grain settling reduces the polarization fraction because the incoming flux directed on a scatterer becomes isotropic as the emission becomes optically thick (Kataoka et al., 2015). If it is the case in the HL Tau disk, the large grain population, which is settled down, contributes to little polarized emission in Band 3 whereas the small grain population in the upper layer contributes to polarized emission. To examine the possibility and further constrain grain sizes and their spatial distributions, comprehensive studies combining those observations are needed. This could be the next work.

2.4.3 Validity and Limitations of the Radiative Transfer Modeling

In this study, the grain alignment and self-scattering models are separately constructed to investigate the grain size, shape, and alignment efficiency. The maximum grain radius a_{max} = 130 μm is determined by investigating when the scattered emission contribution becomes comparable to the thermal emission of aligned grains while α and ϵ are fixed. This method possibly causes a certain uncertainty for the measured a_{max} when α and ϵ change. For example, if we assume more elongated grains (larger α) that more randomly orient (small ϵ) to explain the polarized emission in the disk minor axis, the contribution of the scattered emission to reproduce the azimuthally uniform polarized emission can be modified.

However, the deviation from a_{max} = 130 μm is probably small even if this is the case. It is because as shown in Figure 2.11 and 2.12, the scattered emission is highly sensitive to a_{max}. When a_{max} changes with an order of 10 μm, the scattered emission contribution easily increases or decreases and deviates from the observed polarized intensity. Therefore, we here qualitatively conclude that the uncertainty of a_{max} is within an order of 10 μm. To exactly determine all parameters and their uncertainties including α and ϵ as well as a_{max}, the modeling for the other data obtained at λ = 870 μm and 1.3 mm for the disk is promising. This is future work.

We also note a technical difficulty for the dust models. We assume the distinctive grain size distributions for the alignment and self-scattering models: the elongated grains with a_{max} = 50 μm is assumed for the alignment model while the spherical grains with changeable a_{max}, while common grain models are considered to natural assumption. Assuming the common grain population is still difficult because computing the scattering opacity for the elongated grains is challenging. Due to the difficulty, we cannot discuss how our result would be modified when the common grain models are assumed. Although the radiative transfer models assume the nearly spherical grains with α = 1.1, and thus the modification would be small, quantitative estimation of the effect is also future work.

2.5 Conclusions

The origin of the polarized emission at 3.1 mm on the HL Tau disk has been debated in the previous works. To solve the question, we have conducted semi-analytical and radiative transfer modeling. We first confirmed that neither prolate and oblate grain models cannot reproduce the polarization feature on the HL Tau disk (elliptical polarization pattern and azimuthally uniform polarization fraction) as was previously concluded by Yang et al. (2019). We proceeded to further modelings and we found that:

1. We found that the combination of the alignment model assuming prolate grains and self-scattering models can reproduce the polarization features on the HL Tau disk. We also found that the combination of the alignment model assuming the oblate grains and self-scattering models cannot reproduce the polarization feature. The results are surprising because the grain alignment has been believed to triggered by the dust spinning, which is the case in ISM or star-forming clouds.

2. We found that the maximum size of the scattering dust grains is a_{max} $\sim$ 130 μm to reproduce the azimuthally uniform polarization fraction. This size is consistent with them obtained on the polarization observation in Band 6 and 7. However, the size is a few times smaller than that was measured by the spectra (Carrasco-González et al., 2019). The difference of assumed disk model, grain composition, and grain population possibly causes the discrepancy.

3. The Gold alignment model, where the long axes of the dust grains are aligned by the gas flow on grains, is the unique model that predicts the prolate aligned grains. However, this interpretation contradicts several theoretical models. One of the problems is that the directions of gas flow are predicted to be radial for the dust grains with a_{max} = 130 μm, whereas they should be azimuthal to reproduce the azimuthal polarization pattern for the prolate grains. More fundamental problem is that the Gold alignment model is effective only when the gas velocity on the dust grains is supersonic, whereas that is subsonic in disks in general. These pose questions for the alignment theories.

   The constructed semi-analytical and radiative transfer models can be applied to the observations at other wavelengths (870 μm and 1.3 mm). Modeling the multiband polarization observations provide the spectrum of alignment and scattering efficiency, which enable us to further constrain the grain sizes and shapes.

Chapter 3

The observation and analysis for the polarized emission on the AS 209 disk

3.1 Introduction

AS 209 is a Classical T Tauri star in the Ophiuchus star forming region at a distance of 121 $\pm$ 2 pc (Gaia Collaboration et al., 2018). It has a mass of 0.9 $M_\odot$ (Bouvier and Appenzeller, 1992), spectral type of K5 (Luhman and Rieke, 1999) and a luminosity of 1.5 $L_\odot$ (Natta, Testi, and Randich, 2006). The disk mass was estimated to 0.028 $M_\odot$ with SMA continuum observation assuming 100:1 dust-to-gas mass ratio (Andrews et al., 2009). More recently, Favre et al. (2019) conducted CO isotopologue observation with ALMA and derived the gas mass of 3×10^{-3} $M_\odot$, which is less massive compared to the previous study (Andrews et al., 2009). ALMA 1.3 mm dust continuum observations revealed that the disk has two prominent rings at 74 and 120 au and at least three faint rings in the inner 60 au (Fedele et al., 2018; Guzmán et al., 2018). Planet-disk interaction is one promising gap opening mechanism. Recent studies using 3D hydrodynamical simulations found that the ringed structure may be induced by torque from a Saturn-like mass planet at $\sim$100 au (Fedele et al., 2018; Zhang et al., 2018; Favre et al., 2019). The radial profile of the grain size of the AS 209 disk is constrained by measuring spectral index (Pérez et al., 2012; Tazzari et al., 2016). They found that the radial profile of the opacity index β radially increases, suggesting that the grain size radially decreases from $\sim$2 cm to $\sim$0.2 cm.

This paper is organized as follows. In Section 3.2, we briefly summarize observation and data reduction processes. In Section 3.3, we describe characteristics of the observed polarized emission based on the polarization morphology and fraction. In Section 3.4, we explore the origin of the polarized emission and discuss a grain property and dynamics in the AS 209 disk. In Section 3.5, we conclude this paper.

3.2 Observations

The continuum polarization observations at 870 μm were carried out on 2018 May 16 during ALMA Cycle 5 operation. The antenna configurations were

C43-2 with 43 antennas. In total four spectral windows (spws), two for lower sideband, another two for upper sideband, were taken in time division mode (TDM). Those four spws were centered at the central frequencies of 336.5, 338.4, 348.5 and 350 GHz. The effective bandwidth of each spw is 1.875 GHz, providing the bandwidth of ∼7.5 GHz. The bandpass, complex gain, and polarization calibrators were J1751-0939, J1733-1304, and J1924-2914, respectively. The polarization calibrator was observed in four different scans with a scan length of ∼8 minutes at different hour angles to cover a wide range of parallactic angle. The total integration times for the target were 30.89 minutes in the observation.

The reduction and calibration of the data were done with the CASA version 5.1.1 (McMullin et al., 2007). We follow the data reduction process given by Nagai et al. (2016). For the imaging, we perform the interactive CLEAN deconvolution by using the CASA task `tclean`. We employ Briggs weighting with a robust parameter of 0.5. The beam size in the final product is $0.''94 \times 0.''62$ which corresponds to $\sim 114 \times 75$ au at the distance of 121 pc.

With the obtained Stokes Q and U, we derive the polarized intensity (PI). Note that PI has a positive bias because it is always positive value even if the Stokes Q and U have negative values. This bias has a non-negligible effect in low-signal-to-noise observations. We thus derive the debiased polarized intensity with the following equation presented in Vaillancourt (2006) and Hull and Plambeck (2015),

$$PI = \sqrt{Q^2 + U^2 - \sigma_{PI}^2} \tag{3.1}$$

where σ_{PI} is an error of the polarized intensity, which is derived to be $\sigma_{PI} = 2.7 \times 10^{-5}$ Jy beam^{-1} with the error propagation of Stokes Q and U.

Polarization fraction (PF) and polarization angle (θ) are also derived with the following equation.

$$PF = PI/I \tag{3.2}$$

$$\theta = \frac{1}{2} \arctan \frac{U}{Q} \tag{3.3}$$

The 1σ error of the polarization angle σ_θ is calculated in each pixel in the image with a following equation.

$$\sigma_\theta(^\circ) = 0.5 \times 180/\pi \times \sqrt{(U \times \sigma_Q)^2 + (Q \times \sigma_U)^2}/PI^2 \tag{3.4}$$

where σ_Q and σ_U are the rms noise of Stokes Q and U, respectively. In addition, instrumental angle errors can systematically contribute to the uncertainties of the angles. This systematic error ($\Delta\chi$) is $\Delta\chi \sim 2^\circ/\sqrt{N}$, where N is the number of antennas (Nagai et al., 2016) and thus $\Delta\chi \sim 2^\circ/\sqrt{43} = 0.^\circ3$ in this observation. All of these values presented above are derived only where the detection is above the threshold $3\sigma_{PI}$.

3.3 Results

The main results of the observation are summarized in Figure 3.1. Figure 3.1(a) shows the total intensity (Stokes I) of the protoplanetary disk around AS 209 with the color scale and contours. The substructures discovered in the high-resolution observations (Fedele et al., 2018; Guzmán et al., 2018) are not identified in our Stokes I image because the beam size $0.''94 \times 0.''62$ is not small enough to resolve the rings or gaps with the size of $\sim 0.''04$ (Guzmán et al., 2018). The integrated flux density is 489 ± 50 mJy, which is consistent with the previously obtained value, 577 ± 58 mJy within the uncertainty (Andrews et al., 2009).

Figures 1(b) and 1(c) show the polarized intensity and polarization fraction, respectively. The polarization vectors are also overlaid where PI is larger than $3\sigma_{PI} = 81$ μJy beam^{-1}. The vectors are plotted twice per synthesized beam in each direction based on Nyquist sampling. Figure 3.1(d) shows the map of σ_θ in degrees estimated with the equation (4). The typical 1σ polarization angle error is $\sigma_\theta \sim 1-4^\circ$. Note that the systematic angle error ($\Delta\chi = 0.^\circ3$) explained in the former section is not included in Figure 3.1(d).

The polarization orientations show distinct patterns between the inner and outer regions. In the inner $0.''5$ region, which is illustrated by the circle in Figure 3.1(d), the polarization orientations seem to be parallel to the minor axis. In Figure 3.2, we plot a histogram of the deviations of the polarization angles from the minor axis to see if the vectors are completely aligned with the minor axis. We use the major axis position angle (PA) of $85.^\circ76$ and minor axis PA of $-4.^\circ24$ with reference to Guzmán et al. (2018). Due to the large beam size, only four vectors are plotted with the bin width of $\sim 4^\circ$. The plotted angular deviations ($\Delta\theta_{minor}$) are $\Delta\theta_{minor} = 6.^\circ7 \pm 2.^\circ8$, $-5.^\circ1 \pm 2.^\circ5$, $1.^\circ4 \pm 4.^\circ3$, and $7.^\circ7 \pm 3.^\circ6$. Note that the histogram with the small sample size is perhaps not helpful to visualize the angle distribution. However, such analysis will be helpful for future observations with smaller beam sizes, and thus we keep the histogram in this paper.

The center of the histogram seems to be around $\sim 0^\circ$, but three of the $\Delta\theta_{minor}$ values significantly deviate from 0. Given the fact that the sample size is small and each vector is not necessarily independently sampled, we cannot conclude whether the spread is real or not. One possibility is that the spread comes from beam dilution, where polarization in the outer regions can cause some angular deviations from the minor axis. Although an observation with a smaller beam size is necessary to confirm the statement, we conclude that the polarization orientations in the inner region are consistent with the direction of the minor axis.

In the outer $0.''5$ region, on the other hand, the polarization orientations seem to be aligned in the azimuthal directions. To interpret the polarization, we proceed to a further analysis of the polarization angles. First, we discuss whether the observed polarization orientations are consistent with circular or elliptical patterns. The circular pattern is a concentric circle on the image plane, and the elliptical pattern is a trajectory that traces the same orbits in the inclined disk. We derive the tangents of the circle and the ellipse at

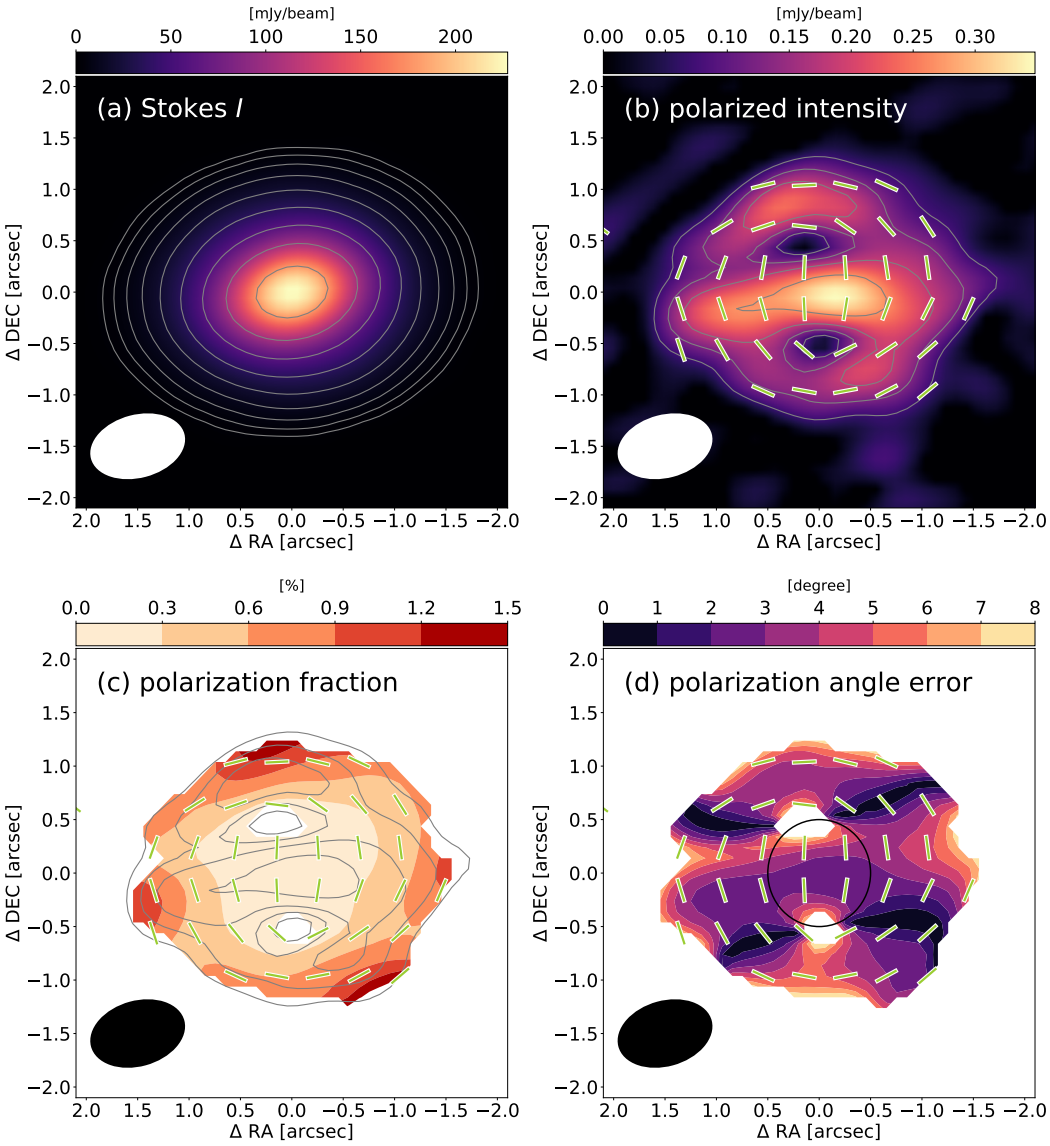

FIGURE 3.1: Upper left (a): The total intensity (Stokes I) of the continuum emission at 870 μm. The solid contours represent total intensity with levels of $100-10000 \times \sigma_I$ (=60 μJy beam^{-1}) in log space. The beam with the size of $0.''94 \times 0.''62$ and position angle of $-75.^\circ3$ is shown in the bottom left with the white ellipse. Upper right (b): Polarized intensity on a linear scale. The solid contour levels are $(3, 5, 7, 10) \times \sigma_{PI}$ (= 27 μJy beam^{-1}). The polarization vectors are presented where polarized intensity is larger than $3\sigma_{PI}$. We set the length of the polarization vectors to be the same. Lower left (c): The polarization fraction overlaid with the vectors. The solid contours show polarized intensity as with the PI map. The polarization fraction where polarized intensity is less than $3\sigma_{PI}$ is removed. The synthesized beam is also presented with the black ellipse. Lower right (d): The color map of the 1σ polarization angle error (σ_θ). The synthesized beam and polarization vectors are also overlaid. The overlaid circle at the center represents the boundary of the inner and outer regions with the radius of $0.''5$.

FIGURE 3.2: The distribution of the polarization angles measured from the minor axis in the inner 0.″5 region. Three bins are presented with the width of ∼4°. The gray dotted line represents the positions of the minor axis PA.

each location of the polarization vectors. For the derivations of the elliptical tangents, we use the same PA of the major axis as the previous discussion and the inclination of 34.°88 (Guzmán et al., 2018). Figures 3(a) and (b) depict comparisons between the observed polarization orientations and the circular (a) or elliptical (b) tangents overlaid on the Stokes I map. Figures 3(c) and (d) show the distribution of the angular deviations from the circular (c) and elliptical (d) tangents, each of which is overlaid with the best-fitted Gaussian function.

The histogram of the angular deviations from the elliptical tangents shows a little narrower width than that from the circular tangents. We confirm this by performing the Gaussian fittings of the histogram, showing that the standard deviations are ∼10° and ∼11° in the elliptical and circular case, respectively. Therefore, the polarization pattern is more consistent with the elliptical pattern rather than the circular pattern. We also conduct a χ^2 test to statistically examine the above discussion and conclude that the elliptical pattern is preferred indeed (see Appendix C).

Then, we investigate if there is a systematic angular difference between the polarization angles and the elliptical tangents. If the polarization vectors are completely aligned with the ellipse, the mean of the angular differences $\Delta\theta_{ellipse}$ would be 0°. However, the histogram of the angular differences shows a certain shift from $\Delta\theta_{ellipse} = 0°$. We calculate a weighted mean of $\Delta\theta_{ellipse}$ with the $\Delta\theta_{ellipse}$ and σ_θ maps (see Appendix C). This results in the weighted mean of $\Delta\theta_{ellipse} = -4.°5 \pm 1.°6$, which is significantly shifted from 0°. This suggests that the polarization orientations have certain angular deviations from the elliptical tangents with almost the same degrees and directions. Note that a beam dilution due to the large and flattened beam

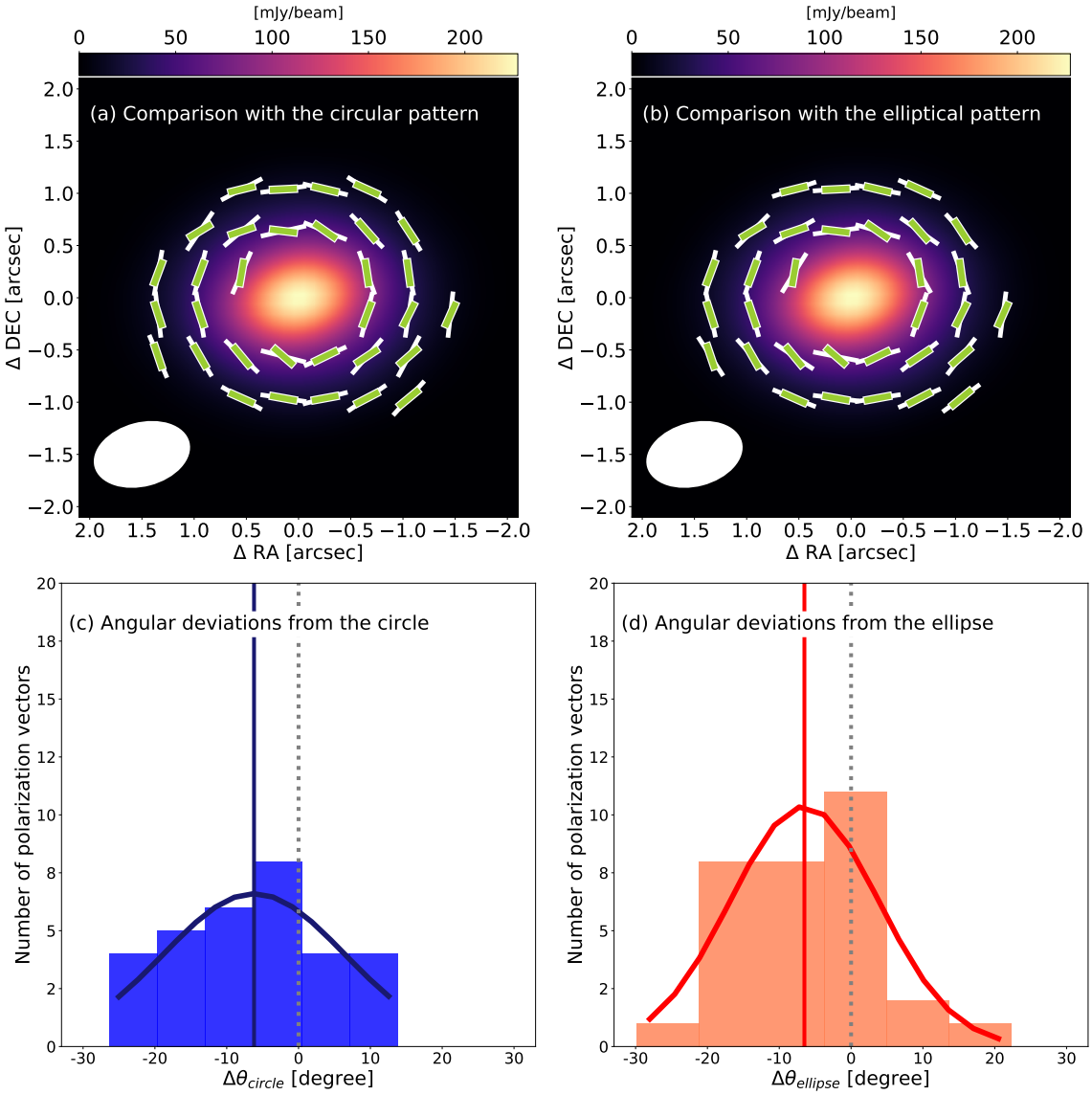

FIGURE 3.3: (a) Comparison between the polarization vectors and circular tangents in the outer 0.″5 region. The green and white lines represent the polarization vectors and circular tangents, respectively. (b) Comparison between the polarization vectors and elliptical tangents. The green and white lines are represented as with (a). (c) The histogram of the angular differences between the polarization vectors and the circular tangents, both of which are presented in (a). The best-fitted Gaussian is overlaid to the histogram. The blue straight line represents the center of the distribution. The gray dotted line represents the $\Delta\theta_{circle} = 0^\circ$ position. (d) The histogram of the angular differences between the polarization vectors and the ellipse, both of which are presented (b). The best-fitted Gaussian and the center of the distribution are overlaid as with (c) with red lines. $\Delta\theta_{ellipse} = 0^\circ$ position is also presented as with (c).

can artificially generate the angular deviation from the azimuthal directions.

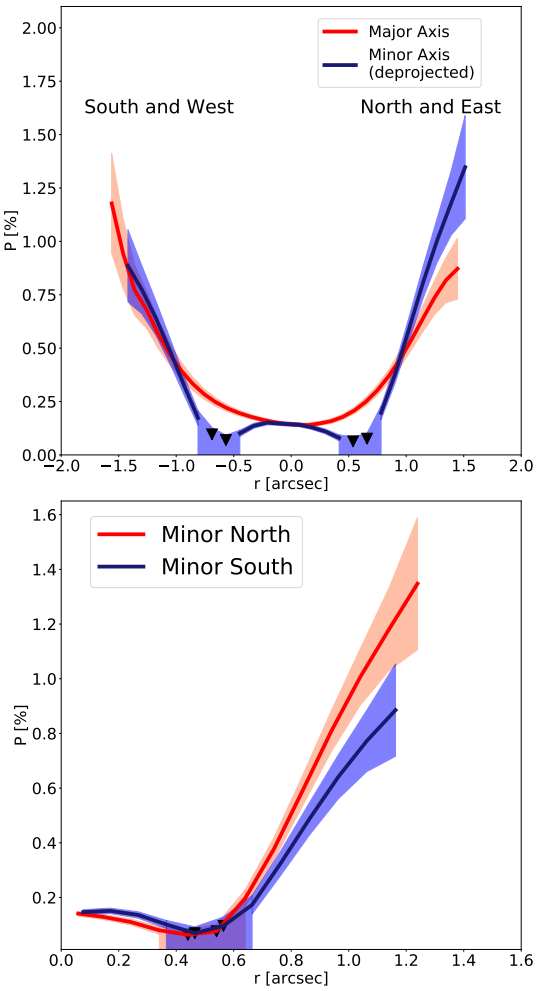

FIGURE 3.4: Upper panel: radial profiles of the polarization fraction along with the major (red) and minor (blue) axes. To correct the disk inclination ($i = 34.^{\circ}88$), the minor axis profile is enlarged by multiplying the radius by $1/\cos i$ for the deprojection. The shade in each profile represents the 1σ error regions of the polarization fraction. The upper limits and shade are also presented in the region where the polarized intensity is less than $3\sigma_{PI}$. Bottom panel: minor axis profiles of the polarization fraction in the north (red) and south (blue), both of which are extracted from the upper panel. The deprojection is not applied to the profiles.

Although we need detailed modeling to examine the effect, the obtained orientations which systematically deviate from the azimuth cannot be caused only by the beam dilution.

The polarization fractions are another clue to interpreting the polarization. To compare the polarization fractions between the major and minor axes, we plot radial profiles of the polarization fractions along the major and deprojected minor axes in Figure 3.4 (upper panel). The negative values in the horizontal axis represent the south and west regions, while the positive values represent the north and east regions.

As Figures 1(c) and Figure 3.4 show, polarization fractions are not the same between the two regions as well as the polarization orientations. In the inner 0.″5 region, the polarization fractions are almost uniform at ∼0.20%. Note that the rms noise of the polarization fraction is ∼0.01% and thus the 0.20% polarization fraction is significant. In the outer 0.″5 region, on the other hand, the polarization fractions gradually increase from ∼0.2% to ∼1.0% with increasing radius. The gradual increase is likely due to the beam dilution between the inner and outer region, each of which shows distinct polarization orientations and thus cancel out each other. This can reduce the polarization fractions near the 0.″5 regions where the distinct polarization orientations coexist in the inner and outer regions. The effect becomes weaker with increasing the distance from the center. Thus, the typical polarization fraction in the outer region is likely ∼1.0%, which is obtained in the outermost region.

Another feature in the polarization fractions is that the radial profile along the minor axis shows a certain asymmetry that polarization fractions increase more sharply in the north region. The bottom panel of Figure 3.4 shows the minor axis profiles extracted from the upper panel. Indeed, the polarization fractions in the north region reach higher values of ∼1.2%. The asymmetry is probably not caused by the beam dilution since its effect should be the same between the north and south regions. However, the difference of the profiles is only 1σ, and moreover, the detection of the polarized intensity is somewhat marginal with the signal-to-noise ratio of $\sim 3-5\sigma_{PI}$. Therefore, although the asymmetry may reflect some physical origins, we cannot robustly conclude if it is real with this data.

3.4 Discussion

We detect the ∼0.20% and ∼1.0% polarization in the inner and outer regions, respectively. The polarization orientations are parallel to the minor axis in the inner region, while they are in the azimuthal (elliptical) directions in the outer region. These distinct characteristics of the polarized emission imply the distinct origins of the polarized emission between the regions. First, we describe the possible origins of the polarization and predicted polarization pattern in subsection 4.1. Then, we explore the origins in the AS 209 disk and possible models for the grain properties and grain dynamics in the AS 209 disk in the inner and outer regions in subsection 4.2. and 4.3.

3.4.1 The Polarization Pattern in the Different Theories

The possible origins of the millimeter-wave polarization from protoplanetary disks are the grain alignment or self-scattering. The grain alignment models include magnetic, radiative and mechanical alignment, where dust grains are aligned with the magnetic fields, radiative gradient and gas flow, respectively. We quickly review the currently proposed scenarios of the millimeter-wave polarization and summarize the phenomenological differences.

TABLE 3.1: The origin and expected polarization morphology (inclined disks)

Origin	**Morphology**
magnetic alignment	radial (if toroidal)
radiative alignment	circular
mechanical alignment (Gold mechanism)	elliptical
mechanical alignment (helicity-induced, small grain)	circular (if $\delta v_r \gg \delta v_\phi$)
mechanical alignment (helicity-induced, large grain)	spiral-like (if $\delta v_r \sim \delta v_\phi$)
self-scattering	minor axis

Long axes of the magnetically aligned dust grains are perpendicular to magnetic fields (Davis and Greenstein, 1951; Cho and Lazarian, 2007). The toroidal magnetic fields are thought to be amplified with magnetorotational instability (MRI) in disks (Brandenburg et al., 1995; Fromang and Nelson, 2006; Bai and Stone, 2013; Suzuki and Inutsuka, 2014). Thus, the resultant polarization would show a radial pattern in face-on disks (Brandenburg et al., 1995).

Grain alignment with radiation fields makes grain long axes perpendicular to radiation gradients (Cho and Lazarian, 2007; Tazaki, Lazarian, and Nomura, 2017). Thus, the outgoing radiation gradients would produce a circular pattern in polarization vectors in face-on disks. We note that Yang et al. (2019) pointed out that the polarization orientations remain circular patterns even in inclined disks.

Grain alignment with the ambient gas flows, which is called mechanical alignment, makes grain long axes to be either parallel or perpendicular to the gas velocity against the dust grains. The alignment parallel to the gas occurs for subsonic gas flows, which is called the Gold mechanism (Gold, 1952). The aligned dust grains would produce an elliptical polarization pattern in inclined disks (Yang et al., 2019). Dust grains can also be aligned perpendicular to the gas flow onto the dust grains when they have certain helicity (Lazarian and Hoang, 2007). The resultant polarization is perpendicular to the gas velocity against the dust grains. This helicity-induced grain alignment occurs for subsonic gas. Since gas velocity against dust grains is subsonic, helicity-induced alignment likely occurs in protoplanetary disks (Kataoka, Okuzumi, and Tazaki, 2019).

The polarization orientations for mechanical alignment are determined by gas velocity against dust grains. We express the radial and azimuthal components of the gas velocity against the dust grains with δv_r and δv_ϕ, respectively. The gas velocity against the dust grains is also determined by how well the dust grains are coupled to gas, which is denoted with the Stokes number (St). The Stokes number is the dust stopping time normalized with the Keplerian timescale and is given by $\mathrm{St} = \frac{\pi}{2}\frac{a\rho_s}{\Sigma_g}$, where a is the grain size, ρ_s is the internal density of the dust grains and Σ_g is the gas surface density (Birnstiel, Dullemond, and Brauer, 2009). We briefly describe the expected polarization patterns for the helicity-alignment model in Kataoka, Okuzumi,

and Tazaki (2019), assuming that the dust grains radially drift due to the headwind from the gas.

When the Stokes number is much smaller than unity, which corresponds to small grain size, the headwind of the gas on the dust grain is dominated by the radial component ($\delta v_r \gg \delta v_\phi$). The polarization orientations are perpendicular to the gas velocity against the dust grains, and thus the resultant polarization pattern is circular. When the Stokes number is close to unity, the larger dust grains are decoupled from the gas and radially drift due to the gas headwind, resulting in the comparable velocity fields against the dust grains between the radial and azimuthal components ($\delta v_\phi \lesssim \delta v_r$). As a consequence, the synthetic relative velocity is inclined with respect to the azimuthal directions, and thus the polarization orientations show a spiral-like pattern. The deviation from the circular direction at each location on the sky would be $\arctan(\delta v_r / \delta v_\phi)$ (Kataoka, Okuzumi, and Tazaki, 2019).

The polarization orientations for the scattering-induced polarization are determined by incoming flux distributions around the dust grains (Kataoka et al., 2015). In the inclined disk such as the AS 209 disk, the polarization orientations are parallel to the minor axis because the flux coming parallel to the major axis is generally stronger than that parallel to the minor axis (Pohl et al., 2016; Kataoka et al., 2017). Yang et al. (2017) pointed out that the polarization patterns can be modified by the spatial distributions of the optical depth. When the disk is optically thin in the outer region, the polarization orientations are perpendicular to the radiative gradient in the disks. The outgoing radiative gradient leads to the azimuthal pattern in the outer region. However, the model assumed smooth surface density structures, which has no rings and gap. In the case of the AS 209 disk, the radiative gradient of the flux distribution produced by the ringed structure would be too small to produce the azimuthal pattern. Thus, if the scattering dominates the observed polarized emission, the polarization orientations are parallel to the minor axis even if the disk is optically thin in the outer region.

In Table 1, we summarize the expected polarization patterns explained above. In the following subsections, based primarily on the polarization patterns shown in Table 1, we explore the origin of the polarization separately in the inner and outer regions.

3.4.2 The Origin of the Polarization in the Inner Region

In the inner region, the polarization vectors are aligned with the minor axis (Figure 3.2). Although certain deviations from the minor axis exist, the observed orientations which are parallel to the minor axis are consistent with the self-scattering model in the inclined disks (Table 1). Therefore, we conclude that self-scattering dominates the polarized emission in the inner region of the AS 209 disk at 0.87 mm.

The polarization fraction in the inner region is $\sim$0.2 % (Figure 3.1(a) and 4). The self-scattering model predicts the polarization fraction of $2-3\%$, when the grain population has a single power-law with the maximum grain size of $a_{max} \sim \lambda/2\pi \sim 140$ μm (Kataoka et al., 2015; Kataoka et al., 2016a).

Polarization fractions obtained in the previous observations for the inclined disks were lower than 2−3%, but significantly higher than that in this observation. For example, the IM Lup and HL Tau disks show scattering-induced polarization with the fractions of ∼1.2% and ∼0.6% in the central regions (Hull et al., 2018; Stephens et al., 2017). Relatively low polarization fraction in the AS 209 disk can be explained by two possibilities in the grain size populations. One is that the grain population has a single power-law with a maximum grain size of a_{max}, which is a few times larger or smaller than ∼140 μm (Kataoka et al., 2016a). If this grain model is correct, a_{max} is roughly estimated to be ∼50 μm or ∼400 μm. The other possibility is that two size population model where $a_{max} \sim 140$ μm in one population but a_{max} in the other population is significantly smaller or larger than 140 μm. This additional grain population contributes to unpolarized Stokes I emission but not to polarized emission, and thus reduces polarization fractions.

The maximum grain size has been constrained by Pérez et al. (2012) and Tazzari et al. (2016) with the analysis of the spectral index. They found that the spectral index radially increase with the range $\beta = 0.5-1$, and yielded the grain size of $a_{max} \sim 0.5-2$ cm in inner 60 au. These grain sizes are much larger than those from the polarization.

The size discrepancy may come from the contamination of the optically thick emission in low-resolution observations. Although measurements of the grain size assume the thermal emission is totally optically thin at millimeter wavelengths, Tripathi et al. (2017) pointed out that the assumption is not necessarily correct based on a large sample of low-resolution disk images. However, Pérez et al. (2012) and Tazzari et al. (2016) revealed that the millimeter continuum emission from the AS 209 disk is optically thin at all radii, suggesting that the discrepancy of the grain sizes are not due to the optically thick emission.

The assumption on the grain composition also strongly affects the spectral indices values, leading to grain size uncertainties. For example, Testi et al. (2014) showed that compact grains which composed of silicate, carbonaceous and water ice take $a_{max} \sim 0.5-5$ cm in $\beta = 0.5-1$ range while compact grains which composed only of silicate and carbonaceous material take a_{max} $\sim 0.5-5$ mm in the same $\beta = 0.5-1$ range (see Figure 3.4 of Testi et al. (2014)). The one size population model with $a_{max} = 500$ μm and the latter grain composition model described above is one of the solutions to reconcile the two studies.

More recent studies pointed out that the observed low spectral indices can be reproduced when the effect of scattering is included (Liu, 2019; Zhu et al., 2019). This means that measurement of the grain size ignoring the opacity of scattering can lead to overestimation of the grain size. Thus, including the effects of scattering into continuum modeling is needed to reconcile the discrepancy of the grain properties between the grain size measurements.

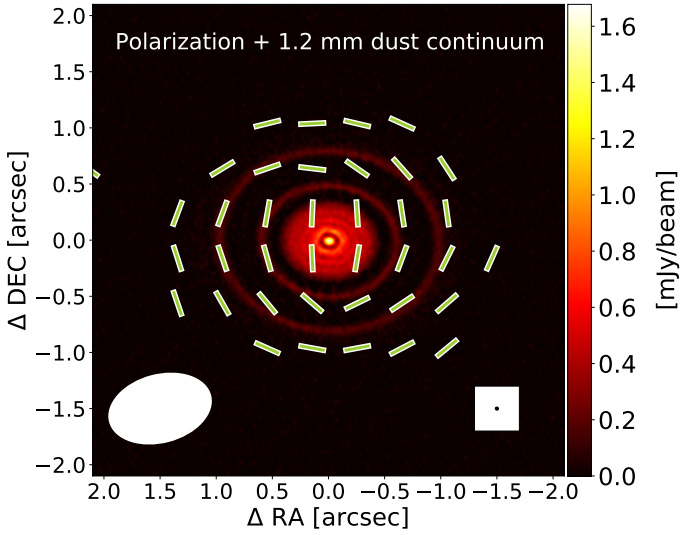

FIGURE 3.5: The polarization vectors and the high resolution image obtained in the DSHARP program (Guzmán et al., 2018). The synthesized beam size in our and DSHARP observations are presented in the lower left and lower right, respectively.

3.4.3 The Origin of the Polarization in the Outer Region

In the outer $0.''5$ region, the polarization orientations seem to be in the azimuthal directions. By conducting the detailed analysis on the orientations, we find that the orientations are consistent with the elliptical pattern rather than the circular pattern and moreover the vectors have the systematic angular deviations from the elliptical tangents with the mean value of $\Delta\theta_{ellipse} = -4.^{\circ}5 \pm 1.^{\circ}6$. The spiral-like pattern can be produced only with the mechanical alignment model (Table 1). Therefore, the observed polarization likely originates from the dust grains which are aligned by the gas flow against the dust grains.

To interpret the polarization, we explore where the polarized emission comes from. However, the large beam size prevents us from exploring the emitting regions only with the polarization data. Thus, in Figure 3.5, we compare the polarization vectors with the previous higher resolution observation by Guzmán et al. (2018). Although it is difficult to link the positions of the vectors to that of high resolution image due to the large beam size gap, roughly speaking, the polarization in the outermost region at $\sim 1.''0$ likely comes from the outermost ring at 120 au in the higher resolution image. Thus, the emitter of the polarization is likely the dust grains at the 120 au ring.

Since the polarization pattern is presumably related to the grain dynamics in the disk, we consider possible grain dynamics to reproduce the spiral-like pattern. Kataoka, Okuzumi, and Tazaki (2019) has already considered the relationships between the grain dynamics and polarization patterns. However, we cannot directly apply the model to the observed pattern because the assumed disk in the model has a smooth surface density profile which is quite different from that of the AS 209 disk. Therefore, we qualitatively discuss the

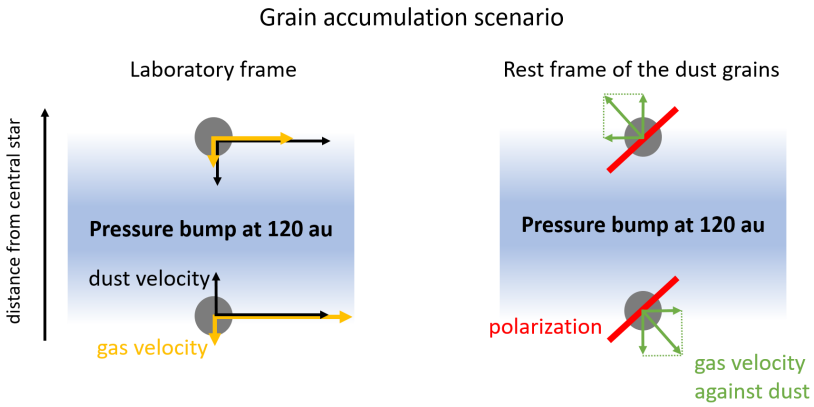

FIGURE 3.6: Schematic illustration of the grain accumulation scenario which can reproduce the inclined polarization orientations. The blue region represents the gas pressure bump near the 120 au ring. The left picture shows grain (black) and gas (orange) velocity fields in the laboratory frame. The right picture shows the radial, azimuthal and synthetic gas velocity against dust grains with green arrows. The resultant polarization vectors are also presented with the red lines.

polarization pattern when mechanical alignment occurs at the ring.

Figure 3.6 illustrates a possible scenario, where the dust grains radially drift inside and outside of the local pressure maxima. To find the resultant polarization pattern at the pressure maxima, we discuss the velocity vectors of gas and dust grains. In a laboratory frame, the gas rotates with sub-Keplerian outside the bump due to the negative pressure gradient while it rotates with super-Keplerian inside the bump due to the positive pressure gradient. Instead, the dust grains rotate almost with the Keplerian speed. As a result, the dust grains on both sides of the bump drift to the pressure maximum. Now, we see the velocity fields on the rest frame of the dust grains. The radial and azimuthal components of the relative gas velocity, δv_r and δv_ϕ become comparable. Because the polarization vectors are perpendicular to the direction of the gas velocity on the rest frame of the dust grains in the helicity-induced alignment model, this leads to the spiral-like polarization patterns.

If the Stokes number is smaller than unity, dust grains would satisfy $\delta v_r > \delta v_\phi$. This leads the polarization pattern almost in the azimuthal direction, but slightly deviates to the clockwise or counterclockwise directions depending on the rotation direction: if the disk rotates in the counter-clockwise direction, the polarization vectors slightly deviate in the clockwise direction (see Kataoka, Okuzumi, and Tazaki (2019)). The direction of the disk rotation has been revealed to be clockwise with previous CO isotopologue observations (Andrews et al., 2009; Guzmán et al., 2018; Favre et al., 2019). Therefore, the expected direction of the deviation is in the counterclockwise direction, or the plus sign in the histogram as shown in Figure 3.3 while the figure shows the opposite results (see the discussion below).

This scenario that produces the spiral-like pattern is partly supported by the previous CO isotopologue observation, where local enhancement of the gas surface density was discovered near the outermost dust ring (Favre et al., 2019). This suggests the presence of the local gas pressure maximum which coincident with the dust ring, implying that we see the drifting grains in the pressure bump with the polarization.

We here note that the grain diffusion from the ring also reproduces the same polarization pattern as the accumulation model. We do not discuss the diffusion but accumulation because it is more likely to occur at a ring.

The common scenario to make the gas pressure maxima are, for example, a planet (Kanagawa et al., 2015; Kanagawa et al., 2016; Bae, Zhu, and Hartmann, 2017; Dong et al., 2017; Huang et al., 2018b; Fedele et al., 2018; Favre et al., 2019) and some MHD effects (Johansen, Youdin, and Klahr, 2009; Bai and Stone, 2014; Simon and Armitage, 2014). We note that the grain accumulation can also be triggered by secular gravitational instability (Tominaga, Inutsuka, and Takahashi, 2018). This model predicts that the gas also be accumulated and thus the gas velocity on the dust grains is slightly different from the models above. While we do not discuss the detailed comparison, the presented polarization may distinguish these physics by revealing the relative velocity between gas and dust grains.

The ratio of the radial and azimuthal components of gas velocity against the dust grains can be derived by assuming the models as $\delta v_\phi / \delta v_r = \tan(\Delta\theta_{ellipse})$ $= 0.08 \pm 0.03$. Both of the models predict the same directions of the angular deviations, which are determined by which clockwise or counterclockwise the disk rotates. When the disk rotates clockwise, as shown in Figure 3.6 shows, the orientations are inclined to the west directions, which correspond to positive angular deviations.

However, there are several questions for the interpretation. One is that the observed pattern is more consistent with the elliptical pattern, which is inconsistent with the theoretical expectations of the helicity-induced alignment model (Kataoka, Okuzumi, and Tazaki, 2019). Moreover, both of the models predict the positive angular deviations whereas the observed orientations show negative angular deviations (i.e. the theory predicts 90° flipped orientations against the observed orientations). Thus, the directions of the orientations cannot be reproduced with the combination of the helicity-induced alignment model and the grain accumulation model as long as the disk rotates clockwise.

Since we find that the helicity-induced alignment model does not perfectly explain the observations, we also consider another mechanical alignment, the Gold mechanism although it probably does not occur in disks since gas velocity against dust grain is subsonic. As explained above, the polarization orientations are parallel to the gas flow against the dust grains for the Gold mechanism, leading to the elliptical polarization pattern (Yang et al., 2019). This expectation is consistent with the fact that the observed pattern is more consistent with the elliptical pattern. The Stokes number should be much larger than unity ($\mathrm{St} \gtrsim 10$) so that δv_ϕ is much larger than δv_r and the azimuthal pattern arises. If it is the case in the disk, the polarization

orientations are inclined with the same directions of the observed polarization. However, another question is that the thermal emission from the dust grains with such large Stokes number is not efficient because the emissivity of the dust grains is inversely proportional to the grain size. Therefore, even though the Gold mechanism is considered, it is uncertain whether the observed orientations can be explained by the possible grain dynamics.

We summarize that the observed spiral-like pattern can be reproduced only with the mechanical alignment model. However, both Gold mechanisms and helicity-induced alignment models have some difficulties, which prevent us from naturally interpreting the orientations by assuming the grain dynamics. This poses the possibility that we misunderstand somewhere in the alignment processes and/or grain dynamics in the protoplanetary disks.

We also discuss the observed polarization fraction. We detect $\sim$1.0% polarization fractions in the outermost regions. Moreover, we also find the asymmetry that the polarization fraction in the north region, which is farther to us reaches the larger value with 1σ (Figure 3.4). No theoretical expectations for the polarization fractions for the mechanical alignment model have been established so far, and thus it is unclear what determines the values and spatial distributions of the polarization fractions. The near/far side asymmetry is thought to be observed in the self-scattering and optically thick disks. Yang et al. (2017) predicted a spatial shift of the polarized intensity peak and near/far side asymmetry of the polarization fractions, both of which are caused by geometrical effects such as disk flaring. However, the AS 209 disk was revealed not to be optically thick at 870 μm (Pérez et al., 2012; Tazzari et al., 2016), casting a question for applying the model to the disk. In fact, the center shift, which was predicted by Yang et al. (2017), is not observed in the inner region of the AS 209 disk, where the scattering-induced polarization is observed. Therefore, the optical depth effects are unlikely to reproduce the observed profile and the origin of the profile is uncertain. This will be investigated in future works.

3.5 Conclusions

We have presented 870 μm polarization observation toward the Class II protoplanetary disk around AS 209. Our main findings can be summarized as follows:

1. We found the spatial segregation of the polarization patterns and fractions between inner and outer regions. We detected $\sim$0.2% polarization in the inner $0.''5$ regions. The polarization orientations in the region are parallel to the minor axis. In the outer region, we detected $\sim$1.0% polarization and found that the polarization orientations are consistent with the elliptical pattern but with the angular deviation of $\Delta\theta_{ellipse} \sim 4.^{\circ}5 \pm 1.^{\circ}6$.

2. The polarization pattern in the inner region is consistent with the self-scattering model. The low polarization fraction ($\sim$0.2%) compared to

the expected value when the dust grains population has a single power-law with $a_{max} \sim \lambda/2\pi \sim 140$ μm can be explained by the following grain models. One is that the grains population has a single power-law with a_{max}, which is a few times larger or smaller than 140 μm. The other is that there is another grain population, which contributes to unpolarized emission but not to the polarized emission.

3. The spiral-like pattern in the outer region can be produced only with the mechanical alignment model. This polarized emission likely comes from the outermost ring at 120 au. This suggests that the dust grains at the ring accumulate to the pressure maximum near 120 au.

4. We found that the combination of mechanical alignment and grain accumulation model can reproduce the spiral-like pattern, but there are some inconsistencies. The helicity-induced model predicts (1) circular polarization pattern and (2) positive angular deviations from the azimuthal directions, both of which are inconsistent with the observed pattern. The Gold mechanism can reproduce both of the elliptical pattern and the observed deviations from the azimuthal directions, but only in the case that the Stokes number is large, where the grain emissivity is inefficient in the millimeter-wave.

5. No theoretical expectations for the polarization fraction for the mechanical alignment disks. Thus, it is yet clear whether the obtained values and spatial distribution of the polarization fractions are typical or not for mechanical alignment disk. This will be investigated in future works.

For the detailed analysis of the polarization angles presented in this work, the large beam size effects are not negligible. Observations with higher spatial resolution would help to confirm the presence of the spiral-like pattern and understand the origin.

Chapter 4

Summary, Discussion, and Outlook

In this chapter, we summarize what we have newly conducted, new findings and future prospects.

4.1 New Analysis and Findings in the Two Studies

Since the first detection of the polarized emission of protoplanetary disks by Stephens et al. (2014), the millimeter-wave polarization observations have turned out to be the strong tool to directly measure the grain sizes. However, the multiple contributors to the emission are proposed and their relative importance is poorly understood by the theoretical studies. To precisely interpret the polarized emission and to connect the observed features with the grain growth scenarios, it is essential to phenomenologically address the origins with the careful analysis for the polarization features. Nevertheless, there have been few studies that carefully disentangle the origins and determine the dominant processes.

This study conducted the detailed analysis and modeling toward the polarized emission on the AS 209 and HL Tau disks, whose origins have been largely uncertain so far. In considering the origins, we newly include the effect of gas-flow alignment (Gold and helicity-induced) models, which have not been considered as candidate models so far. In the following, we explain what is new in this study.

In Chapter 2, we constructed the semi-analytical and radiative transfer models of the grain alignment and self-scattering to interpret the 3.1 mm polarization of the HL Tau disk. Especially, this is the first study that develops the radiative transfer models of the grain alignment. The analysis revealed that the HL Tau polarization can be reproduced by the combination of the self-scattering and grain alignment models and the maximum grain size reach a_{max} = 130 μm. Furthermore, we also revealed that the prolate grain model is preferred rather than the oblate grain model.

In Chapter 3, new observation and data reduction for 870 μm polarization of the AS 209 disk were conducted. In interpreting the polarization, we proposed the new analysis to investigate the presence of systematic angular deviation from the circular or elliptical pattern and we significantly detected the deviation. The angular deviation is consistent with the model, where the radially drifting dust grains are aligned by the gas flow on the dust grains

at 120 au. Moreover, the directions of the angular deviations are consistent with the alignment model with prolate grains, not oblate grains.

Through both the studies, for the first time, we revealed that both the grain alignment and self-scattering simultaneously contribute to the (sub)millimeter-wave polarization in disks. Furthermore, we also found that the aligned grains are prolate but not oblate, although this contradicts some theoretical predictions as explained in Section 2.4 and 3.4.

4.2 Common View on the Two Disks

We describe implications on the grain sizes and the alignment processes in the HL Tau and AS 209 disks. We detect the polarized emission that probably comes from thermal emission of aligned grains for both of the disks although some questions remain for the origin. A major difference between the observations is the wavelengths in which the thermal emission by the aligned grains dominates. The grain alignment works in the AS 209 at $\lambda \sim 870$ μm on the AS 209 disk. On the other hand, on the HL Tau disk, emission by the aligned grains dominates at longer wavelength $\lambda \sim 3.1$ mm while the scattering-induced polarization dominates in the shorter wavelengths at $\lambda \sim 870$ μm and 1.3 mm.

This indicates that the sizes of the aligned grains are different between the two disks. Kirchschlager, Bertrang, and Flock (2019) have calculated the absorption opacity for the major/minor axes of the elongated grains to predict the polarization fraction as a function of grain sizes, axis ratio, and porosity. One of the findings in their work is that when the grain sizes are much larger than the observation wavelengths, net polarization fraction becomes negligible. It is because that the emission with the short wavelengths is equally absorbed by the grain major/minor axes, resulting in zero net polarization fraction. They estimated the grain size range in which the polarization by aligned grains to $a_{max} < 8\lambda$ for silicate grains.

With these results, we obtain some implications on the grain sizes in both of the disks. Because the thermal emission of the aligned grains is observed at $\lambda = 870$ μm on the AS 209 disk, the upper limit of the grain sizes is roughly estimated to $a_{max} \lesssim 100$ μm. On the other hand, the emission is observed at $\lambda = 3.1$ mm whereas the little alignment signatures are observed at the shorter wavelengths, indicating that the lower and upper bound of the grain sizes are roughly 100 μm $\lesssim a_{max} \lesssim 300$ μm. Therefore, we find that the grain sizes in the HL Tau disk are larger than those in the AS 209. We also find that the grain size constrained by the alignment signatures are roughly consistent with that constrained by the scattering model. We here emphasize that the discussions are somewhat qualitative. Since the polarization fractions are strongly influenced by the beam dilution, constraining the sizes or axis ratio of the aligned grains needs higher resolution observations especially for the AS 209 disk. Detailed modeling as is done in this study for higher quality images would sophisticate the above discussions.

Another common result is that the model of the aligned grains prefer to prolate model rather than the oblate model, suggesting that the dust grains

do not spin about any external sources. This picture is obviously different from that in the ISMs and star-forming clouds, where the dust grains are aligned by magnetic fields, which is triggered by the dust spinning. Our results indicate that the tendency of the dust spinning, which is called "helicity", disappear through the grain growth processes and that the different alignment mechanisms drive among the regions with the different spatial scales.

The theoretical models that predict the prolate aligned grains are only gas-flow alignment proposed by Gold (1952). However, this scenario provokes several inconsistencies regarding the grain size, dynamics, and alignment processes as explained in Sections 2.4 and 3.4. Therefore, no alignment models cannot reproduce our obtained results without the explained inconsistencies, posing questions of our understandings of the grain alignment and/or dynamics.

As well as the two objects, for example, DG Tau, Haro 6-13 (Harrison et al., 2019), show the azimuthal polarization morphology and comparable polarization fraction between the disk minor and major axes at 3.1 mm. As a natural extension of our findings, these features can be also reproduced with the grain alignment with the prolate grains and the self-scattering models. This indicates that the prolate aligned grains are typical in the other disks. This study provides the first step toward such comprehensive studies. As a summary, new findings for each object are illustrated in Figures 4.1 and 4.2.

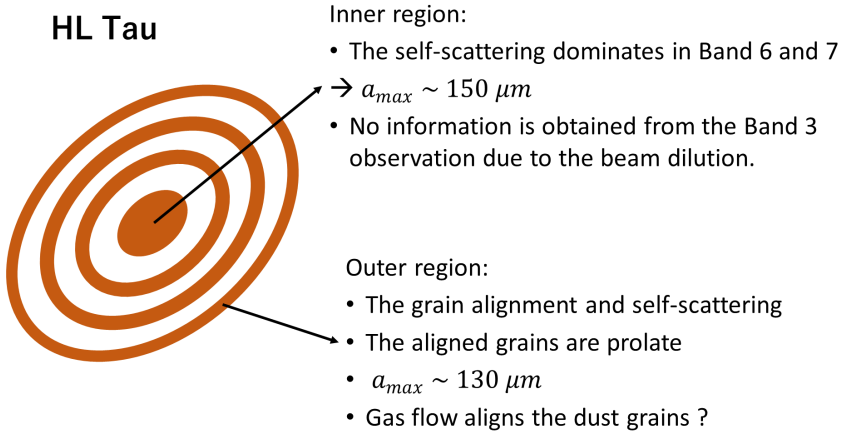

FIGURE 4.1: Summary of the interpretation of the polarized emission for the HL Tau disk.

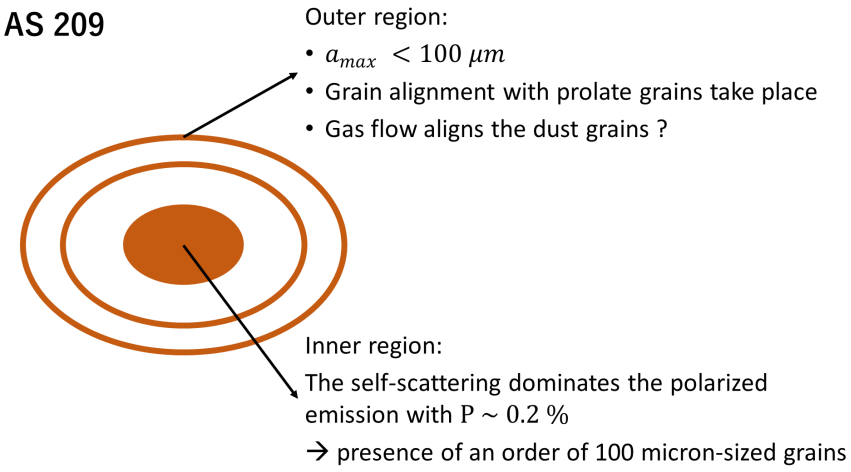

FIGURE 4.2: Summary of the interpretation of the polarized emission for the AS 209 disk.

4.3 The Implications on the Grain Growth Scenarios

Theoretically, as explained in Chapter 1, the coagulation process of the dust grains is poorly understood. To improve the theoretical models, the observational constraints on the grain sizes and shapes are essential. The millimeter-wave polarization observations including our studies have revealed that the maximum grain sizes are on the order of ∼100 μm in the disks, where the scattering-induced polarization was detected (e.g. Bacciotti et al., 2018; Cox et al., 2018; Girart et al., 2018; Harris et al., 2018; Hull et al., 2018; Lee et al., 2018; Ohashi et al., 2018; Sadavoy et al., 2018a; Sadavoy et al., 2018b; Dent et al., 2019; Harrison et al., 2019; Ohashi and Kataoka, 2019). The fact that 100 micron-sized grains are prevalent in the many disks appears curious in terms of the theories. It is because that many growth models predict that dust grains easily evolve into centimeter size in the outer disks, where the water ice grains efficiently stick to each other (Brauer, Dullemond, and Henning, 2008; Birnstiel, Dullemond, and Brauer, 2010; Okuzumi et al., 2012). This indicates that some mechanisms that prevent the steady growth need to be invoked. For example, the latest theoretical study showed that the presence of grains with CO_2 ice mantles can lead to fragmentation because the CO_2 ice is poorly sticky (Okuzumi and Tazaki, 2019).

The fact that $a_{max} \sim 100$ μm is prevalent also suggests that the reachable dust size induced by collisional grain growth is limited to the size. To further growth that eventually forms planetesimal and planets take place, other mechanisms need to be invoked. As explained in Section 1.2, accumulation of the dust grains via Streaming Instability (Youdin and Goodman, 2005), Secular Gravitational instability (Takahashi and Inutsuka, 2014; Tominaga, Inutsuka, and Takahashi, 2018), and other processes are proposed as promising mechanisms. That can lead to form unstable dust clump, leading to form larger body or planets.

One more result obtained on the polarization observations is that the elongated dust grains are also prevalent, which is indicated by the grain alignment signatures (Girart et al., 2018; Harris et al., 2018; Lee et al., 2018; Sadavoy et al., 2018a; Sadavoy et al., 2018b; Harrison et al., 2019). Previous grain growth models have not considered the evolution processes of such aspherical grains. How the presence of the aspherical grains modify the conventional growth scenario is unclear and would need to be conducted as future work. For theoretical works, observational constraints on the grain axis ratio, alignment efficiency, and size are essential. Although there is the degeneracy between the axis ratio and alignment efficiency in this study, the analysis for the polarized emission from the aligned grains, our analysis would be a potential tool to constrain parameters.

4.4 Future Prospects

New analysis and modeling for the millimeter-wave polarization developed in our studies can be applied to that of the other disks. Comprehensive analysis and modeling for other objects that show the azimuthal polarization pattern, which is, for example, DG Tau and Haro 6-13 (Harrison et al., 2019), can provide us clues to investigate the grain properties and alignment processes, which are beyond our new findings. As well as the class I/II objects, the polarized emission has been for a number of class 0/I objects (e.g. Alves et al., 2018; Cox et al., 2018; Girart et al., 2018; Sadavoy et al., 2018a; Sadavoy et al., 2018b). Investigating the polarization origins for the polarization enables us to investigate the grain growth processes in the earlier evolution phases.

Observations at different wavelengths are also crucial to further constrain the grain sizes. The ALMA polarization observations can probe the grains with the sizes of a few hundreds of microns in Band 3, 6 and 7; however, to constrain the population of larger or smaller grains, observations at shorter or longer wavelengths need to be involved. For example, mid-infrared polarization imaging using CanariCam found the centrosymmetric polarization pattern on the AB Aur disk (Li et al., 2016). Centimeter polarization observations using ngVLA will enable us to probe the larger grains and to resolve the size discrepancy between the spectra and polarized emission.

Appendix A

Appendix A

We describe how to construct the semi-analytical models of the grain alignment and self-scattering in detail whose brief explanations are described in Section 2.2.

A.0.1 Coordinate systems and disk model

We first introduce a coordinate system to put a disk model, which is commonly used for computing the grain alignment and scattering models. We define a coordinate system as shown in Figure A.1. Given a Cartesian frame xyz, we define a disk plane in the xy-plane, which is defined with unit vectors $\vec{x} = (1, 0, 0)$ and $\vec{y} = (0, 1, 0)$. Thus, the z-axis $\vec{z} = (0, 0, 1)$ points perpendicular to the disk plane. Since the HL Tau is inclined with respect to the plane-of-sky, we additionally define a image plane by rotating the disk plane by as much as the disk inclination angle about the x-axis. We denote the directions of line of sight, north and east with unit vectors $\vec{r}$, $\vec{n}$ and $\vec{e}$ respectively. These can be written as follows.

$$\vec{r} = (0, -\sin i, \cos i) \tag{A.1}$$

$$\vec{n} = \frac{(\vec{r} \times \vec{z}) \times \vec{r}}{|(\vec{r} \times \vec{z}) \times \vec{r}|} \tag{A.2}$$

$$\vec{e} = \frac{-\vec{r} \times \vec{n}}{|\vec{r} \times \vec{n}|} \tag{A.3}$$

We substitute $i = 45°$, which is the HL Tau inclination angle derived by Kwon, Looney, and Mundy (2011), for Equation A.1 to derive the vectors in the plane-of-sky. This rotation yields the $\vec{n}$-axis and $\vec{n}$-axis that point in the direction of the minor and major axes of the disk, respectively. We note that although the disk position angle is measured to be 135° (Kwon, Looney, and Mundy, 2011), which can be expressed by rotating the image plane about the r-axis, we do not additionally rotate the image plane. It is because our purpose of the analysis is to reproduce the elliptical polarization pattern and uniform polarization in the azimuthal directions, both of which are not related to the disk position angle. Thus, in the semi-analytical models, the disk position angle is fixed at 90°.

On the disk plane defined above, we adopt a model of radial distributions of surface density and temperature. As done in Yang et al. (2019), we

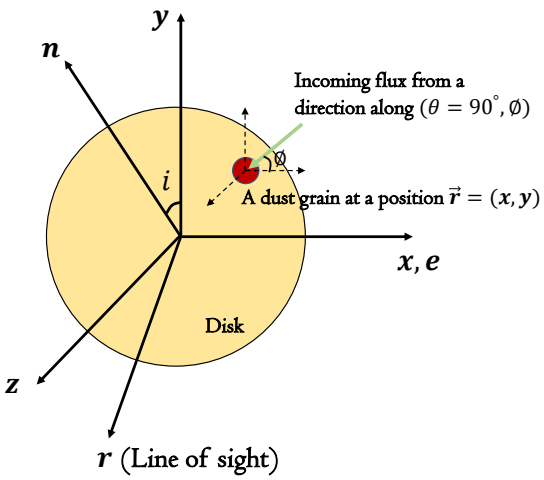

FIGURE A.1: Schematic illustration of defined disk and image frame. The disk plane is defined in the xy-plane and z-axis points perpendicular to the disk plane. The image plane is rotated by as much as the disk inclination angle i about the x-axis. As a result, the e-axis, n-axis and r-axis point in the directions of the east, north and line of sight, respectively.

adopt a model derived by Kwon, Looney, and Mundy (2011), which reproduced the HL Tau intensity distribution at 1.3 mm and 2.7 mm obtained on the CARMA. In the model, the radial distributions of the temperature and gas surface density are given with a power law radial distribution with the exponents of p and q.

$$T(r) = T_0 \left(\frac{r}{r_c}\right)^{-q}, \tag{A.4}$$

$$\Sigma(r) = \Sigma_0 \left(\frac{r}{r_c}\right)^{3/2-p-q/2} \exp\left[-\left(\frac{r}{r_c}\right)^{7/2-p-q/2}\right], \tag{A.5}$$

where r_c is a characteristic radius, where the surface density starts to exponentially decrease, T_0 and Σ_0 is the local temperature and surface density at the radius r_c.

Given Equation A.4, the distribution of the gas scale height can be derived. The gas scale height is given by

$$H(r) = \frac{c_s}{\Omega_k}, \tag{A.6}$$

where c_s is the local sound speed and Ω_k is the local Keplerian angular velocity. The sound speed is given by

$$c_s = \sqrt{\frac{kT}{\mu m_p}}, \tag{A.7}$$

where μ and m_p are the mean molecular weight and proton mass, respectively. The Keplerian angular velocity is given by

$$\Omega_k = \sqrt{\frac{GM_*}{r^3}}, \tag{A.8}$$

where G and M_* are the gravitational constant and the stellar mass, respectively. Substituting Equations A.7, A.8 into A.6, the scale height distribution is given by

$$H(r) = \sqrt{\frac{kTr^3}{\mu m_p GM_*}}. \tag{A.9}$$

As a result, with Equations A.4 and A.9, the distribution of the gas scale height is given with the power-law as

$$H(r) = H_0\left(\frac{r}{r_c}\right)^{3/2-q/2}, \tag{A.10}$$

where H_0 is the scale height for the gas at r_c. We adopt a set of parameters that Kwon, Looney, and Mundy (2011) found best fit the CARMA observations: r_c = 79 au, p = 1, and H_0 = 16.8 au.

A.0.2 Semi-analytical model of the alignment models (prolate and oblate grains)

In this section, we introduce the details of the grain alignment models. First, we put vector fields, which align the dust grains, on the disk explained above. Then, the models of prolate and oblate grains, both of which are developed by Draine (2003), are adopted to the disk.

To provide the polarization orientations on the disk, we define vector fields $\overrightarrow{V}$(x, y, z), which aligns elongated dust grains. As explained in the former section, the Gold alignment model predicts that gas flow on grains makes their long axes parallel to the flow. Therefore, to produce the azimuthal polarization morphology, the background vector filed needs to be in azimuthal (circular) as given by,

$$\overrightarrow{V}(x,y,z) = (-y/r, x/r, 0), \tag{A.11}$$

where r denotes a distance from the center in the disk plane with $r = \sqrt{x^2+y^2}$. The helicity-induced alignment model, on the other hand, predicts that the long axes of the elongated grains are aligned with the direction perpendicular to vector fields. Therefore, if the aligned grains are oblate, the background field is radial as written by

$$\overrightarrow{V}(x,y,z) = (x/r, y/r, 0). \tag{A.12}$$

Given the vector fields, we compute how polarization orientations would be observed when elongated grains are aligned by the vector fields defined

as Equations A.12 and A.11. The polarization orientations, as well as the polarization fractions, are determined by the vector fields projected on the plane-of-sky (or image plane). We thus need to decompose the vector fields $\vec{V}$ into components $\vec{V}_{\parallel}$ and $\vec{V}_{\perp}$, each of which is parallel to the line of sight and plane-of-sky and is given by

$$\vec{V}_{\parallel} = \vec{V} \cdot \vec{r} \tag{A.13}$$

$$\vec{V}_{\perp} = \vec{V} - \vec{V}_{\parallel}. \tag{A.14}$$

We derive the polarization angles, which are measured from the north axis to the east axis. As explained above, the alignment axes of prolate grains are parallel to the plane-of-sky components of the vector fields. Thus, when aligned grains are prolate, the polarization angles ϕ_p equals to the angles, which $\vec{V}_{\perp}$ makes with $\vec{n}$, and they are given by

$$\phi_p = \arccos \frac{\vec{V}_{\perp} \cdot \vec{n}}{|\vec{V}_{\perp}|}, \tag{A.15}$$

where assumed vector field $\vec{V}$ is circular (Equation A.11).

When the aligned grains are oblate, on the other hand, the alignment axis is perpendicular to the plane-of-sky components of the vector fields. Thus, the polarization angle is derived only by adding 90° to Equation A.15 as

$$\phi_p = \arccos \frac{\vec{V}_{\perp} \cdot \vec{n}}{|\vec{V}_{\perp}|} + 90^{\circ}, \tag{A.16}$$

where assumed vector field $\vec{V}$ is radial (Equation A.12).

By using the equations above, we can derive the expected polarization angles for both of the prolate and oblate grain models at all positions in the image plane. In the next subsection, we derive the polarization fraction at each location in the disk, which is dependent on the angles that the alignment axes make with the line of sight.

A.0.3 Polarization fraction of the prolate and oblate grains

To derive the polarization fraction in the disk, we need to assume the size, composition, and shape of the aligned grains. As introduced in Yang et al. (2019), we use grain models derived by Lee and Draine (1985). The polarization fraction at each location $p(x, y)$ is given by

$$p(x, y) = \frac{p_0 \times \sin^2 i_d(x, y)}{1 + p_0 \times \cos^2 i_d(x, y)}, \tag{A.17}$$

where p_0 is maximum polarization fraction and $i_d(x, y)$ is the angle between alignment axis and line of sight. When oblate grains are viewed edge-on, which is the case $i_d = 90^{\circ}$, the most efficient polarization are expected at

$p(x,y) = p_0$. Conversely, when they are viewed face-on, no polarized emission is expected since $i_d = 0°$. Substituting the viewing angles calculated at each location, the polarization fraction can be derived at all locations in the disk.

For the prolate grain model, where the long axes of the grains are parallel to the alignment axes, the polarization fraction at each position $p(x,y)$ is derived as follows

$$p(x,y) = \frac{p_0 \times \sin^2 i_d(x,y)}{1 - p_0 \times \cos^2 i_d(x,y)} \tag{A.18}$$

for small grains (Lee and Draine, 1985). In this model, the polarization fraction reaches maximum when the long axes of the grains are parallel to the plane-of-sky, whereas no polarization are expected when the axes are perpendicular to the plane-of-sky.

The polarization fraction and morphology can be computed with Equations A.15 and A.18 for the prolate grains, and A.16 and A.17 for the oblate grains. Since the disk model and background field is fixed, the parameter that determines the contribution to polarized emission is just the intrinsic polarization fraction p_0. To create the Stokes Q and U intensity for the alignment model, Stokes I intensity needs to be multiplied. As explained in the following, we use the Stokes I emission derived in the scattering model. In the next section, we additionally reconstruct the scattering model developed by Yang et al. (2016).

A.0.4 Source function of scattered waves

In this section, we reproduce the Yang et al. (2016) model of the scattering-induced polarization in inclined disks. We use the same coordinate systems of the disk and image plane as in the alignment model illustrated with Figure A.1. The model assumes that dust grains scatter incoming thermal emission from surrounding grains whose temperature is T.

To facilitate the computation of the model, the model put three assumptions: (1) the emission is optically thin at all radii (2) the thermal emission from dust grains is described with the Rayleigh-Jeans law so that the Planck function $B_\nu(T)$is

$$B_\nu(T) = \frac{2\nu^2 kT}{c^2}, \tag{A.19}$$

where k is the Boltzmann constant, and c is the light speed. (3) the only last scattering contributes to resultant scattered emission.

Note that these assumptions are necessarily not applicable to the HL Tau disk. Especially, Carrasco-González et al. (2019) has revealed that the HL Tau disk is optically thick even at the millimeter wavelengths contrary to the assumption (2). However, as explained in Section 1.2, we intend to investigate whether the scattering can solve the discrepancy between the theory and observation, and thus such approximations are not problematic for the purpose.

With the assumptions, we can derive source functions of all Stokes parameters except Stokes V. We suppose a situation that a dust grain at the position r scatters the emission coming from a direction polar angle θ and the azimuthal angle ϕ as illustrated in Figure A.1. The intensity of the scattered emission can be derived by an integration of the source function S_s along the line of sight (i.e. r-axis). The Source function S_s is given by

$$S_s(\vec{r}) = \frac{1}{\sigma_s} \int \frac{d\sigma}{d\Omega} I(\vec{r}, \theta, \phi) d\Omega, \tag{A.20}$$

where $I(\vec{r}, \theta, \phi)$ is the intensity of the unpolarized thermal emission seen by the scattering dust grains at a location $\vec{r}$ along a direction θ and ϕ, σ_s is scattering cross section, which is integrated with the solid angle Ω, and $d\sigma/d\Omega$ is the differential scattering cross section, which denotes how much the grains scatter the incoming emission $I(\vec{r}, \theta, \phi)$ into the line of sight.

The incoming emission to be scattered $I(\vec{r}, \theta, \phi)$ is given by an integration of the grain thermal emission over the optical depth along the direction (θ, ϕ). We denote the distance from the scatterer along the direction (θ, ϕ) with l and thus the unpolarized radiation is given by

$$I(\vec{r}, \theta, \phi) = \int B_\nu(T) d\tau_{abs} = \int \kappa_{abs}(\vec{r}_l) \frac{2\nu^2 kT}{c^2} \rho(\vec{r}_l) dl, \tag{A.21}$$

where $d\tau_{abs} = \kappa_{abs}\rho(\vec{r}_l)dl$ is the absorption optical depth, which is the product of the absorption opacity κ_{abs}, mass density of the grains ρ at a location $\vec{r}_l$, and the short length along direction (θ, ϕ) dl.

By substituting Equation A.21 into Equation A.20, the source function of the scattered emission is rewritten by

$$S_s(\vec{r}) = \frac{2\nu^2 k}{c^2 \sigma_s} \int_0^{2\pi} d\phi \int_0^{\infty} dl \int_0^{\pi} d\theta \frac{d\sigma}{d\Omega} \kappa(\vec{r}_l) \rho(\vec{r}_l) T(\vec{r}_l) \sin\theta. \tag{A.22}$$

To compute the integration A.22, we need to adopt some modifications to the equation. First, Yang et al. (2019) divided the source function A.22 into two components, S_0 and S_∞, as follows

$$S_s(\vec{r}) = S_{s,0} + S_{s,\infty}, \tag{A.23}$$

where

$$S_{s,0}(\vec{r}) \equiv \frac{2\nu^2 k}{c^2 \sigma_s} \int_0^{2\pi} d\phi \int_0^{H} dl \int_0^{\pi} d\theta \frac{d\sigma}{d\Omega} \kappa(\vec{r}_l) \rho(\vec{r}_l) T(\vec{r}_l) \sin\theta \tag{A.24}$$

and

$$S_{s,\infty}(\vec{r}) \equiv \frac{2\nu^2 k}{c^2 \sigma_s} \int_0^{2\pi} d\phi \int_H^{\infty} dl \int_0^{\pi} d\theta \frac{d\sigma}{d\Omega} \kappa(\vec{r}_l) \rho(\vec{r}_l) T(\vec{r}_l) \sin\theta, \tag{A.25}$$

each of which denotes the contribution to the incoming emission to be scattered at the location $\vec{r}$ from two distinct regions: $\S_{s,0}$ takes into account the

contributions from a region within a local distance on the order of dust scale height $H(\vec{r})$, while $\S_{s,\infty}$ does the whole contribution from a region beyond a local scale height. We hereafter refer to the two contributions as near- and far-contribution, respectively.

To compute the contributions given by Equations A.24 and A.25, Yang et al. (2019) additionally assumes that (4) the disk is geometrically thin along the direction $\vec{z}$, (5) the absorption opacity κ_{abs} is constant at all locations, and that the mass density ρ and temperature T are uniform within a distance on the order of the local scale height $H(\vec{r})$. The assumption (3) enables to confine the unpolarized radiation direct to the scatterer to $\delta\theta \sim 2H_l/l$ around $\theta = \pi/2$. Moreover, with the assumption (4) and (5), the quantities ρ and κ_{abs} can be moved outside the integral. Adopting the disk model explained above, Equation A.24 is rewritten by

$$S_{s,0}(\vec{r}) = \frac{2\nu^2 k \kappa_{abs} \Sigma(\vec{r}) T(\vec{r})}{c^2}. \tag{A.26}$$

For the far-field contribution denoted by S_∞, the assumption (3) enables to integrate over the polar angle θ in Equation A.25, and the assumption (4) move κ_{abs} to the outside of the integration. As a result, Equation A.25 is rewritten by

$$\begin{aligned} S_{s,\infty}(\vec{r}) &\approx \frac{2\nu^2 k \kappa_{abs}}{c^2 \sigma_s} \int_0^\pi d\phi \frac{d\sigma}{d\Omega} \int_H^\infty dl \frac{2\rho(\vec{r}_l) H(\vec{r}_l) T(\vec{r}_l)}{l} \\ &= \frac{2\nu^2 k \kappa_{abs}}{c^2 \sigma_s} \int_0^\pi d\phi \frac{d\sigma}{d\Omega} \int_H^\infty dl \frac{\Sigma(\vec{r}_l) T(\vec{r}_l)}{l}, \end{aligned} \tag{A.27}$$

where $\Sigma(\vec{r}_l)$ is the surface density at a location $\vec{r}_l$, which is given by $\Sigma(\vec{r}_l) = 2\rho(\vec{r}_l)\mathrm{H}(\vec{r}_l)$.

The last quantity to determine is the differential cross section $d\sigma/d\Omega$. Yang et al. (2016) assumed that the scatter scattering follows Rayleigh approximation, which is applicable when the grain sizes are smaller than the observation wavelength. This approximation yields the differential equation as to be

$$\frac{d\sigma}{d\Omega} = \frac{3\sigma_s}{16\pi}(1 + cos^2\theta_s), \tag{A.28}$$

where θ_s is the scattering angle, which the incoming emission along the direction ($\theta = 90^\circ$, ϕ) makes with the line of sight (i.e. along the $\vec{r}$). When we define an unit vector, which points in a direction of the incoming emission with $\vec{I} = (\sin\phi, \sin\phi, 0)$ (see Figure A.1), the scattering angle θ_s is given by

$$\cos\theta_s = \vec{I} \cdot \vec{r} = \sin i \cos\phi \tag{A.29}$$

The scattered emission is partially polarized with a fraction of p, which is given by

$$p = \frac{1 - cos^2\theta_s}{1 + cos^2\theta_s}. \tag{A.30}$$

When the scattering angle is $\theta = 90^\circ$, the scattered emission is fully polarized since $p = 1$.

As done in Section 1.2., the polarization angle is measured from the n-axis to the e-axis. Since the polarization direction is perpendicular to the incoming emission that is projected on the plane of sky, we decompose the emission vector to the vectors that direct to the line of sight $\vec{I}_{\parallel}$ and that lie in the plane of sky with $\vec{I}_{\perp}$. They are given by

$$\vec{I}_{\parallel} = (\vec{I}\cdot\vec{r})\vec{r} = \sin\phi\sin i \begin{pmatrix} 0 \\ -\sin i \\ \cos i \end{pmatrix} \tag{A.31}$$

$$\vec{I}_{\perp} = \vec{I} - \vec{I}_{\parallel} = \begin{pmatrix} -\cos\phi \\ -\sin\phi\cos^2 i \\ -\sin\phi\sin i\cos i \end{pmatrix} \tag{A.32}$$

Thus, the polarization angle is given by

$$\cos\phi = \frac{\vec{I}_{\perp}\cdot\vec{n}}{|\vec{I}_{\perp}|} = \frac{\cos i\cos\phi}{\sqrt{\sin^2\phi + \cos^2 i\cos^2\phi}}. \tag{A.33}$$

The intensity of the polarized emission is expressed by Stokes Q and U parameters. They can be derived by taking into account the polarization fraction (Equation A.30) and the polarization angles (Equation A.33) to the source function of the scattered emission (Equation A.27). The source functions of the Stokes Q and U are given by

$$S_{Q,\infty}(\vec{r}) \approx \frac{2\nu^2 k\kappa_{abs}}{c^2\sigma_s}\int_0^{2\pi} d\phi\frac{d\sigma}{d\Omega}\int_H^{\infty} dl\frac{\Sigma(\vec{r}_l)T(\vec{r}_l)}{l}p(\theta_s)\cos 2\phi_{PA} \tag{A.34}$$

$$S_{Q,\infty}(\vec{r}) \approx \frac{2\nu^2 k\kappa_{abs}}{c^2\sigma_s}\int_0^{2\pi} d\phi\frac{d\sigma}{d\Omega}\int_H^{\infty} dl\frac{\Sigma(\vec{r}_l)T(\vec{r}_l)}{l}p(\theta_s)\sin 2\phi_{PA} \tag{A.35}$$

Since we assume the optically thin emission at all radii, we can simply derive the resultant Stokes Q and U by multiplying the source functions and scattering optical depth $\tau_s = \kappa_{sca}\Sigma(\vec{r})/\cos i$ (where κ_{sca} is the scattering opacity): $Q = S_{Q,\infty}\,\tau_s$ and $U = S_{U,\infty}\,\tau_s$.

Unlike the case for the near-field contribution given by A.26, we cannot directly integrate Equations A.27, A.34, and A.35 by hand because the integral over l includes infinitely distant field. Instead, since we have all functions to be integrated in Equations A.34 and A.35, we derive the source functions by summing up the product of Equations A.28, A.29, A.30 and A.33 at each location.

Finally, we derive the Stokes I emission coming from the disk. To facilitate the modeling, we assume that the Stokes I emission is simply originate from direct thermal emission from the grains. Since the source function of thermal emission is the Planck function, direct thermal emission component I_d is the product of the Planck function (A.19) and the absorption optical depth τ_{abs} =

$\kappa_{abs}\Sigma(\vec{r})/\cos i$, as written by

$$I_d = \frac{2\nu^2 k \kappa_{abs}\Sigma(\vec{r})T(\vec{r})}{c^2 \cos i} \tag{A.36}$$

With the obtained Stokes I, Q and U intensity, we can derive the polarized intensity, polarization fraction, and polarization position angles, each of which is given by

$$PI = \sqrt{Q^2 + U^2}, \tag{A.37}$$

$$PF = \frac{PI}{I}, \tag{A.38}$$

and

$$\theta_{PA} = \frac{1}{2}\arctan\frac{U}{Q}. \tag{A.39}$$

To confirm whether the scattering model is correctly reconstructed, we reproduce a Figure 2 in the paper Yang et al. (2016) that presents images of the polarized intensity with the inclination angles of $i = 0°$, $30°$, $45°$ and $60°$, as shown in A.2. Comparing reconstructed model with the results in Yang et

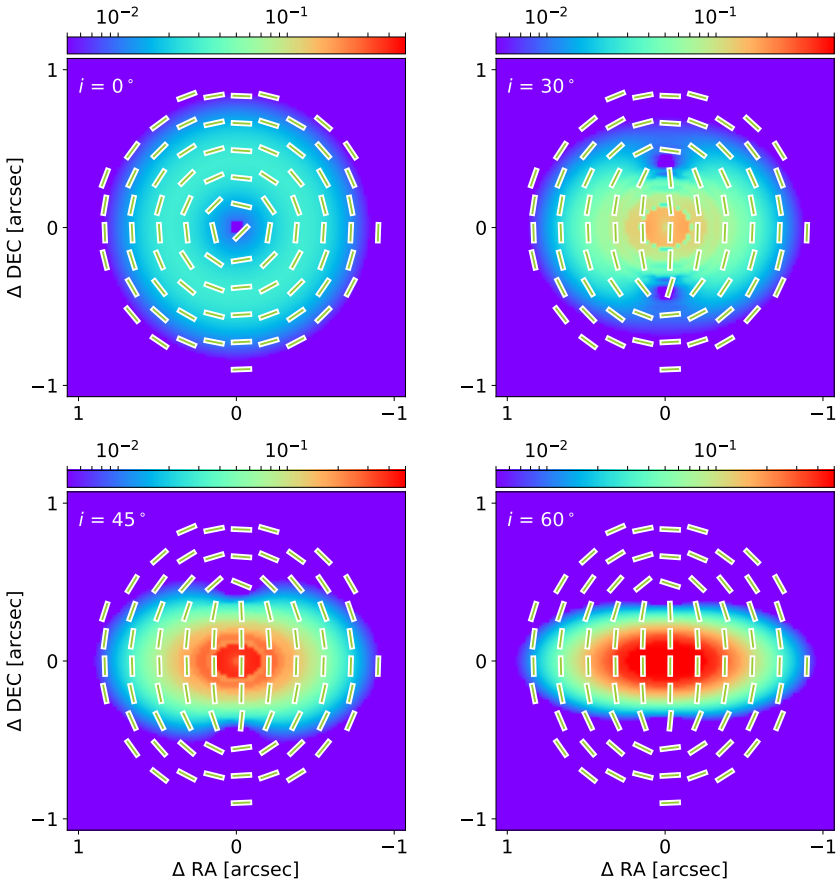

FIGURE A.2: Expected polarization morphology overlaid on the polarized intensity, showing the effects of disk inclination angles as done by Yang et al. (2016). The polarized intensity is normalized with a units of $2\Sigma_0^2\kappa_{abs}\kappa_{sca}\nu^2 kT_0/c^2$.

al. (2016), we confirm that the scattering model is successfully reconstructed and the polarization features in the scattering model are captured explained in Introduction Section.

A.0.5 Combined (scattering + alignment) model

In this section, we describe how to combine the alignment and scattering models presented above. By constructing the models explained above, we can obtain the polarization fraction and pattern for the alignment model, and the Stokes I, Q and U intensity for the scattering model. To derive the Stokes Q and U intensity for the alignment model, we use the Stokes I intensity provided in the scattering model and multiply that with polarization fraction $p(x, y)$ as written by

$$Q = I(x, y)p(x, y)\cos\phi_p \tag{A.40}$$

$$U = I(x, y)p(x, y)\sin\phi_p, \tag{A.41}$$

where the Stokes I, $p(x, y)$ and ϕ_p are given by Equations A.36, A.18 and A.15 for the prolate grains. (For the oblate grains, $p(x, y)$ and ϕ_p are given by Equations A.17 and A.16.)

To create the combined model, we compute the sum of Stokes Q and U intensity derived for each model. When combining the models, the controllable parameters that determine the intensity of scattered and thermal emission of the aligned grains are absorption/scattering opacity (κ_{abs} and κ_{sca}) and the intrinsic polarization fraction of the aligned grains (p_0). The polarization fraction and morphology in the combined model are determined by how the alignment and scattering contribute to the polarized emission. Between the three parameters, the absorption opacity κ_{abs} determines the absolute intensity for both the emission but does not determine the flux contribution from each emission because the parameter is equally involved in both of the emission. On the other hand, the scattering opacity κ_{sca} and the intrinsic polarization fraction p_0 are involved only in the intensity of scattered and thermal emission of the aligned grains, respectively. Therefore, the resultant polarization fraction and morphology can be modified by changing the parameter κ_{sca} and p_0. We construct the combined model with changing the parameters and compare it with the observed images after the beam averaging is adopted.

Appendix B

Appendix B

We describe how to construct the radiative transfer models of the grain alignment and self-scattering in detail whose brief explanations are described in Section 2.2.

B.1 Method (Radiative transfer modeling)

In section 3.3, by computing the semi-analytical model, we find that the polarization feature on the HL Tau disk at 3 mm can be reproduced by the mixture of the grain alignment and self-scattering model. Moreover, we also find that the Gold alignment model is preferred rather than helicity-induced alignment model.

In this section, to further examine the conclusions and constrain the grain sizes and shape quantitatively, we perform radiative transfer calculations with RADMC-3D (Dullemond et al., 2012). First, we perform Stokes I modeling to reproduce the observed continuum image obtained on the ALMA polarization observation. Then, we include the effect of thermal emission from the aligned and elongated grains. We also distinctly develop the self-scattering model. Finally, we combine the created Stokes I, Q, and U images.

B.1.1 Previous RAT model

In constructing semi-analytical models, we have used the disk model that fit the multiband observation using CARMA in 1.3 mm and 2.7 mm wavelength (Kwon, Looney, and Mundy, 2011). We first investigate whether the previous model can reproduce the Stokes I image obtained on the ALMA polarization observation in Band 3. Figure B.1 presents the Stokes I image obtained on the ALMA polarization observation, the RAT model developed by Kwon, Looney, and Mundy (2011), and residual map, which is observed Stokes I subtracted with the RAT model. The residual map shows that especially in the outer region of the disk, the model excessively produces the Stokes I emission. Therefore, we find that although the model is the best for the continuum obtained on CARMA, it does not necessarily reproduce the Stokes I emission obtained on the ALMA observation. Thus, we develop a new RAT model that can reproduce the tokes I image obtained on ALMA.

Note that recent studies have developed sophisticated RAT models that constrain multi-ringed and gaped structures revealed by the high resolution

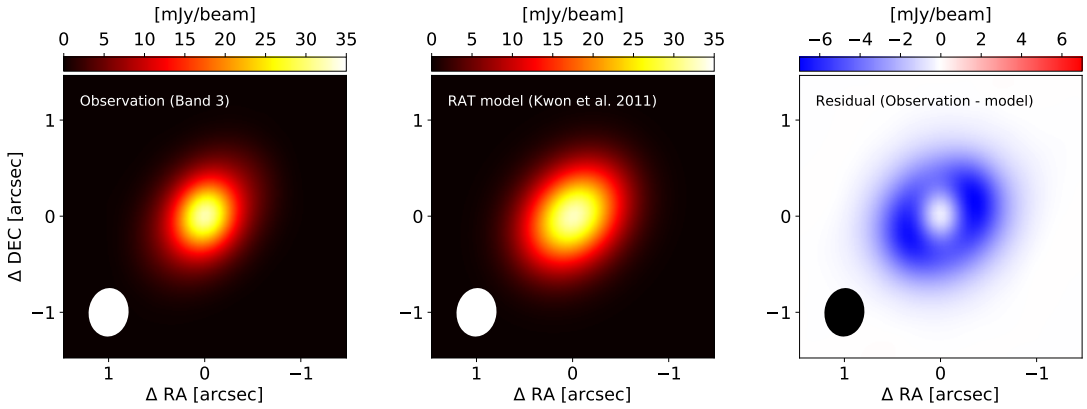

FIGURE B.1: The image of Stokes I emission obtained on ALMA (left panel), modeled image based on the previous RAT modeling (central panel), and residual map, where the observed Stokes I subtracted with modeled Stokes I.

observation (Pinte et al., 2016; Liu et al., 2017; Carrasco-González et al., 2019). However, the models require huge amounts of grid points for the disk substructure and machine- and time-demanding. Thus, we develop the geometrical model assuming smoothed surface density without any substructure. This approach is reasonable because we intend not to reproduce the detailed structure of the disk but the polarization features obtained on the ALMA observation with the coarse angular resolution compared to ALMA Partnership et al. (2015).

B.1.2 New RAT model in this study

To reproduce the observed Stokes I image, we model the radial profile of the optical depth τ. Modeling τ profiles has an advantageous in enabling to model the brightness without assuming grain model. The τ profile to be modeled is derived with

$$\tau_{obs}(r) = \frac{T_B(r)}{T(r)}, \tag{B.1}$$

where $T_B(r)$ is the brightness temperature profile and $T(r)$ is the temperature profile. Assuming Rayleigh-Jeans law, the brightness temperature profile is given by

$$T_B(r) = \frac{4\ln 2}{2\pi k}\frac{\lambda^2}{\theta_{MA}\theta_{MI}}F_\nu(r), \tag{B.2}$$

where θ_{MA} and θ_{MI} are the full widths at half power of the major and minor axes of the beam and F_ν is the observed flux density. To derive the τ profile, the other temperature profile $T(r)$ needs to be specified. We use the temperature profile that is used in Okuzumi and Tazaki (2019), which is given by

$$T(r) = 310\left(\frac{r}{1\,\mathrm{AU}}\right)^{-0.57} \quad K. \tag{B.3}$$

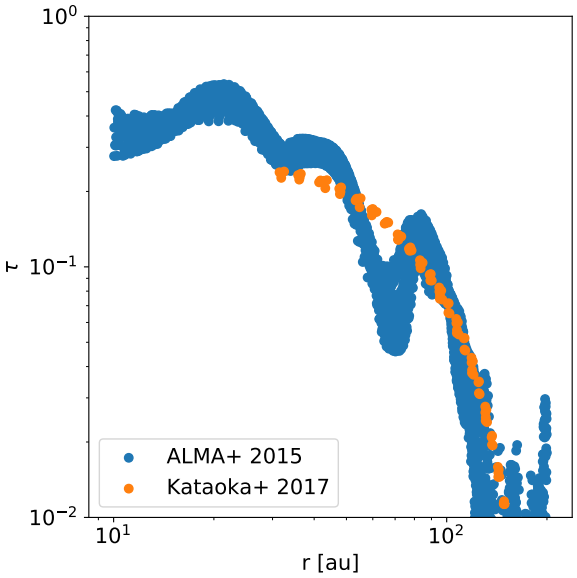

FIGURE B.2: The τ profiles derived with Equation B.1, B.2 and B.3. The blue and orange plots show the profiles for the continuum images obtained with high resolution observation ALMA Partnership et al. (2015) and polarization observation Kataoka et al. (2017), respectively.

We derive the τ profiles by inserting Equations B.2 and B.3 into B.1. Figure B.2 presents the derived profiles for the two continuum images obtained by Kataoka et al. (2017) and ALMA Partnership et al. (2015).

We model the derived τ profiles by assuming the power-law radial distribution with the exponents of γ_1 and γ_2 as given by,

$$\tau_{model}(r) = \tau_0 \left(\frac{r}{1\,\mathrm{AU}}\right)^{-\gamma_1} \exp\left[\left(\frac{r}{r_c}\right)^{-\gamma_2}\right], \tag{B.4}$$

where τ_0 is the optical depth at a location r = 1 au, r_c is the characteristic radius, beyond which the optical depth starts to exponentially decreases. The parameters to be determined are those four parameters (τ_0, r_c, γ_1, γ_2)

We search a model that best fits the profile obtained on the polarization observation as follows. First, we fix one of the exponents parameters γ_1 that determines the profiles in the central region and change the other parameters to search a best model. Then, with the best fit parameter set, we make the convolved Stokes I image and subtract it from the observed image. The tried parameters are listed in Table B.1

Figure B.3 shows the models with the parameters in B.1 overlaid on the τ_{obs} profiles in B.2. The profiles of the model 1 and 2 are obviously so shallow in the inner r < 30 au region, where large residuals remain in the inner region. Thus, larger γ_1 is needed to produce steeper τ_{model} profile in the radial direction.

Repeating the changes of γ_1 and the fitting, we evaluate the residual levels for each model. As a result, we find that the model 5 is the best model in

TABLE B.1: List of the tried parameters to fit the optical depth τ_{obs} profile

Model No.	τ_0	r_c	γ_1	γ_2
1	0.0	-2.0	84.4	0.28
2	0.5	-3.2	112.1	1.4
3	0.8	-4.8	123.5	4.2
4	0.9	-5.6	126.5	6.2
5	1.0	-6.6	129.2	9.0

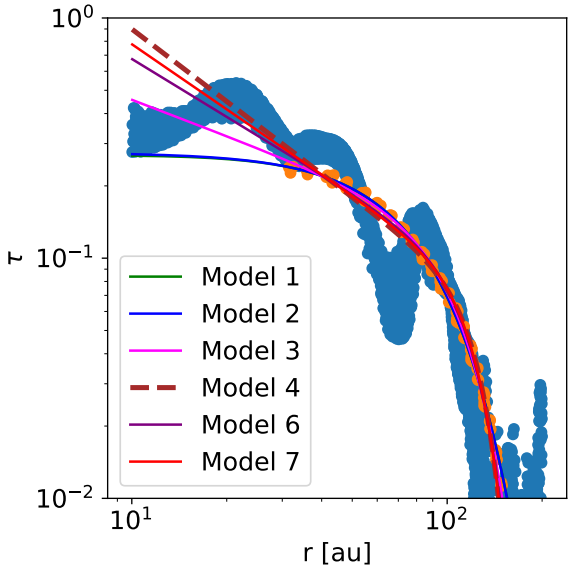

FIGURE B.3: The τ_{obs} profiles overlaid with the τ_{obs} assuming the parameter sets in B.1.

the tried parameter sets. Figure 2.2 presented in Section 2.2 shows the images of observed and modeled Stokes I produced by the model 5 and residual as done in Figure B.1

We note that there remains still residuals with the significant levels ($\sim$25 $\times$ σ_I). Moreover, the residuals show azimuthal variations between the near and far side of the disk, which is possibly due to more complex geometry than that in the assumed model. Although the origin of the residuals is uncertain, given the limited angular resolution and simplified model, we do not employ more detailed modeling because we intend to reproduce the polarization pattern and fractions with the resolutions of $\sim$0.1 % that is probably not affected by the residual level shown in Figure 2.2 in Section 2.2. Thus, we proceed to the next step with the acquired best model in the following.

B.1.3 Alignment model

Here, we include the effect of grain alignment in the ray-tracing to create the Stokes Q and U images. As is explained in subsection 3.1.2, the polarization fraction is sensitive to the grain axis ratio and viewing angle. Thus, we introduce two parameters α and ϵ, which denote the grain geometrical axis ratio and grain alignment efficiency, respectively.

We make a grain model to put on the disk by assuming the grain composition and size distribution. Note that in calculating the absorption and scattering opacities, the grains are assumed to be spherical. It is because that the Mie theory cannot be adopted non-spherical grains. We use a grain composition model developed by Birnstiel et al. (2018), where the grains are the mixture of silicate, troilite, organics, and water ice. The refractive index used in the calculation is as follows: Draine (2003) for astronomical silicate, Henning and Stognienko (1996) for troilite and refractory organics, and Warren and Brandt (2008) for water ice. We compute the mixture of them with the effective medium theory using the Maxwell-Garnett rule (e.g., Bohren and Huffman (1983) and Miyake and Nakagawa (1993)). We assume the grains have a power-law-size distribution with a power of q = -3.5 (Mathis, Rumpl, and Nordsieck, 1977) with the maximum grain size of a_{max}, while the minimum grain size is fixed at a_{min} = 0.05 μm.

With the assumed model, we produce the model of the polarized emission that purely comes from the thermal emission of the elongated grains. However, one problem is that RADMC-3D cannot compute the ray-tracing without the effect of scattering and separate the thermal emission and scattered emission. Thus, to virtually switch off the scattering, the maximum grain sizes are adjusted to where the scattering opacity is negligible compared to the absorption opacity. We fix the maximum size at a_{max} = 50 μm, where the absorption opacity κ_{abs} = 0.5 whereas the scattering opacity κ_{sca} = 0.01. At the fixed radius, the absorption opacity is almost constant within the range $a_{max} < \lambda/2\pi$. Thus, although we change the grain size in the scattering model, the contribution from the thermal emission of the aligned grains changes little compared to that of the scattered emission.

The apparent grain axis ratio of the elongated grains deviates from its original ratio when they are viewed inclined. It depends on the viewing angle, and thus changes location to location in the disks. Thus, we next develop an elongated grain model, which correctly describes the dependence. Figure B.4 presents the directions of the alignment axis and line of sight with the viewing angle of θ. The viewing angle is measured counterclockwise from the alignment axis and is given by

$$\cos\theta \equiv |\vec{n}_{align} \cdot \vec{n}_{los}|, \tag{B.5}$$

where $\vec{n}_{align}$ and $\vec{n}_{los}$ are the unit vectors, which point in the directions of alignment axis and line of sight, respectively. The alignment axis of the oblate grains is parallel to the short axes of the grain whereas that of the prolate grain is parallel to the long axes. Whichever the aligned grains are oblate or prolate, the maximum polarization fraction is expected when $\cos\theta = 0$ (θ

= 90°), which is the case that a dust grain is viewed edge-on. On the other hand, zero polarization fraction is expected when $\cos\theta = 1$ ($\theta = 0°$), which is the case that a dust grain is viewed face-on.

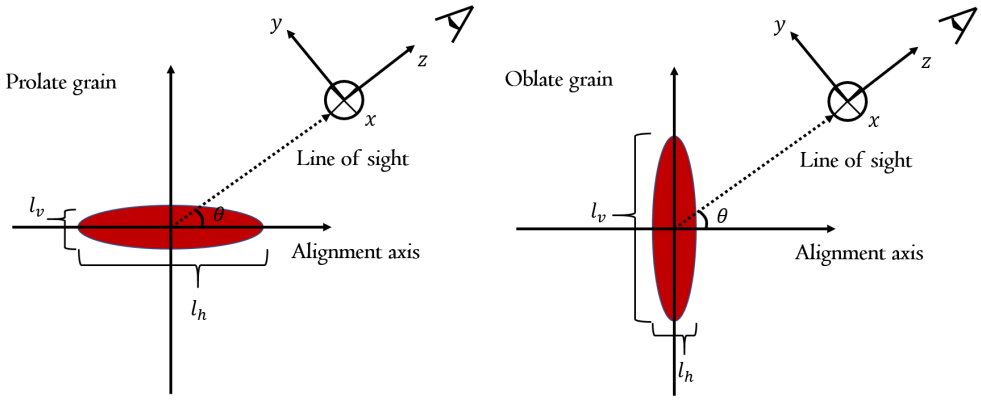

FIGURE B.4: Schematic illustrations of the aligned prolate (left) and oblate (oblate) grains, in which the alignment axis and the line of sight are defined. The viewing angle θ is measured counterclockwise from the alignment axis. The alignment axis of the prolate grain is parallel to the long axis of the grain, whereas that of the oblate grain is perpendicular to the short axis. The geometrical length of the two axes are also presented l_h and l_v, which is measured along the parallel and perpendicular to the alignment axis.

To quantitatively denote the angle dependence, we introduce the functions $\kappa_{abs,\nu,x}$ and $\kappa_{abs,\nu,y}$ as a function of the viewing angle θ. The functions are written by

$$\kappa_{abs,\nu,x} = \kappa_{abs,\nu} k_{\nu,x}(\theta) \tag{B.6}$$

and

$$\kappa_{abs,\nu,y} = \kappa_{abs,\nu} k_{\nu,y}(\theta), \tag{B.7}$$

where $k_{\nu,x}(\theta)$ and $k_{\nu,y}(\theta)$ are the dimensionless functions, each of which determines the opacity along the directions of x- and y-axis in the plane of sky. One condition is that when the grains randomly orient, the average opacity equals to the original opacity $\kappa_{abs,\nu}$:

$$\int_0^\infty \frac{1}{2}[\kappa_{abs,\nu,x}(\theta) + \kappa_{abs,\nu,y}(\theta)]d\mu = \kappa_{abs,\nu}, \tag{B.8}$$

or equivalently,

$$\int_0^1 \frac{1}{2}[k_{\nu,x}(\theta) + k_{\nu,y}(\theta)]d\mu = 1, \tag{B.9}$$

where $\mu = \cos\theta$.

We implement an additional parameter α, which is the original axis ratio of the aligned grains:

$$\alpha = \frac{l_v}{l_h} = \frac{k_{\nu,v}}{k_{\nu,h}}, \tag{B.10}$$

where l_v is the length along the direction that is parallel to the alignment axis, while l_h is the length along the direction that is perpendicular to the alignment axis (Figure B.4). The second modification in Equation B.10 assumes that $k_{\nu,v} \propto l_v$ and $k_{\nu,h} \propto l_h$. With the definition, the grains with $\alpha > 1$ are regarded as the prolate grains, whereas the grains with $\alpha < 1$ is regarded as the oblate grains. When we set $\alpha = 1$ then the grain is totally spherical and no polarization are expected.

To derive the functions $k_{\nu,x}(\theta)$ and $k_{\nu,y}(\theta)$, the relationship between the grain original axis ratio ($\alpha = k_v/k_h$) and projected axis ratio denoted with $k_{\nu,x}$ and $k_{\nu,y}$ need to be solved. One of the parameters $k_{\nu,x}$ is always equals to $k_{\nu,h}$ because the length l_x is constant at its original length for all the viewing angle θ.

$$k_{\nu,x} = k_{\nu,h} \tag{B.11}$$

The other parameter $k_{\nu,y}$, on the other hand, varies with the viewing angle. This can be derived by finding linear functions with the slope of $\tan\theta$ that contact with the ellipse. When we write the elliptical function with $x'^2/l_h^2 + y'^2/l_v^2 = 1$ and the linear function with $y' = (\tan\theta)x' + c$, the condition that the two equations have multiple root is $c = \pm\sqrt{l_v^2\cos^2\theta + l_h^2\sin^2\theta}$. The opacity projected on the plane of sky $k_{\nu,y}$ corresponds to the distance of two linear functions and is given by

$$k_{\nu,y} = \sqrt{k_{\nu,v}^2\sin^2\theta + k_{\nu,h}^2\cos^2\theta}. \tag{B.12}$$

By specifying the grain axis ratio α, we can compute the opacity for the two grain axes with Equations B.11 and B.12 as a function of the viewing angle θ.

Finally, we derive concrete values of the function $k_{\nu,x}(\theta)$ and $k_{\nu,y}(\theta)$ for each viewing angle θ. We substitute Equations B.11 and B.12 to B.9, yielding

$$k_{\nu,h} = 2\Big/\int_0^1 [\sqrt{\alpha^2\sin^2\theta + \cos^2\theta} + 1]d\theta, \tag{B.13}$$

where we use $k_v = \alpha k_h$. Replacing $\mu = \cos\theta$, Equation B.13 is rewritten by

$$\begin{aligned} k_{\nu,h} &= 2\Big/\int_0^1 \sqrt{\alpha^2 + (1-\alpha^2)\mu^2}d\mu \\ &= 2\Big/\sqrt{|1-\alpha^2|}\int_0^1 \sqrt{\mu^2 + \frac{\alpha^2}{|1-\alpha^2|}}d\mu. \end{aligned} \tag{B.14}$$

To derive the function $k_{\nu,h}$, we compute the integration in Equation B.14. Since the sign of $1-\alpha^2$ changes with α in Equation B.14, the integration is

distinctly performed for the prolate ($\alpha > 1$) and oblate grains ($\alpha < 1$). When the aligned grains are prolate ($\alpha > 1$),

$$k_{\nu,h} = 2 \Big/ \sqrt{\frac{3}{2} + \frac{\alpha^2}{2\sqrt{\alpha^2-1}} \sin^{-1}(\sqrt{1-\frac{1}{\alpha^2}})}, \tag{B.15}$$

where we use an equation $\int \frac{1}{\sqrt{x^2+a^2}} dx = \log(x + \sqrt{x^2+a^2}) + C$ to derive Equation B.15 (C is the integration constant). When the aligned grains are oblate ($\alpha < 1$),

$$k_{\nu,h} = 2 \Big/ [\frac{3}{2} + \frac{\sqrt{1-\alpha^2}}{2} [\frac{\alpha^2}{1-\alpha^2} \log(1 + \frac{1}{\sqrt{1-\alpha^2}}) - \frac{\alpha^2}{1-\alpha^2} \log(\frac{\alpha}{\sqrt{1-\alpha^2}})]], \tag{B.16}$$

where we use an equation $\int \frac{1}{\sqrt{x^2-a^2}} dx = \frac{1}{2}[x\sqrt{x^2-a^2} - a^2 \log x + \sqrt{x^2-a^2}] + C$ to derive Equation B.16.

Figure B.5 shows the functions k_x and k_y for the prolate and oblate grains derived with Equations B.15 and B.16. We substitute α = 0.85, 0.9, and 0.95 to Equation B.15 for the prolate grains, while α = 0.85, 0.9, and 0.95 to Equation B.16 for the oblate grains. For both of the grains, the grains seen from the directions of the alignment axis (i.e. $\theta = 0^\circ$) produce no asymmetry between the two functions k_x and k_y. As the viewing angle increases, the function k_y becomes larger or smaller for the prolate or oblate grains, respectively. The function k_x, on the other hand, is constant for the all angle as described above. The asymmetry between the two axes becomes maximum at the viewing angle $\theta = 90^\circ$, where the elongated grains are viewed edge-on. The shape of prolate or oblate grain is more elongated as the axis ratio is apart from $\alpha = 1$, resulting in the larger asymmetry between the two axes. The viewing angle of the prolate grains varies with the azimuthal directions from $\theta = 0^\circ$ to $\theta = i^\circ$.

B.1.4 Grain alignment efficiency

Alignment efficiency, which denotes how well the grains are aligned by some external sources, is another parameter to be specified. We additionally introduce a parameter ϵ_{align} to include an effect of the partial grain alignment. We implement the partial alignment in the ray-tracing by modifying Equations B.6 and B.7 as follows.

$$\kappa_{abs,\nu,x}(\theta) = \kappa_{abs,\nu}[\epsilon_{align} k_{\nu,x}(\theta) + 1 - \epsilon_{align}] \tag{B.17}$$

$$\kappa_{abs,\nu,y}(\theta) = \kappa_{abs,\nu}[\epsilon_{align} k_{\nu,y}(\theta) + 1 - \epsilon_{align}] \tag{B.18}$$

The case ϵ = 1 represents the situation that grains are completely aligned with external sources, resulting in high polarization efficiency. The case ϵ = 0, on the other hand, represents the situation that grains randomly orient and the opacity along with the directions of the x- and y-axis equal to the original opacity κ, resulting in no polarization. Since the parameter ϵ_{align}

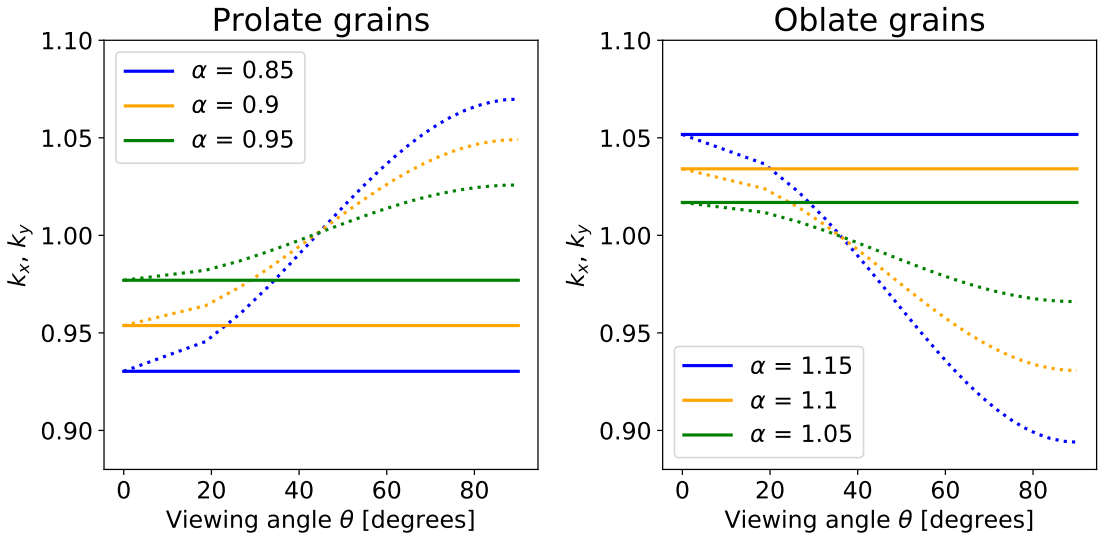

FIGURE B.5: The dimensionless functions k_x and k_y as a function of the viewing angle θ for the prolate (left) and oblate (right) grains. The solid lines represent the function along x-axis k_x, while the dotted lines represent the function along y-axis k_y. The three kind of the axis ratio values are color-coded in the each panels (α = 0.85, 0.9 and 0.95 for the prolate grains, and α = 1.15, 1.1 and 1.05 for the oblate grains).

is specified to a certain value and is constant in the whole disks, unlike the grain axis ratio α, it does not change the degree of polarization variations in the azimuthal directions but equally, contribute to polarized intensity in the whole disks.

B.1.5 Scattering model

The intensity of the scattered emission depends on the scattering opacity and phase functions, both of which depend on the grain radius. In creating the Stokes Q and U images for the self-scattering model, the grains are assumed to be spherical, unlike the alignment model. The polarization fraction becomes highest when the grain size is $a_{max} \sim \lambda/2\pi$, while it is reduced when the grain size is larger or smaller than that radius. The contributions to the polarized emission from the scattered emission are determined only by the grain maximum size of a_{max}. As done by Kataoka et al. (2015), we perform radiative transfer calculation taking into account multiple scattering. The created Stokes I, Q, and U images are convolved with a Gaussian beam as in the alignment model.

Appendix C

Appendix C

C.1 Statistical tests for examining the mechanical alignment model

We conduct a simple statistical analysis of the polarization angles to examine (1) which circular or elliptical pattern is compatible with the observed pattern, and (2) whether systematic angular deviations exist or not.

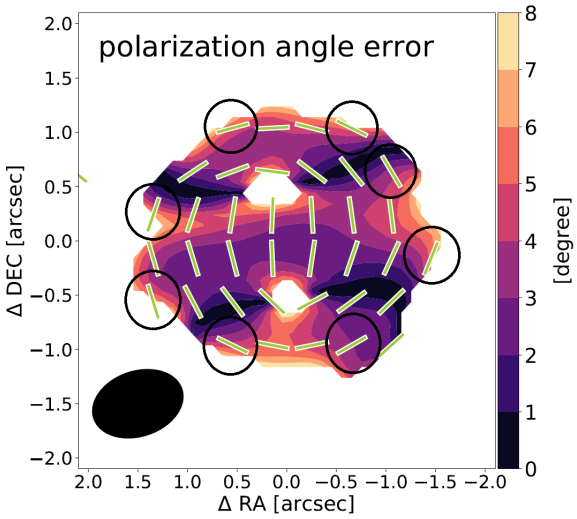

FIGURE C.1: The polarization angle error map and vectors. The vectors which are used for the statistical analysis are encircled in black.

For the analysis, each polarization angle should be independently sampled without the overlap of the synthesized beam. Thus, as shown in Figure C.1, we select the eight positions in the outer region, where the contamination from the central emission likely weak. Since the polarization angle error is obtained at the each position, the value of χ^2 can be calculated with the following equation.

$$\chi^2 = \sum_{i=1}^{8} \frac{\{\theta_{obs,i} - (\theta_{circle/ellipse,i} + \Delta\theta_{circle/ellipse})\}^2}{\sigma^2_{\theta,i}} \tag{C.1}$$

where $\theta_{obs,i}$, $\theta_{circle/ellipse,i}$ and $\sigma_{\theta,i}$ are the observed polarization angle, the position angle of the circular/elliptical tangent, and the polarization angle error at ith position, respectively. $\Delta\theta_i$ is weighted mean of the angular deviation from circular/elliptical tangents at ith position, which can be estimated with a following equation.

$$\Delta\theta_{circle/ellipse} = \sum_{i=1}^{8} \frac{(\theta_{obs,i} - \theta_{circle/ellipse,i})^2/\sigma_{\theta,i}^2}{1/\sigma_{\theta,i}^2} \tag{C.2}$$

The uncertainty of $\Delta\theta_{circle/ellipse}$, $\delta\theta$ can also be estimated with

$$\delta\theta = \sum_{i=1}^{8} \frac{1}{\sigma_{\theta,i}^2} \tag{C.3}$$

First, with Equations C.2 and C.3, we calculate the weighted mean of the angular deviation from circular/ellipse tangents and their uncertainties. Then, we substitute the values to Equation C.1 for the circular and elliptical cases. Equation C.3 yields $\Delta\theta_{circle} = -3.^\circ8 \pm 1.^\circ6$ and $\Delta\theta_{ellipse} = -4.^\circ5 \pm 1.^\circ6$, each of which corresponds to $\chi^2 = 25$ and 10, respectively. Thus, we conclude that the elliptical pattern is preferred rather than the circular pattern. This is the answer for (1) described above. At the same time, the mean value of the angular deviations from the elliptical tangents is $\Delta\theta_{ellipse} = -4.^\circ5 \pm 1.^\circ6$, which significantly deviates from 0. Therefore, we also conclude that there is the systematic angular deviation from the elliptical tangents. This is the answer for (2).

References

Aikawa, Y. et al. (May 2002). "Warm molecular layers in protoplanetary disks". In: *Astronomy and Astrophysics* 386, pp. 622–632. DOI: 10.1051/0004-6361:20020037. arXiv: astro-ph/0202060 [astro-ph].

Akeson, R. L. and J. E. Carlstrom (Dec. 1997). "Magnetic Field Structure in Protostellar Envelopes". In: *The Astrophysical Journal* 491(1), pp. 254–266. DOI: 10.1086/304949.

Alexander, R. D., C. J. Clarke, and J. E. Pringle (June 2006a). "Photoevaporation of protoplanetary discs - I. Hydrodynamic models". In: *Monthly Notice of Royal Astronomical Society* 369(1), pp. 216–228. DOI: 10.1111/j.1365-2966.2006.10293.x. arXiv: astro-ph/0603253 [astro-ph].

Alexander, R. D., C. J. Clarke, and J. E. Pringle (June 2006b). "Photoevaporation of protoplanetary discs - II. Evolutionary models and observable properties". In: *Monthly Notice of Royal Astronomical Society* 369(1), pp. 229–239. DOI: 10.1111/j.1365-2966.2006.10294.x. arXiv: astro-ph/0603254 [astro-ph].

ALMA Partnership et al. (July 2015). "The 2014 ALMA Long Baseline Campaign: First Results from High Angular Resolution Observations toward the HL Tau Region". In: *The Astrophysical Journal Letters* 808(1), L3, p. L3. DOI: 10.1088/2041-8205/808/1/L3. arXiv: 1503.02649 [astro-ph.SR].

Alves, F. O. et al. (Aug. 2018). "Magnetic field in a young circumbinary disk". In: *Astronomy and Astrophysics* 616, A56, A56. DOI: 10.1051/0004-6361/201832935. arXiv: 1805.00494 [astro-ph.SR].

Alves, João F., Charles J. Lada, and Elizabeth A. Lada (Jan. 2001). "Internal structure of a cold dark molecular cloud inferred from the extinction of background starlight". In: *Nature* 409(6817), pp. 159–161.

Andre, Philippe and Thierry Montmerle (Jan. 1994). "From T Tauri Stars to Protostars: Circumstellar Material and Young Stellar Objects in the rho Ophiuchi Cloud". In: *The Astrophysical Journal* 420, p. 837. DOI: 10.1086/173608.

Andrews, Sean M. and Jonathan P. Williams (Oct. 2005). "Circumstellar Dust Disks in Taurus-Auriga: The Submillimeter Perspective". In: *The Astrophysical Journal* 631(2), pp. 1134–1160. DOI: 10.1086/432712. arXiv: astro-ph/0506187 [astro-ph].

Andrews, Sean M. and Jonathan P. Williams (Apr. 2007). "High-Resolution Submillimeter Constraints on Circumstellar Disk Structure". In: *The Astrophysical Journal* 659(1), pp. 705–728. DOI: 10.1086/511741. arXiv: astro-ph/0610813 [astro-ph].

Andrews, Sean M. et al. (Aug. 2009). "Protoplanetary Disk Structures in Ophiuchus". In: *The Astrophysical Journal* 700(2), pp. 1502–1523. DOI: 10.1088/0004-637X/700/2/1502. arXiv: 0906.0730 [astro-ph.EP].

Andrews, Sean M. et al. (Nov. 2010). "Protoplanetary Disk Structures in Ophiuchus. II. Extension to Fainter Sources". In: *The Astrophysical Journal* 723(2), pp. 1241–1254. DOI: 10.1088/0004-637X/723/2/1241. arXiv: 1007.5070 [astro-ph.SR].

Andrews, Sean M. et al. (May 2011). "Resolved Images of Large Cavities in Protoplanetary Transition Disks". In: *The Astrophysical Journal* 732(1), 42, p. 42. DOI: 10.1088/0004-637X/732/1/42. arXiv: 1103.0284 [astro-ph.GA].

Andrews, Sean M. et al. (July 2013). "The Mass Dependence between Protoplanetary Disks and their Stellar Hosts". In: *The Astrophysical Journal* 771(2), 129, p. 129. DOI: 10.1088/0004-637X/771/2/129. arXiv: 1305.5262 [astro-ph.SR].

Andrews, Sean M. et al. (Apr. 2016). "Ringed Substructure and a Gap at 1 au in the Nearest Protoplanetary Disk". In: *The Astrophysical Journal Letters* 820(2), L40, p. L40. DOI: 10.3847/2041-8205/820/2/L40. arXiv: 1603.09352 [astro-ph.EP].

Anglada, Guillem et al. (June 2007). "Proper Motions of the Jets in the Region of HH 30 and HL/XZ Tau: Evidence for a Binary Exciting Source of the HH 30 Jet". In: *The Astronomical Journal* 133(6), pp. 2799–2814. DOI: 10.1086/517493. arXiv: astro-ph/0703155 [astro-ph].

Ansdell, M. et al. (Sept. 2016). "ALMA Survey of Lupus Protoplanetary Disks. I. Dust and Gas Masses". In: *The Astrophysical Journal* 828(1), 46, p. 46. DOI: 10.3847/0004-637X/828/1/46. arXiv: 1604.05719 [astro-ph.EP].

Ansdell, M. et al. (May 2017). "An ALMA Survey of Protoplanetary Disks in the σ Orionis Cluster". In: *The Astronomical Journal* 153(5), 240, p. 240. DOI: 10.3847/1538-3881/aa69c0. arXiv: 1703.08546 [astro-ph.EP].

Ansdell, Megan, Jonathan P. Williams, and Lucas A. Cieza (June 2015). "A SCUBA-2 850-micron Survey of Circumstellar Disks in the λ Orionis Cluster". In: *The Astrophysical Journal* 806(2), 221, p. 221. DOI: 10.1088/0004-637X/806/2/221. arXiv: 1505.00262 [astro-ph.EP].

Avenhaus, Henning et al. (Feb. 2014). "Structures in the Protoplanetary Disk of HD142527 Seen in Polarized Scattered Light". In: *The Astrophysical Journal* 781(2), 87, p. 87. DOI: 10.1088/0004-637X/781/2/87. arXiv: 1311.7088 [astro-ph.SR].

Avenhaus, Henning et al. (Aug. 2018). "Disks around T Tauri Stars with SPHERE (DARTTS-S). I. SPHERE/IRDIS Polarimetric Imaging of Eight Prominent T Tauri Disks". In: *The Astrophysical Journal* 863(1), 44, p. 44. DOI: 10.3847/1538-4357/aab846. arXiv: 1803.10882 [astro-ph.SR].

Bacciotti, Francesca et al. (Oct. 2018). "ALMA Observations of Polarized Emission toward the CW Tau and DG Tau Protoplanetary Disks: Constraints on Dust Grain Growth and Settling". In: *The Astrophysical Journal Letters* 865(2), L12, p. L12. DOI: 10.3847/2041-8213/aadf87. arXiv: 1809.02559 [astro-ph.SR].

Bae, Jaehan, Zhaohuan Zhu, and Lee Hartmann (Dec. 2017). "On the Formation of Multiple Concentric Rings and Gaps in Protoplanetary Disks". In: *The Astrophysical Journal* 850(2), 201, p. 201. DOI: 10.3847/1538-4357/aa9705. arXiv: 1706.03066 [astro-ph.EP].

Bai, Xue-Ning and James M. Stone (May 2013). "Wind-driven Accretion in Protoplanetary Disks. I. Suppression of the Magnetorotational Instability and Launching of the Magnetocentrifugal Wind". In: *The Astrophysical Journal* 769(1), 76, p. 76. DOI: 10.1088/0004-637X/769/1/76. arXiv: 1301.0318 [astro-ph.EP].

Bai, Xue-Ning and James M. Stone (Nov. 2014). "Magnetic Flux Concentration and Zonal Flows in Magnetorotational Instability Turbulence". In: *The Astrophysical Journal* 796(1), 31, p. 31. DOI: 10.1088/0004-637X/796/1/31. arXiv: 1409.2512 [astro-ph.HE].

Balbus, Steven A. and John F. Hawley (July 1991). "A Powerful Local Shear Instability in Weakly Magnetized Disks. I. Linear Analysis". In: *The Astrophysical Journal* 376, p. 214. DOI: 10.1086/170270.

Barenfeld, Scott A. et al. (Aug. 2016). "ALMA Observations of Circumstellar Disks in the Upper Scorpius OB Association". In: *The Astrophysical Journal* 827(2), 142, p. 142. DOI: 10.3847/0004-637X/827/2/142. arXiv: 1605.05772 [astro-ph.EP].

Barge, P. and J. Sommeria (Mar. 1995). "Did planet formation begin inside persistent gaseous vortices?" In: *Astronomy and Astrophysics* 295, pp. L1–L4. arXiv: astro-ph/9501050 [astro-ph].

Beckwith, Steven V. W. and Anneila I. Sargent (Nov. 1991). "Particle Emissivity in Circumstellar Disks". In: *The Astrophysical Journal* 381, p. 250. DOI: 10.1086/170646.

Birnstiel, T., C. P. Dullemond, and F. Brauer (Aug. 2009). "Dust retention in protoplanetary disks". In: *Astronomy and Astrophysics* 503(1), pp. L5–L8. DOI: 10.1051/0004-6361/200912452. arXiv: 0907.0985 [astro-ph.EP].

Birnstiel, T., C. P. Dullemond, and F. Brauer (Apr. 2010). "Gas- and dust evolution in protoplanetary disks". In: *Astronomy and Astrophysics* 513, A79, A79. DOI: 10.1051/0004-6361/200913731. arXiv: 1002.0335 [astro-ph.EP].

Birnstiel, Tilman et al. (Dec. 2018). "The Disk Substructures at High Angular Resolution Project (DSHARP). V. Interpreting ALMA Maps of Protoplanetary Disks in Terms of a Dust Model". In: *The Astrophysical Journal Letters* 869(2), L45, p. L45. DOI: 10.3847/2041-8213/aaf743. arXiv: 1812.04043 [astro-ph.SR].

Blandford, R. D. and D. G. Payne (June 1982). "Hydromagnetic flows from accretion disks and the production of radio jets." In: *Monthly Notice of Royal Astronomical Society* 199, pp. 883–903. DOI: 10.1093/mnras/199.4.883.

Blum, J. and G. Wurm (Sept. 2008). "The growth mechanisms of macroscopic bodies in protoplanetary disks." In: *Annual Review of Astronomy and Astrophysics* 46, pp. 21–56. DOI: 10.1146/annurev.astro.46.060407.145152.

Boehler, Y. et al. (Feb. 2018). "The Complex Morphology of the Young Disk MWC 758: Spirals and Dust Clumps around a Large Cavity". In: *The Astrophysical Journal* 853(2), 162, p. 162. DOI: 10.3847/1538-4357/aaa19c. arXiv: 1712.08845 [astro-ph.EP].

Bohren, Craig F. and Donald R. Huffman (1983). *Absorption and scattering of light by small particles*.

Bok, Bart J. (1948). "Dimensions and Masses of Dark Nebulae". In: *Centennial Symposia, December 1946. Harvard Observatory Monographs, No. 7. Contributions on Interstellar Matter, Electronic and Computational Devices, Eclipsing Binaries, The Gaseous Envelope of the Earth. Cambridge, MA: Harvard Observatory, 1948., p.53*. Vol. 7, p. 53.

Bok, Bart J., Carolyn S. Cordwell, and Richard H. Cromwell (Jan. 1971). "Dark Nebulae, Globules and Protostars". In: *Dark nebulae, Globules and Protostars*. Ed. by Beverly T. Lynds, p. 33.

Bouvier, J. and I. Appenzeller (Feb. 1992). "A magnitude-limited spectroscopic and photometric survey of rho OphiuchusX-ray sources." In: *Astronomy and Astrophysics Supplement Series* 92, pp. 481–516.

Brandenburg, Axel et al. (June 1995). "Dynamo-generated Turbulence and Large-Scale Magnetic Fields in a Keplerian Shear Flow". In: *The Astrophysical Journal* 446, p. 741. DOI: 10.1086/175831.

Brauer, F., C. P. Dullemond, and Th. Henning (Mar. 2008). "Coagulation, fragmentation and radial motion of solid particles in protoplanetary disks". In: *Astronomy and Astrophysics* 480(3), pp. 859–877. DOI: 10.1051/0004-6361:20077759. arXiv: 0711.2192 [astro-ph].

Canovas, H. et al. (Aug. 2013). "Near-infrared imaging polarimetry of HD 142527". In: *Astronomy and Astrophysics* 556, A123, A123. DOI: 10.1051/0004-6361/201321924. arXiv: 1306.6379 [astro-ph.SR].

Carpenter, John M., Luca Ricci, and Andrea Isella (May 2014). "An ALMA Continuum Survey of Circumstellar Disks in the Upper Scorpius OB Association". In: *The Astrophysical Journal* 787(1), 42, p. 42. DOI: 10.1088/0004-637X/787/1/42. arXiv: 1404.0387 [astro-ph.SR].

Carrasco-González, Carlos et al. (Apr. 2016). "The VLA View of the HL Tau Disk: Disk Mass, Grain Evolution, and Early Planet Formation". In: *The Astrophysical Journal Letters* 821(1), L16, p. L16. DOI: 10.3847/2041-8205/821/1/L16. arXiv: 1603.03731 [astro-ph.SR].

Carrasco-González, Carlos et al. (Sept. 2019). "The Radial Distribution of Dust Particles in the HL Tau Disk from ALMA and VLA Observations". In: *The Astrophysical Journal* 883(1), 71, p. 71. DOI: 10.3847/1538-4357/ab3d33. arXiv: 1908.07140 [astro-ph.EP].

Casassus, Simon et al. (Jan. 2013). "Flows of gas through a protoplanetary gap". In: *Nature* 493(7431), pp. 191–194. DOI: 10.1038/nature11769. arXiv: 1305.6062 [astro-ph.GA].

Chiang, E. I. and P. Goldreich (Nov. 1997). "Spectral Energy Distributions of T Tauri Stars with Passive Circumstellar Disks". In: *The Astrophysical Journal* 490(1), pp. 368–376. DOI: 10.1086/304869. arXiv: astro-ph/9706042 [astro-ph].

Chiang, E. I. et al. (Feb. 2001). "Spectral Energy Distributions of Passive T Tauri and Herbig Ae Disks: Grain Mineralogy, Parameter Dependences, and Comparison with Infrared Space Observatory LWS Observations". In: *The Astrophysical Journal* 547(2), pp. 1077–1089. DOI: 10.1086/318427. arXiv: astro-ph/0009428 [astro-ph].

Cho, Jungyeon and A. Lazarian (Nov. 2007). "Grain Alignment and Polarized Emission from Magnetized T Tauri Disks". In: *The Astrophysical Journal*

669(2), pp. 1085–1097. DOI: 10.1086/521805. arXiv: astro-ph/0611280 [astro-ph].

Cieza, Lucas et al. (Sept. 2007). "The Spitzer c2d Survey of Weak-Line T Tauri Stars. II. New Constraints on the Timescale for Planet Building". In: *The Astrophysical Journal* 667(1), pp. 308–328. DOI: 10.1086/520698. arXiv: 0706.0563 [astro-ph].

Cieza, Lucas A. et al. (Dec. 2017). "ALMA Observations of Elias 2-24: A Protoplanetary Disk with Multiple Gaps in the Ophiuchus Molecular Cloud". In: *The Astrophysical Journal Letters* 851(2), L23, p. L23. DOI: 10.3847/2041-8213/aa9b7b. arXiv: 1711.06905 [astro-ph.EP].

Clampin, M. et al. (July 2003). "Hubble Space Telescope ACS Coronagraphic Imaging of the Circumstellar Disk around HD 141569A". In: *The Astronomical Journal* 126(1), pp. 385–392. DOI: 10.1086/375460. arXiv: astro-ph/0303605 [astro-ph].

Clarke, C. J. et al. (Oct. 2018). "High-resolution Millimeter Imaging of the CI Tau Protoplanetary Disk: A Massive Ensemble of Protoplanets from 0.1 to 100 au". In: *The Astrophysical Journal Letters* 866(1), L6, p. L6. DOI: 10.3847/2041-8213/aae36b. arXiv: 1809.08147 [astro-ph.EP].

Coudé, Simon et al. (June 2019). "The JCMT BISTRO Survey: The Magnetic Field of the Barnard 1 Star-forming Region". In: *The Astrophysical Journal* 877(2), 88, p. 88. DOI: 10.3847/1538-4357/ab1b23. arXiv: 1904.07221 [astro-ph.GA].

Cox, Erin G. et al. (Mar. 2018). "ALMA's Polarized View of 10 Protostars in the Perseus Molecular Cloud". In: *The Astrophysical Journal* 855(2), 92, p. 92. DOI: 10.3847/1538-4357/aaacd2. arXiv: 1802.00449 [astro-ph.SR].

Cudlip, W. et al. (Sept. 1982). "Far infrared polarimetry of W51A and M42". In: *Monthly Notice of Royal Astronomical Society* 200, pp. 1169–1173. DOI: 10.1093/mnras/200.4.1169.

Dartois, E., A. Dutrey, and S. Guilloteau (Feb. 2003). "Structure of the DM Tau Outer Disk: Probing the vertical kinetic temperature gradient". In: *Astronomy and Astrophysics* 399, pp. 773–787. DOI: 10.1051/0004-6361:20021638.

Das, Indrajit and Joseph C. Weingartner (Apr. 2016). "Alignment of interstellar grains by mechanical torques: suprathermally rotating Gaussian random spheres". In: *Monthly Notice of Royal Astronomical Society* 457(2), pp. 1958–1987. DOI: 10.1093/mnras/stw146. arXiv: 1602.04775 [astro-ph.GA].

Davis Leverett, Jr. and Jesse L. Greenstein (Sept. 1951). "The Polarization of Starlight by Aligned Dust Grains." In: *The Astrophysical Journal* 114, p. 206. DOI: 10.1086/145464.

Dent, W. R. F. et al. (Jan. 2019). "Submillimetre dust polarization and opacity in the HD163296 protoplanetary ring system". In: *Monthly Notice of Royal Astronomical Society* 482(1), pp. L29–L33. DOI: 10.1093/mnrasl/sly181. arXiv: 1809.09185 [astro-ph.EP].

Dipierro, G. et al. (Apr. 2018). "Rings and gaps in the disc around Elias 24 revealed by ALMA". In: *Monthly Notice of Royal Astronomical Society* 475(4), pp. 5296–5312. DOI: 10.1093/mnras/sty181. arXiv: 1801.05812 [astro-ph.EP].

Dipierro, Giovanni et al. (July 2015). "Dust trapping by spiral arms in gravitationally unstable protostellar discs". In: *Monthly Notice of Royal Astronomical Society* 451(1), pp. 974–986. DOI: 10.1093/mnras/stv970. arXiv: 1504.08099 [astro-ph.SR].

Dong, Ruobing, Joan R. Najita, and Sean Brittain (Aug. 2018). "Spiral Arms in Disks: Planets or Gravitational Instability?" In: *The Astrophysical Journal* 862(2), 103, p. 103. DOI: 10.3847/1538-4357/aaccfc. arXiv: 1806.05183 [astro-ph.SR].

Dong, Ruobing et al. (July 2017). "Multiple Disk Gaps and Rings Generated by a Single Super-Earth". In: *The Astrophysical Journal* 843(2), 127, p. 127. DOI: 10.3847/1538-4357/aa72f2. arXiv: 1705.04687 [astro-ph.EP].

Draine, B. T. (Jan. 2003). "Interstellar Dust Grains". In: *Annual Review of Astronomy and Astrophysics* 41, pp. 241–289. DOI: 10.1146/annurev.astro.41.011802.094840. arXiv: astro-ph/0304489 [astro-ph].

Draine, B. T. (Jan. 2006). "On the Submillimeter Opacity of Protoplanetary Disks". In: *The Astrophysical Journal* 636(2), pp. 1114–1120. DOI: 10.1086/498130. arXiv: astro-ph/0507292 [astro-ph].

Dullemond, C. P. et al. (Feb. 2012). *RADMC-3D: A multi-purpose radiative transfer tool*. ascl: 1202.015.

Espaillat, C. et al. (Dec. 2007a). "On the Diversity of the Taurus Transitional Disks: UX Tauri A and LkCa 15". In: *The Astrophysical Journal Letters* 670(2), pp. L135–L138. DOI: 10.1086/524360. arXiv: 0710.2892 [astro-ph].

Espaillat, C. et al. (July 2010). "Unveiling the Structure of Pre-transitional Disks". In: *The Astrophysical Journal* 717(1), pp. 441–457. DOI: 10.1088/0004-637X/717/1/441. arXiv: 1005.2365 [astro-ph.SR].

Espaillat, Catherine et al. (Aug. 2007b). "Probing the Dust and Gas in the Transitional Disk of CS Cha with Spitzer". In: *The Astrophysical Journal Letters* 664(2), pp. L111–L114. DOI: 10.1086/520879. arXiv: 0707.0019 [astro-ph].

Espaillat, Catherine et al. (Aug. 2008). "Confirmation of a Gapped Primordial Disk around LkCa 15". In: *The Astrophysical Journal Letters* 682(2), p. L125. DOI: 10.1086/591270. arXiv: 0807.2291 [astro-ph].

Favre, Cécile et al. (Jan. 2019). "Gas Density Perturbations Induced by One or More Forming Planets in the AS 209 Protoplanetary Disk as Seen with ALMA". In: *The Astrophysical Journal* 871(1), 107, p. 107. DOI: 10.3847/1538-4357/aaf80c.

Fedele, D. et al. (Feb. 2010). "Timescale of mass accretion in pre-main-sequence stars". In: *Astronomy and Astrophysics* 510, A72, A72. DOI: 10.1051/0004-6361/200912810. arXiv: 0911.3320 [astro-ph.SR].

Fedele, D. et al. (Apr. 2017). "ALMA unveils rings and gaps in the protoplanetary system <ASTROBJ>HD 169142</ASTROBJ>: signatures of two giant protoplanets". In: *Astronomy and Astrophysics* 600, A72, A72. DOI: 10.1051/0004-6361/201629860. arXiv: 1702.02844 [astro-ph.SR].

Fedele, D. et al. (Feb. 2018). "ALMA continuum observations of the protoplanetary disk AS 209. Evidence of multiple gaps opened by a single planet". In: *Astronomy and Astrophysics* 610, A24, A24. DOI: 10.1051/0004-6361/201731978. arXiv: 1711.05185 [astro-ph.EP].

Ferreira, J., C. Dougados, and S. Cabrit (July 2006). "Which jet launching mechanism(s) in T Tauri stars?" In: *Astronomy and Astrophysics* 453(3), pp. 785–796. DOI: 10.1051/0004-6361:20054231. arXiv: astro-ph/0604053 [astro-ph].

Fromang, S. and R. P. Nelson (Oct. 2006). "Global MHD simulations of stratified and turbulent protoplanetary discs. I. Model properties". In: *Astronomy and Astrophysics* 457(1), pp. 343–358. DOI: 10.1051/0004-6361:20065643. arXiv: astro-ph/0606729 [astro-ph].

Fukagawa, Misato et al. (Apr. 2004). "Spiral Structure in the Circumstellar Disk around AB Aurigae". In: *The Astrophysical Journal Letters* 605(1), pp. L53–L56. DOI: 10.1086/420699.

Fukagawa, Misato et al. (Jan. 2006). "Near-Infrared Images of Protoplanetary Disk Surrounding HD 142527". In: *The Astrophysical Journal Letters* 636(2), pp. L153–L156. DOI: 10.1086/500128.

Fukagawa, Misato et al. (Dec. 2013). "Local Enhancement of the Surface Density in the Protoplanetary Ring Surrounding HD 142527". In: *Publications of the Astronomical Society of Japan* 65, L14, p. L14. DOI: 10.1093/pasj/65.6.L14. arXiv: 1309.7400 [astro-ph.SR].

Gaia Collaboration et al. (Aug. 2018). "Gaia Data Release 2. The celestial reference frame (Gaia-CRF2)". In: *Astronomy and Astrophysics* 616, A14, A14. DOI: 10.1051/0004-6361/201832916.

Gammie, Charles F., Stuart L. Shapiro, and Jonathan C. McKinney (Feb. 2004). "Black Hole Spin Evolution". In: *The Astrophysical Journal* 602(1), pp. 312–319. DOI: 10.1086/380996. arXiv: astro-ph/0310886 [astro-ph].

Garufi, A. et al. (Dec. 2013). "Small vs. large dust grains in transitional disks: do different cavity sizes indicate a planet?. SAO 206462 (HD 135344B) in polarized light with VLT/NACO". In: *Astronomy and Astrophysics* 560, A105, A105. DOI: 10.1051/0004-6361/201322429. arXiv: 1311.4195 [astro-ph.EP].

Girart, J. M. et al. (Apr. 2018). "Resolving the Polarized Dust Emission of the Disk around the Massive Star Powering the HH 80-81 Radio Jet". In: *The Astrophysical Journal Letters* 856(2), L27, p. L27. DOI: 10.3847/2041-8213/aab76b. arXiv: 1803.06165 [astro-ph.SR].

Gold, T. (Jan. 1952). "The alignment of galactic dust". In: *Monthly Notice of Royal Astronomical Society* 112, p. 215. DOI: 10.1093/mnras/112.2.215.

Goldreich, Peter and William R. Ward (Aug. 1973). "The Formation of Planetesimals". In: *The Astrophysical Journal* 183, pp. 1051–1062. DOI: 10.1086/152291.

Gorti, U., C. P. Dullemond, and D. Hollenbach (Nov. 2009). "Time Evolution of Viscous Circumstellar Disks due to Photoevaporation by Far-Ultraviolet, Extreme-Ultraviolet, and X-ray Radiation from the Central Star". In: *The Astrophysical Journal* 705(2), pp. 1237–1251. DOI: 10.1088/0004-637X/705/2/1237. arXiv: 0909.1836 [astro-ph.SR].

Gorti, U. and D. Hollenbach (Jan. 2009). "Photoevaporation of Circumstellar Disks By Far-Ultraviolet, Extreme-Ultraviolet and X-Ray Radiation from the Central Star". In: *The Astrophysical Journal* 690(2), pp. 1539–1552. DOI: 10.1088/0004-637X/690/2/1539. arXiv: 0809.1494 [astro-ph].

Grady, C. A. et al. (Jan. 2013). "Spiral Arms in the Asymmetrically Illuminated Disk of MWC 758 and Constraints on Giant Planets". In: *The Astrophysical Journal* 762(1), 48, p. 48. DOI: 10.1088/0004-637X/762/1/48. arXiv: 1212.1466 [astro-ph.SR].

Greene, Thomas P. et al. (Oct. 1994). "Further Mid-Infrared Study of the rho Ophiuchi Cloud Young Stellar Population: Luminosities and Masses of Pre–Main-Sequence Stars". In: *The Astrophysical Journal* 434, p. 614. DOI: 10.1086/174763.

Guilloteau, S. et al. (May 2011). "A dual-frequency sub-arcsecond study of proto-planetary disks at mm wavelengths: first evidence for radial variations of the dust properties". In: *Astronomy and Astrophysics* 529, A105, A105. DOI: 10.1051/0004-6361/201015209. arXiv: 1103.1296 [astro-ph.GA].

Gutermuth, R. A. et al. (Feb. 2008). "Spitzer Observations of NGC 1333: A Study of Structure and Evolution in a Nearby Embedded Cluster". In: *The Astrophysical Journal* 674(1), pp. 336–356. DOI: 10.1086/524722. arXiv: 0710.1860 [astro-ph].

Güttler, C. et al. (Apr. 2010). "The outcome of protoplanetary dust growth: pebbles, boulders, or planetesimals?. I. Mapping the zoo of laboratory collision experiments". In: *Astronomy and Astrophysics* 513, A56, A56. DOI: 10.1051/0004-6361/200912852. arXiv: 0910.4251 [astro-ph.EP].

Guzmán, Viviana V. et al. (Dec. 2018). "The Disk Substructures at High Angular Resolution Program (DSHARP). VIII. The Rich Ringed Substructures in the AS 209 Disk". In: *The Astrophysical Journal Letters* 869(2), L48, p. L48. DOI: 10.3847/2041-8213/aaedae. arXiv: 1812.04046 [astro-ph.SR].

Haisch Karl E., Jr., Elizabeth A. Lada, and Charles J. Lada (June 2001). "Disk Frequencies and Lifetimes in Young Clusters". In: *The Astrophysical Journal Letters* 553(2), pp. L153–L156. DOI: 10.1086/320685. arXiv: astro-ph/0104347 [astro-ph].

Harris, Robert J. et al. (July 2018). "ALMA Observations of Polarized 872 μm Dust Emission from the Protostellar Systems VLA 1623 and L1527". In: *The Astrophysical Journal* 861(2), 91, p. 91. DOI: 10.3847/1538-4357/aac6ec. arXiv: 1805.08792 [astro-ph.SR].

Harrison, Rachel E. et al. (May 2019). "Dust Polarization in Four Protoplanetary Disks at 3 mm: Further Evidence of Multiple Origins". In: *The Astrophysical Journal Letters* 877(1), L2, p. L2. DOI: 10.3847/2041-8213/ab1e46. arXiv: 1905.06266 [astro-ph.SR].

Hartmann, Lee et al. (Mar. 1998). "Accretion and the Evolution of T Tauri Disks". In: *The Astrophysical Journal* 495(1), pp. 385–400. DOI: 10.1086/305277.

Hayashi, C. (Jan. 1981). "Formation of the planets". In: *Fundamental Problems in the Theory of Stellar Evolution*. Ed. by D. Sugimoto, D. Q. Lamb, and D. N. Schramm. Vol. 93. IAU Symposium, pp. 113–126.

Henning, T. and R. Stognienko (July 1996). "Dust opacities for protoplanetary accretion disks: influence of dust aggregates." In: *Astronomy and Astrophysics* 311, pp. 291–303.

Hernández, Jesús et al. (Dec. 2007). "Spitzer Observations of the Orion OB1 Association: Disk Census in the Low-Mass Stars". In: *The Astrophysical*

Journal 671(2), pp. 1784–1799. DOI: 10.1086/522882. arXiv: 0709.0912 [astro-ph].

Hillenbrand, Lynne A. (Nov. 2005). "Observational Constraints on Dust Disk Lifetimes: Implications for Planet Formation". In: *arXiv e-prints*, astro-ph/0511083, astro–ph/0511083. arXiv: astro-ph/0511083 [astro-ph].

Hiltner, W. A. (Feb. 1949). "Polarization of Radiation from Distant Stars by the Interstellar Medium". In: *Nature* 163(4138), p. 283. DOI: 10.1038/163283a0.

Hoang, Thiem, Jungyeon Cho, and A. Lazarian (Jan. 2018). "Alignment of Irregular Grains by Mechanical Torques". In: *The Astrophysical Journal* 852(2), 129, p. 129. DOI: 10.3847/1538-4357/aa9edc. arXiv: 1704.02256 [astro-ph.GA].

Hoang, Thiem and A. Lazarian (July 2008). "Radiative torque alignment: essential physical processes". In: *Monthly Notice of Royal Astronomical Society* 388(1), pp. 117–143. DOI: 10.1111/j.1365-2966.2008.13249.x. arXiv: 0707.3645 [astro-ph].

Hollenbach, David et al. (June 1994). "Photoevaporation of Disks around Massive Stars and Application to Ultracompact H II Regions". In: *The Astrophysical Journal* 428, p. 654. DOI: 10.1086/174276.

Huang, Jane et al. (Jan. 2018a). "CO and Dust Properties in the TW Hya Disk from High-resolution ALMA Observations". In: *The Astrophysical Journal* 852(2), 122, p. 122. DOI: 10.3847/1538-4357/aaa1e7. arXiv: 1801.03948 [astro-ph.SR].

Huang, Jane et al. (Dec. 2018b). "The Disk Substructures at High Angular Resolution Project (DSHARP). II. Characteristics of Annular Substructures". In: *The Astrophysical Journal Letters* 869(2), L42, p. L42. DOI: 10.3847/2041-8213/aaf740. arXiv: 1812.04041 [astro-ph.EP].

Hughes, A. Meredith et al. (Oct. 2009). "Stringent Limits on the Polarized Submillimeter Emission from Protoplanetary Disks". In: *The Astrophysical Journal* 704(2), pp. 1204–1217. DOI: 10.1088/0004-637X/704/2/1204. arXiv: 0909.1345 [astro-ph.SR].

Hughes, A. Meredith et al. (Apr. 2013). "Interferometric Upper Limits on Millimeter Polarization of the Disks around DG Tau, GM Aur, and MWC 480". In: *The Astronomical Journal* 145(4), 115, p. 115. DOI: 10.1088/0004-6256/145/4/115. arXiv: 1302.4745 [astro-ph.SR].

Hull, Charles L. H. and Richard L. Plambeck (June 2015). "The 1.3mm Full-Stokes Polarization System at CARMA". In: *Journal of Astronomical Instrumentation* 4, 1550005, p. 1550005. DOI: 10.1142/S2251171715500051. arXiv: 1506.04771 [astro-ph.IM].

Hull, Charles L. H. et al. (June 2018). "ALMA Observations of Polarization from Dust Scattering in the IM Lup Protoplanetary Disk". In: *The Astrophysical Journal* 860(1), 82, p. 82. DOI: 10.3847/1538-4357/aabfeb. arXiv: 1804.06269 [astro-ph.SR].

Isella, Andrea, John M. Carpenter, and Anneila I. Sargent (Aug. 2009). "Structure and Evolution of Pre-main-sequence Circumstellar Disks". In: *The Astrophysical Journal* 701(1), pp. 260–282. DOI: 10.1088/0004-637X/701/1/260. arXiv: 0906.2227 [astro-ph.SR].

Isella, Andrea, John M. Carpenter, and Anneila I. Sargent (May 2010). "Investigating Planet Formation in Circumstellar Disks: CARMA Observations of Ry Tau and Dg Tau". In: *The Astrophysical Journal* 714(2), pp. 1746–1761. DOI: 10.1088/0004-637X/714/2/1746. arXiv: 1003.4318 [astro-ph.SR].

Isella, Andrea et al. (Dec. 2010). "Millimeter Imaging of MWC 758: Probing the Disk Structure and Kinematics". In: *The Astrophysical Journal* 725(2), pp. 1735–1741. DOI: 10.1088/0004-637X/725/2/1735. arXiv: 1010.3016 [astro-ph.SR].

Isella, Andrea et al. (Dec. 2016). "Ringed Structures of the HD 163296 Protoplanetary Disk Revealed by ALMA". In: *Physical Review Letters* 117(25), 251101, p. 251101. DOI: 10.1103/PhysRevLett.117.251101.

Jin, Sheng et al. (Feb. 2016). "Modeling Dust Emission of HL Tau Disk Based on Planet-Disk Interactions". In: *The Astrophysical Journal* 818(1), 76, p. 76. DOI: 10.3847/0004-637X/818/1/76. arXiv: 1601.00358 [astro-ph.EP].

Johansen, A., A. Youdin, and H. Klahr (June 2009). "Zonal Flows and Long-lived Axisymmetric Pressure Bumps in Magnetorotational Turbulence". In: *The Astrophysical Journal* 697(2), pp. 1269–1289. DOI: 10.1088/0004-637X/697/2/1269. arXiv: 0811.3937 [astro-ph].

Johansen, Anders et al. (Aug. 2007). "Rapid planetesimal formation in turbulent circumstellar disks". In: *Nature* 448(7157), pp. 1022–1025. DOI: 10.1038/nature06086. arXiv: 0708.3890 [astro-ph].

Kanagawa, Kazuhiro D. et al. (June 2015). "Mass Estimates of a Giant Planet in a Protoplanetary Disk from the Gap Structures". In: *The Astrophysical Journal Letters* 806(1), L15, p. L15. DOI: 10.1088/2041-8205/806/1/L15. arXiv: 1505.04482 [astro-ph.EP].

Kanagawa, Kazuhiro D. et al. (June 2016). "Mass constraint for a planet in a protoplanetary disk from the gap width". In: *Publications of the Astronomical Society of Japan* 68(3), 43, p. 43. DOI: 10.1093/pasj/psw037. arXiv: 1603.03853 [astro-ph.EP].

Kataoka, Akimasa, Satoshi Okuzumi, and Ryo Tazaki (Mar. 2019). "Millimeter-wave Polarization Due to Grain Alignment by the Gas Flow in Protoplanetary Disks". In: *The Astrophysical Journal Letters* 874(1), L6, p. L6. DOI: 10.3847/2041-8213/ab0c9a. arXiv: 1903.03529 [astro-ph.EP].

Kataoka, Akimasa et al. (Aug. 2015). "Millimeter-wave Polarization of Protoplanetary Disks due to Dust Scattering". In: *The Astrophysical Journal* 809(1), 78, p. 78. DOI: 10.1088/0004-637X/809/1/78. arXiv: 1504.04812 [astro-ph.EP].

Kataoka, Akimasa et al. (Mar. 2016a). "Grain Size Constraints on HL Tau with Polarization Signature". In: *The Astrophysical Journal* 820(1), 54, p. 54. DOI: 10.3847/0004-637X/820/1/54. arXiv: 1507.08902 [astro-ph.EP].

Kataoka, Akimasa et al. (Nov. 2016b). "Submillimeter Polarization Observation of the Protoplanetary Disk around HD 142527". In: *The Astrophysical Journal Letters* 831(2), L12, p. L12. DOI: 10.3847/2041-8205/831/2/L12. arXiv: 1610.06318 [astro-ph.EP].

Kataoka, Akimasa et al. (July 2017). "The Evidence of Radio Polarization Induced by the Radiative Grain Alignment and Self-scattering of Dust

Grains in a Protoplanetary Disk". In: *The Astrophysical Journal Letters* 844(1), L5, p. L5. DOI: 10.3847/2041-8213/aa7e33. arXiv: 1707.01612 [astro-ph.EP].

Kirchschlager, Florian, Gesa H. M. Bertrang, and Mario Flock (Sept. 2019). "Intrinsic polarization of elongated porous dust grains". In: *Monthly Notice of Royal Astronomical Society* 488(1), pp. 1211–1219. DOI: 10.1093/mnras/stz1763. arXiv: 1906.10699 [astro-ph.EP].

Kitamura, Yoshimi et al. (Dec. 2002). "Investigation of the Physical Properties of Protoplanetary Disks around T Tauri Stars by a 1 Arcsecond Imaging Survey: Evolution and Diversity of the Disks in Their Accretion Stage". In: *The Astrophysical Journal* 581(1), pp. 357–380. DOI: 10.1086/344223.

Klahr, H. Hubertus and Thomas Henning (July 1997). "Particle-Trapping Eddies in Protoplanetary Accretion Disks". In: *Icarus* 128(1), pp. 213–229. DOI: 10.1006/icar.1997.5720.

Kudoh, Takahiro and Kazunari Shibata (Feb. 1997). "Magnetically Driven Jets from Accretion Disks. II. Nonsteady Solutions and Comparison with Steady Solutions". In: *The Astrophysical Journal* 476(2), pp. 632–648. DOI: 10.1086/303635.

Kusaka, T., T. Nakano, and C. Hayashi (Dec. 1970). "Growth of Solid Particles in the Primordial Solar Nebula". In: *Progress of Theoretical Physics* 44(6), pp. 1580–1595. DOI: 10.1143/PTP.44.1580.

Kwon, Woojin, Leslie W. Looney, and Lee G. Mundy (Nov. 2011). "Resolving the Circumstellar Disk of HL Tauri at Millimeter Wavelengths". In: *The Astrophysical Journal* 741(1), 3, p. 3. DOI: 10.1088/0004-637X/741/1/3. arXiv: 1107.5275 [astro-ph.SR].

Lada, C. J., M. Margulis, and D. Dearborn (Oct. 1984). "The formation and early dynamical evolution of bound stellar systems." In: *The Astrophysical Journal* 285, pp. 141–152. DOI: 10.1086/162485.

Lada, Charles J. et al. (Mar. 2006). "Spitzer Observations of IC 348: The Disk Population at 2-3 Million Years". In: *The Astronomical Journal* 131(3), pp. 1574–1607. DOI: 10.1086/499808. arXiv: astro-ph/0511638 [astro-ph].

Larson, Richard B. (Jan. 1969). "Numerical calculations of the dynamics of collapsing proto-star". In: *Monthly Notice of Royal Astronomical Society* 145, p. 271. DOI: 10.1093/mnras/145.3.271.

Lay, O. P., J. E. Carlstrom, and R. E. Hills (Nov. 1997). "Constraints on the HL Tauri Protostellar Disk from Millimeter- and Submillimeter-Wave Interferometry". In: *The Astrophysical Journal* 489(2), pp. 917–927. DOI: 10.1086/304815.

Lazarian, A. and B. T. Draine (July 1999). "Nuclear Spin Relaxation within Interstellar Grains". In: *The Astrophysical Journal Letters* 520(1), pp. L67–L70. DOI: 10.1086/312137. arXiv: astro-ph/9903235 [astro-ph].

Lazarian, A. and Michael Efroimsky (Mar. 1999). "Inelastic dissipation in a freely rotating body: application to cosmic dust alignment". In: *Monthly Notice of Royal Astronomical Society* 303(4), pp. 673–684. DOI: 10.1046/j.1365-8711.1999.02235.x. arXiv: astro-ph/9811040 [astro-ph].

Lazarian, A. and Thiem Hoang (Nov. 2007). "Subsonic Mechanical Alignment of Irregular Grains". In: *The Astrophysical Journal Letters* 669(2), pp. L77–L80. DOI: 10.1086/523849. arXiv: 0707.3805 [astro-ph].

Lee, Chin-Fei et al. (Feb. 2018). "ALMA Dust Polarization Observations of Two Young Edge-on Protostellar Disks". In: *The Astrophysical Journal* 854(1), 56, p. 56. DOI: 10.3847/1538-4357/aaa769. arXiv: 1801.03802 [astro-ph.GA].

Lee, H. M. and B. T. Draine (Mar. 1985). "Infrared extinction and polarization due to partially aligned spheroidal grains : models for the dust toward the BN object." In: *The Astrophysical Journal* 290, pp. 211–228. DOI: 10.1086/162974.

Lee, Nicholas, Jonathan P. Williams, and Lucas A. Cieza (Aug. 2011). "Protoplanetary Disk Masses in IC348: A Rapid Decline in the Population of Small Dust Grains After 1 Myr". In: *The Astrophysical Journal* 736(2), 135, p. 135. DOI: 10.1088/0004-637X/736/2/135. arXiv: 1105.2046 [astro-ph.SR].

Li, Aigen and B. T. Draine (June 2001). "Infrared Emission from Interstellar Dust. II. The Diffuse Interstellar Medium". In: *The Astrophysical Journal* 554(2), pp. 778–802. DOI: 10.1086/323147. arXiv: astro-ph/0011319 [astro-ph].

Li, Dan et al. (Nov. 2016). "An Ordered Magnetic Field in the Protoplanetary Disk of AB Aur Revealed by Mid-infrared Polarimetry". In: *The Astrophysical Journal* 832(1), 18, p. 18. DOI: 10.3847/0004-637X/832/1/18. arXiv: 1609.02493 [astro-ph.EP].

Lin, D. N. C. and J. Papaloizou (Apr. 1980). "On the structure and evolution of the primordial solar nebula". In: *Monthly Notice of Royal Astronomical Society* 191, pp. 37–48. DOI: 10.1093/mnras/191.1.37.

Liu, Hauyu Baobab (June 2019). "The Anomalously Low (Sub)Millimeter Spectral Indices of Some Protoplanetary Disks May Be Explained By Dust Self-scattering". In: *The Astrophysical Journal Letters* 877(2), L22, p. L22. DOI: 10.3847/2041-8213/ab1f8e. arXiv: 1904.00333 [astro-ph.SR].

Liu, Yao et al. (Nov. 2017). "The properties of the inner disk around HL Tau: Multi-wavelength modeling of the dust emission". In: *Astronomy and Astrophysics* 607, A74, A74. DOI: 10.1051/0004-6361/201629786. arXiv: 1708.03238 [astro-ph.EP].

Long, Feng et al. (Dec. 2018). "Gaps and Rings in an ALMA Survey of Disks in the Taurus Star-forming Region". In: *The Astrophysical Journal* 869(1), 17, p. 17. DOI: 10.3847/1538-4357/aae8e1. arXiv: 1810.06044 [astro-ph.SR].

Looney, Leslie W., Lee G. Mundy, and W. J. Welch (Jan. 2000). "Unveiling the Circumstellar Envelope and Disk: A Subarcsecond Survey of Circumstellar Structures". In: *The Astrophysical Journal* 529(1), pp. 477–498. DOI: 10.1086/308239. arXiv: astro-ph/9908301 [astro-ph].

Luhman, K. L. and G. H. Rieke (Nov. 1999). "Low-Mass Star Formation and the Initial Mass Function in the ρ Ophiuchi Cloud Core". In: *The Astrophysical Journal* 525(1), pp. 440–465. DOI: 10.1086/307891. arXiv: astro-ph/9905286 [astro-ph].

Lumbreras, Alba M. and Luis A. Zapata (Apr. 2014). "SMA Submillimeter Observations of HL Tau: Revealing a Compact Molecular Outflow". In: *The Astronomical Journal* 147(4), 72, p. 72. DOI: 10.1088/0004-6256/147/4/72. arXiv: 1401.0455 [astro-ph.GA].

Lynden-Bell, D. and J. E. Pringle (Sept. 1974). "The evolution of viscous discs and the origin of the nebular variables." In: *Monthly Notice of Royal Astronomical Society* 168, pp. 603–637. DOI: 10.1093/mnras/168.3.603.

Lyra, Wladimir and Min-Kai Lin (Sept. 2013). "Steady State Dust Distributions in Disk Vortices: Observational Predictions and Applications to Transitional Disks". In: *The Astrophysical Journal* 775(1), 17, p. 17. DOI: 10.1088/0004-637X/775/1/17. arXiv: 1307.3770 [astro-ph.EP].

Mannings, Vincent and James P. Emerson (Mar. 1994). "Dust in discs around T Tauri stars : grain growth ?" In: *Monthly Notice of Royal Astronomical Society* 267, pp. 361–378. DOI: 10.1093/mnras/267.2.361.

Mathis, J. S., W. Rumpl, and K. H. Nordsieck (Oct. 1977). "The size distribution of interstellar grains." In: *The Astrophysical Journal* 217, pp. 425–433. DOI: 10.1086/155591.

McMullin, J. P. et al. (Oct. 2007). "CASA Architecture and Applications". In: *Astronomical Data Analysis Software and Systems XVI*. Ed. by R. A. Shaw, F. Hill, and D. J. Bell. Vol. 376. Astronomical Society of the Pacific Conference Series, p. 127.

Min, M., J. W. Hovenier, and A. de Koter (Mar. 2005). "Modeling optical properties of cosmic dust grains using a distribution of hollow spheres". In: *Astronomy and Astrophysics* 432(3), pp. 909–920. DOI: 10.1051/0004-6361:20041920. arXiv: astro-ph/0503068 [astro-ph].

Miotello, A. et al. (Oct. 2016). "Determining protoplanetary disk gas masses from CO isotopologues line observations". In: *Astronomy and Astrophysics* 594, A85, A85. DOI: 10.1051/0004-6361/201628159. arXiv: 1605.07780 [astro-ph.SR].

Miotello, A. et al. (Mar. 2017). "Lupus disks with faint CO isotopologues: low gas/dust or high carbon depletion?" In: *Astronomy and Astrophysics* 599, A113, A113. DOI: 10.1051/0004-6361/201629556. arXiv: 1612.01538 [astro-ph.SR].

Miotello, A. et al. (Nov. 2018). "Probing the protoplanetary disk gas surface density distribution with ^{13}CO emission". In: *Astronomy and Astrophysics* 619, A113, A113. DOI: 10.1051/0004-6361/201833595. arXiv: 1809.00482 [astro-ph.SR].

Mittal, Tushar and Eugene Chiang (Jan. 2015). "Fast Modes and Dusty Horseshoes in Transitional Disks". In: *The Astrophysical Journal Letters* 798(1), L25, p. L25. DOI: 10.1088/2041-8205/798/1/L25. arXiv: 1412.2135 [astro-ph.EP].

Miyake, Kotaro and Yoshitsugu Nakagawa (Nov. 1993). "Effects of Particle Size Distribution on Opacity Curves of Protoplanetary Disks around T Tauri Stars". In: *Icarus* 106(1), pp. 20–41. DOI: 10.1006/icar.1993.1156.

Mundy, Lee G. et al. (June 1996). "Imaging the HL Tauri Disk at lambda = 2.7 Millimeters with the BIMA Array". In: *The Astrophysical Journal Letters* 464, p. L169. DOI: 10.1086/310117.

Muto, T. et al. (Apr. 2012). "Discovery of Small-scale Spiral Structures in the Disk of SAO 206462 (HD 135344B): Implications for the Physical State of the Disk from Spiral Density Wave Theory". In: *The Astrophysical Journal*

Letters 748(2), L22, p. L22. DOI: 10.1088/2041-8205/748/2/L22. arXiv: 1202.6139 [astro-ph.EP].

Muzerolle, James et al. (Jan. 2010). "A Spitzer Census of Transitional Protoplanetary Disks with AU-scale Inner Holes". In: *The Astrophysical Journal* 708(2), pp. 1107–1118. DOI: 10.1088/0004-637X/708/2/1107. arXiv: 0911.2704 [astro-ph.SR].

Nagai, H. et al. (June 2016). "ALMA Science Verification Data: Millimeter Continuum Polarimetry of the Bright Radio Quasar 3C 286". In: *The Astrophysical Journal* 824(2), 132, p. 132. DOI: 10.3847/0004-637X/824/2/132. arXiv: 1605.00051 [astro-ph.GA].

Natta, A., L. Testi, and S. Randich (June 2006). "Accretion in the ρ-Ophiuchi pre-main sequence stars". In: *Astronomy and Astrophysics* 452(1), pp. 245–252. DOI: 10.1051/0004-6361:20054706. arXiv: astro-ph/0602618 [astro-ph].

Natta, A. et al. (Mar. 2004). "A search for evolved dust in Herbig Ae stars". In: *Astronomy and Astrophysics* 416, pp. 179–186. DOI: 10.1051/0004-6361:20035620. arXiv: astro-ph/0311624 [astro-ph].

Natta, A. et al. (Jan. 2007). "Dust in Protoplanetary Disks: Properties and Evolution". In: *Protostars and Planets V*. Ed. by Bo Reipurth, David Jewitt, and Klaus Keil, p. 767. arXiv: astro-ph/0602041 [astro-ph].

Öberg, Karin I. et al. (Dec. 2011). "The Ionization Fraction in the DM Tau Protoplanetary Disk". In: *The Astrophysical Journal* 743(2), 152, p. 152. DOI: 10.1088/0004-637X/743/2/152. arXiv: 1109.2578 [astro-ph.GA].

Ohashi, Satoshi and Akimasa Kataoka (Oct. 2019). "Radial variations in grain sizes and dust scale heights in the protoplanetary disk around HD 163296 revealed by ALMA polarization observation". In: *arXiv e-prints*, arXiv:1910.12868, arXiv:1910.12868. arXiv: 1910.12868 [astro-ph.EP].

Ohashi, Satoshi et al. (Sept. 2018). "Two Different Grain Size Distributions within the Protoplanetary Disk around HD 142527 Revealed by ALMA Polarization Observation". In: *The Astrophysical Journal* 864(1), 81, p. 81. DOI: 10.3847/1538-4357/aad632. arXiv: 1807.10776 [astro-ph.EP].

Okuzumi, Satoshi (June 2009). "Electric Charging of Dust Aggregates and its Effect on Dust Coagulation in Protoplanetary Disks". In: *The Astrophysical Journal* 698(2), pp. 1122–1135. DOI: 10.1088/0004-637X/698/2/1122. arXiv: 0901.2886 [astro-ph.EP].

Okuzumi, Satoshi and Ryo Tazaki (June 2019). "Nonsticky Ice at the Origin of the Uniformly Polarized Submillimeter Emission from the HL Tau Disk". In: *The Astrophysical Journal* 878(2), 132, p. 132. DOI: 10.3847/1538-4357/ab204d. arXiv: 1904.03869 [astro-ph.EP].

Okuzumi, Satoshi et al. (Apr. 2011a). "Electrostatic Barrier Against Dust Growth in Protoplanetary Disks. I. Classifying the Evolution of Size Distribution". In: *The Astrophysical Journal* 731(2), 95, p. 95. DOI: 10.1088/0004-637X/731/2/95. arXiv: 1009.3199 [astro-ph.EP].

Okuzumi, Satoshi et al. (Apr. 2011b). "Electrostatic Barrier Against Dust Growth in Protoplanetary Disks. II. Measuring the Size of the "Frozen" Zone". In: *The Astrophysical Journal* 731(2), 96, p. 96. DOI: 10.1088/0004-637X/731/2/96. arXiv: 1009.3101 [astro-ph.EP].

Okuzumi, Satoshi et al. (June 2012). "Rapid Coagulation of Porous Dust Aggregates outside the Snow Line: A Pathway to Successful Icy Planetesimal Formation". In: *The Astrophysical Journal* 752(2), 106, p. 106. DOI: 10.1088/0004-637X/752/2/106. arXiv: 1204.5035 [astro-ph.EP].

Owen, J. E. et al. (Jan. 2010). "Radiation-hydrodynamic models of X-ray and EUV photoevaporating protoplanetary discs". In: *Monthly Notice of Royal Astronomical Society* 401(3), pp. 1415–1428. DOI: 10.1111/j.1365-2966.2009.15771.x. arXiv: 0909.4309 [astro-ph.SR].

Pattle, Kate et al. (Sept. 2017). "The JCMT BISTRO Survey: The Magnetic Field Strength in the Orion A Filament". In: *The Astrophysical Journal* 846(2), 122, p. 122. DOI: 10.3847/1538-4357/aa80e5. arXiv: 1707.05269 [astro-ph.GA].

Pérez, Laura M. et al. (Nov. 2012). "Constraints on the Radial Variation of Grain Growth in the AS 209 Circumstellar Disk". In: *The Astrophysical Journal Letters* 760(1), L17, p. L17. DOI: 10.1088/2041-8205/760/1/L17. arXiv: 1210.5252 [astro-ph.SR].

Pérez, Laura M. et al. (Mar. 2014). "Large-scale Asymmetries in the Transitional Disks of SAO 206462 and SR 21". In: *The Astrophysical Journal Letters* 783(1), L13, p. L13. DOI: 10.1088/2041-8205/783/1/L13. arXiv: 1402.0832 [astro-ph.SR].

Pérez, Laura M. et al. (Sept. 2016). "Spiral density waves in a young protoplanetary disk". In: *Science* 353(6307), pp. 1519–1521. DOI: 10.1126/science.aaf8296. arXiv: 1610.05139 [astro-ph.GA].

Piétu, V. et al. (Dec. 2006). "Resolving the inner dust disks surrounding LkCa 15 and MWC 480 at mm wavelengths". In: *Astronomy and Astrophysics* 460(3), pp. L43–L47. DOI: 10.1051/0004-6361:20065968. arXiv: astro-ph/0610200 [astro-ph].

Piétu, V. et al. (Apr. 2014). "Faint disks around classical T Tauri stars: Small but dense enough to form planets". In: *Astronomy and Astrophysics* 564, A95, A95. DOI: 10.1051/0004-6361/201322388. arXiv: 1402.5312 [astro-ph.EP].

Pinilla, P., M. Benisty, and T. Birnstiel (Sept. 2012). "Ring shaped dust accumulation in transition disks". In: *Astronomy and Astrophysics* 545, A81, A81. DOI: 10.1051/0004-6361/201219315. arXiv: 1207.6485 [astro-ph.EP].

Pinte, C. et al. (Jan. 2016). "Dust and Gas in the Disk of HL Tauri: Surface Density, Dust Settling, and Dust-to-gas Ratio". In: *The Astrophysical Journal* 816(1), 25, p. 25. DOI: 10.3847/0004-637X/816/1/25. arXiv: 1508.00584 [astro-ph.SR].

Planck Collaboration et al. (Apr. 2015). "Planck intermediate results. XIX. An overview of the polarized thermal emission from Galactic dust". In: *Astronomy and Astrophysics* 576, A104, A104. DOI: 10.1051/0004-6361/201424082. arXiv: 1405.0871 [astro-ph.GA].

Planck Collaboration et al. (Dec. 2016). "Planck intermediate results. XLIV. Structure of the Galactic magnetic field from dust polarization maps of the southern Galactic cap". In: *Astronomy and Astrophysics* 596, A105, A105. DOI: 10.1051/0004-6361/201628636. arXiv: 1604.01029 [astro-ph.GA].

Pohl, A. et al. (Aug. 2016). "Investigating dust trapping in transition disks with millimeter-wave polarization". In: *Astronomy and Astrophysics* 593,

A12, A12. DOI: 10.1051/0004-6361/201628637. arXiv: 1607.00387 [astro-ph.EP].

Pollack, James B. et al. (Feb. 1994). "Composition and Radiative Properties of Grains in Molecular Clouds and Accretion Disks". In: *The Astrophysical Journal* 421, p. 615. DOI: 10.1086/173677.

Purcell, E. M. (July 1979). "Suprathermal rotation of interstellar grains." In: *The Astrophysical Journal* 231, pp. 404–416. DOI: 10.1086/157204.

Rebull, L. M., S. C. Wolff, and S. E. Strom (Feb. 2004). "Stellar Rotation in Young Clusters: The First 4 Million Years". In: *The Astronomical Journal* 127(2), pp. 1029–1051. DOI: 10.1086/380931.

Regály, Zs. et al. (Jan. 2012). "Possible planet-forming regions on submillimetre images". In: *Monthly Notice of Royal Astronomical Society* 419(2), pp. 1701–1712. DOI: 10.1111/j.1365-2966.2011.19834.x. arXiv: 1109.6177 [astro-ph.SR].

Ricci, L. et al. (Mar. 2010). "Dust properties of protoplanetary disks in the Taurus-Auriga star forming region from millimeter wavelengths". In: *Astronomy and Astrophysics* 512, A15, A15. DOI: 10.1051/0004-6361/200913403. arXiv: 0912.3356 [astro-ph.EP].

Ricci, L. et al. (Apr. 2012). "The effect of local optically thick regions in the long-wave emission of young circumstellar disks". In: *Astronomy and Astrophysics* 540, A6, A6. DOI: 10.1051/0004-6361/201118296. arXiv: 1202.1802 [astro-ph.GA].

Robitaille, Thomas P. et al. (Apr. 2007). "Interpreting Spectral Energy Distributions from Young Stellar Objects. II. Fitting Observed SEDs Using a Large Grid of Precomputed Models". In: *The Astrophysical Journal Supplement Series* 169(2), pp. 328–352. DOI: 10.1086/512039. arXiv: astro-ph/0612690 [astro-ph].

Rodmann, J. et al. (Jan. 2006). "Large dust particles in disks around T Tauri stars". In: *Astronomy and Astrophysics* 446(1), pp. 211–221. DOI: 10.1051/0004-6361:20054038. arXiv: astro-ph/0509555 [astro-ph].

Rosenfeld, Katherine A. et al. (Sept. 2013a). "A Spatially Resolved Vertical Temperature Gradient in the HD 163296 Disk". In: *The Astrophysical Journal* 774(1), 16, p. 16. DOI: 10.1088/0004-637X/774/1/16. arXiv: 1306.6475 [astro-ph.SR].

Rosenfeld, Katherine A. et al. (Oct. 2013b). "The Structure of the Evolved Circumbinary Disk around V4046 Sgr". In: *The Astrophysical Journal* 775(2), 136, p. 136. DOI: 10.1088/0004-637X/775/2/136. arXiv: 1308.4358 [astro-ph.SR].

Ruden, S. P. and D. N. C. Lin (Sept. 1986). "The Global Evolution of the Primordial Solar Nebula". In: *The Astrophysical Journal* 308, p. 883. DOI: 10.1086/164559.

Ruden, Steven P. and James B. Pollack (July 1991). "The Dynamical Evolution of the Protosolar Nebula". In: *The Astrophysical Journal* 375, p. 740. DOI: 10.1086/170239.

Sadavoy, Sarah I. et al. (June 2018a). "Dust Polarization toward Embedded Protostars in Ophiuchus with ALMA. I. VLA 1623". In: *The Astrophysical*

Journal 859(2), 165, p. 165. DOI: 10.3847/1538-4357/aac21a. arXiv: 1804.05968 [astro-ph.SR].

Sadavoy, Sarah I. et al. (Dec. 2018b). "Dust Polarization toward Embedded Protostars in Ophiuchus with ALMA. II. IRAS 16293-2422". In: *The Astrophysical Journal* 869(2), 115, p. 115. DOI: 10.3847/1538-4357/aaef81. arXiv: 1811.03104 [astro-ph.GA].

Sargent, A. I. and S. V. W. Beckwith (Nov. 1991). "The Molecular Structure around HL Tauri". In: *The Astrophysical Journal Letters* 382, p. L31. DOI: 10.1086/186207.

Shakura, N. I. and R. A. Sunyaev (June 1973). "Reprint of 1973A&A....24..337S. Black holes in binary systems. Observational appearance." In: *Astronomy and Astrophysics* 500, pp. 33–51.

Sicilia-Aguilar, Aurora et al. (Feb. 2006). "Disk Evolution in Cep OB2: Results from the Spitzer Space Telescope". In: *The Astrophysical Journal* 638(2), pp. 897–919. DOI: 10.1086/498085.

Simon, Jacob B. and Philip J. Armitage (Mar. 2014). "Efficiency of Particle Trapping in the Outer Regions of Protoplanetary Disks". In: *The Astrophysical Journal* 784(1), 15, p. 15. DOI: 10.1088/0004-637X/784/1/15. arXiv: 1402.1489 [astro-ph.SR].

Stephens, Ian W. et al. (Oct. 2014). "Spatially resolved magnetic field structure in the disk of a T Tauri star". In: *Nature* 514(7524), pp. 597–599. DOI: 10.1038/nature13850. arXiv: 1409.2878 [astro-ph.GA].

Stephens, Ian W. et al. (Dec. 2017). "ALMA Reveals Transition of Polarization Pattern with Wavelength in HL Tau's Disk". In: *The Astrophysical Journal* 851(1), 55, p. 55. DOI: 10.3847/1538-4357/aa998b. arXiv: 1710.04670 [astro-ph.SR].

Stepinski, Tomasz F. (Mar. 1998). "The Solar Nebula as a Process-An Analytic Model". In: *Icarus* 132(1), pp. 100–112. DOI: 10.1006/icar.1998.5893.

Strom, Karen M. et al. (May 1989). "Circumstellar Material Associated with Solar-Type Pre-Main-Sequence Stars: A Possible Constraint on the Timescale for Planet Building". In: *The Astronomical Journal* 97, p. 1451. DOI: 10.1086/115085.

Sung, Hwankyung, John R. Stauffer, and Michael S. Bessell (Oct. 2009). "A Spitzer View of the Young Open Cluster NGC 2264". In: *The Astronomical Journal* 138(4), pp. 1116–1136. DOI: 10.1088/0004-6256/138/4/1116. arXiv: 0906.3072 [astro-ph.SR].

Suzuki, Takeru K. and Shu-ichiro Inutsuka (Apr. 2014). "Magnetohydrodynamic Simulations of Global Accretion Disks with Vertical Magnetic Fields". In: *The Astrophysical Journal* 784(2), 121, p. 121. DOI: 10.1088/0004-637X/784/2/121. arXiv: 1309.6916 [astro-ph.EP].

Takahashi, Sanemichi Z. and Shu-ichiro Inutsuka (Oct. 2014). "Two-component Secular Gravitational Instability in a Protoplanetary Disk: A Possible Mechanism for Creating Ring-like Structures". In: *The Astrophysical Journal* 794(1), 55, p. 55. DOI: 10.1088/0004-637X/794/1/55. arXiv: 1312.6870 [astro-ph.EP].

Tamura, Motohide, J. H. Hough, and Saeko S. Hayashi (July 1995). "1 Millimeter Polarimetry of Young Stellar Objects: Low-Mass Protostars and T Tauri Stars". In: *The Astrophysical Journal* 448, p. 346. DOI: 10.1086/175965.

Tamura, Motohide et al. (Nov. 1999). "First Detection of Submillimeter Polarization from T Tauri Stars". In: *The Astrophysical Journal* 525(2), pp. 832–836. DOI: 10.1086/307953.

Tazaki, Ryo, Alexandre Lazarian, and Hideko Nomura (Apr. 2017). "Radiative Grain Alignment In Protoplanetary Disks: Implications for Polarimetric Observations". In: *The Astrophysical Journal* 839(1), 56, p. 56. DOI: 10.3847/1538-4357/839/1/56. arXiv: 1701.02063 [astro-ph.EP].

Tazzari, M. et al. (Apr. 2016). "Multiwavelength analysis for interferometric (sub-)mm observations of protoplanetary disks. Radial constraints on the dust properties and the disk structure". In: *Astronomy and Astrophysics* 588, A53, A53. DOI: 10.1051/0004-6361/201527423. arXiv: 1512.05679 [astro-ph.GA].

Testi, L. et al. (June 2001). "Constraints on Properties of the Protoplanetary Disks around UX Orionis and CQ Tauri". In: *The Astrophysical Journal* 554(2), pp. 1087–1094. DOI: 10.1086/321406. arXiv: astro-ph/0102473 [astro-ph].

Testi, L. et al. (May 2003). "Large grains in the disk of CQ Tau". In: *Astronomy and Astrophysics* 403, pp. 323–328. DOI: 10.1051/0004-6361:20030362. arXiv: astro-ph/0303420 [astro-ph].

Testi, L. et al. (Jan. 2014). "Dust Evolution in Protoplanetary Disks". In: *Protostars and Planets VI*. Ed. by Henrik Beuther et al., p. 339. DOI: 10.2458/azu_uapress_9780816531240-ch015. arXiv: 1402.1354 [astro-ph.SR].

Tominaga, Ryosuke T., Shu-ichiro Inutsuka, and Sanemichi Z. Takahashi (Jan. 2018). "Non-linear development of secular gravitational instability in protoplanetary disks". In: *Publications of the Astronomical Society of Japan* 70(1), 3, p. 3. DOI: 10.1093/pasj/psx143. arXiv: 1711.05948 [astro-ph.EP].

Tripathi, Anjali et al. (Aug. 2017). "A millimeter Continuum Size-Luminosity Relationship for Protoplanetary Disks". In: *The Astrophysical Journal* 845(1), 44, p. 44. DOI: 10.3847/1538-4357/aa7c62. arXiv: 1706.08977 [astro-ph.EP].

Tsukagoshi, Takashi et al. (Oct. 2016). "A Gap with a Deficit of Large Grains in the Protoplanetary Disk around TW Hya". In: *The Astrophysical Journal Letters* 829(2), L35, p. L35. DOI: 10.3847/2041-8205/829/2/L35. arXiv: 1605.00289 [astro-ph.SR].

Vaillancourt, John E. (Sept. 2006). "Placing Confidence Limits on Polarization Measurements". In: *Publications of the Astronomical Society of the Pacific* 118(847), pp. 1340–1343. DOI: 10.1086/507472. arXiv: astro-ph/0603110 [astro-ph].

van der Marel, Nienke et al. (June 2013). "A Major Asymmetric Dust Trap in a Transition Disk". In: *Science* 340(6137), pp. 1199–1202. DOI: 10.1126/science.1236770. arXiv: 1306.1768 [astro-ph.EP].

van Terwisga, S. E. et al. (Aug. 2018). "V1094 Scorpii: A rare giant multi-ringed disk around a T Tauri star". In: *Astronomy and Astrophysics* 616, A88, A88. DOI: 10.1051/0004-6361/201832862. arXiv: 1805.03221 [astro-ph.SR].

Wada, Koji et al. (Sept. 2009). "Collisional Growth Conditions for Dust Aggregates". In: *The Astrophysical Journal* 702(2), pp. 1490–1501. DOI: 10.1088/0004-637X/702/2/1490.

Wada, Koji et al. (Aug. 2011). "The Rebound Condition of Dust Aggregates Revealed by Numerical Simulation of Their Collisions". In: *The Astrophysical Journal* 737(1), 36, p. 36. DOI: 10.1088/0004-637X/737/1/36.

Warren, Stephen G. and Richard E. Brandt (July 2008). "Optical constants of ice from the ultraviolet to the microwave: A revised compilation". In: *Journal of Geophysical Research (Atmospheres)* 113(D14), D14220, p. D14220. DOI: 10.1029/2007JD009744.

Weidenschilling, S. J. (July 1977a). "Aerodynamics of solid bodies in the solar nebula." In: *Monthly Notice of Royal Astronomical Society* 180, pp. 57–70. DOI: 10.1093/mnras/180.1.57.

Weidenschilling, S. J. (Sept. 1977b). "The Distribution of Mass in the Planetary System and Solar Nebula". In: *Astrophysics and Space Science* 51(1), pp. 153–158. DOI: 10.1007/BF00642464.

Welch, Wm. J. et al. (Sept. 2000). "High-Resolution, Wide-Field Imaging of the HL Tauri Environment in ^{13}CO (1-0)". In: *The Astrophysical Journal* 540(1), pp. 362–371. DOI: 10.1086/309290.

Whipple, F. L. (Jan. 1972). "On certain aerodynamic processes for asteroids and comets". In: *From Plasma to Planet*. Ed. by Aina Elvius, p. 211.

White, Russel J. and Lynne A. Hillenbrand (Dec. 2004). "On the Evolutionary Status of Class I Stars and Herbig-Haro Energy Sources in Taurus-Auriga". In: *The Astrophysical Journal* 616(2), pp. 998–1032. DOI: 10.1086/425115. arXiv: astro-ph/0408244 [astro-ph].

Williams, Jonathan P. and William M. J. Best (June 2014). "A Parametric Modeling Approach to Measuring the Gas Masses of Circumstellar Disks". In: *The Astrophysical Journal* 788(1), 59, p. 59. DOI: 10.1088/0004-637X/788/1/59. arXiv: 1312.0151 [astro-ph.EP].

Williams, Jonathan P. et al. (Oct. 2013). "A SCUBA-2 850-μm survey of protoplanetary discs in the σ Orionis cluster". In: *Monthly Notice of Royal Astronomical Society* 435(2), pp. 1671–1679. DOI: 10.1093/mnras/stt1407. arXiv: 1307.7174 [astro-ph.GA].

Wilner, D. J. et al. (May 2000). "VLA Imaging of the Disk Surrounding the Nearby Young Star TW Hydrae". In: *The Astrophysical Journal Letters* 534(1), pp. L101–L104. DOI: 10.1086/312642. arXiv: astro-ph/0005019 [astro-ph].

Wilner, D. J. et al. (June 2005). "Toward Planetesimals in the Disk around TW Hydrae: 3.5 Centimeter Dust Emission". In: *The Astrophysical Journal Letters* 626(2), pp. L109–L112. DOI: 10.1086/431757. arXiv: astro-ph/0506644 [astro-ph].

Winston, E. et al. (Nov. 2007). "A Combined Spitzer and Chandra Survey of Young Stellar Objects in the Serpens Cloud Core". In: *The Astrophysical Journal* 669(1), pp. 493–518. DOI: 10.1086/521384. arXiv: 0707.2537 [astro-ph].

Wolf, Sebastian and H. Klahr (Oct. 2002). "Large-Scale Vortices in Protoplanetary Disks: On the Observability of Possible Early Stages of Planet Formation". In: *The Astrophysical Journal Letters* 578(1), pp. L79–L82. DOI: 10.1086/344501. arXiv: astro-ph/0209002 [astro-ph].

Wolk, Scott J. and Frederick M. Walter (May 1996). "A Search for Protoplanetary Disks Around Naked T Tauri Stars". In: *The Astronomical Journal* 111, p. 2066. DOI: 10.1086/117942.

Yang, Haifeng et al. (Mar. 2016). "Inclination-induced polarization of scattered millimetre radiation from protoplanetary discs: the case of HL Tau". In: *Monthly Notice of Royal Astronomical Society* 456(3), pp. 2794–2805. DOI: 10.1093/mnras/stv2633. arXiv: 1507.08353 [astro-ph.SR].

Yang, Haifeng et al. (Nov. 2017). "Scattering-produced (sub)millimetre polarization in inclined discs: optical depth effects, near-far side asymmetry and dust settling". In: *Monthly Notice of Royal Astronomical Society* 472(1), pp. 373–388. DOI: 10.1093/mnras/stx1951. arXiv: 1705.05432 [astro-ph.SR].

Yang, Haifeng et al. (Feb. 2019). "Does HL Tau disc polarization in ALMA band 3 come from radiatively aligned grains?" In: *Monthly Notice of Royal Astronomical Society* 483(2), pp. 2371–2381. DOI: 10.1093/mnras/sty3263. arXiv: 1811.11897 [astro-ph.SR].

Youdin, Andrew N. and Jeremy Goodman (Feb. 2005). "Streaming Instabilities in Protoplanetary Disks". In: *The Astrophysical Journal* 620(1), pp. 459–469. DOI: 10.1086/426895. arXiv: astro-ph/0409263 [astro-ph].

Youdin, Andrew N. and Frank H. Shu (Nov. 2002). "Planetesimal Formation by Gravitational Instability". In: *The Astrophysical Journal* 580(1), pp. 494–505. DOI: 10.1086/343109. arXiv: astro-ph/0207536 [astro-ph].

Zapata, Luis A. et al. (Jan. 2012). "Millimeter Multiplicity in DR21(OH): Outflows, Molecular Cores, and Envelopes". In: *The Astrophysical Journal* 744(2), 86, p. 86. DOI: 10.1088/0004-637X/744/2/86. arXiv: 1109.3153 [astro-ph.GA].

Zapata, Luis A. et al. (Jan. 2015a). "Kinematics of the Outflow from the Young Star DG Tau B: Rotation in the Vicinities of an Optical Jet". In: *The Astrophysical Journal* 798(2), 131, p. 131. DOI: 10.1088/0004-637X/798/2/131. arXiv: 1411.0173 [astro-ph.SR].

Zapata, Luis A. et al. (Sept. 2015b). "Origin and Kinematics of the Eruptive Flow from XZ Tau Revealed by ALMA". In: *The Astrophysical Journal Letters* 811(1), L4, p. L4. DOI: 10.1088/2041-8205/811/1/L4. arXiv: 1509.00316 [astro-ph.SR].

Zhang, Shangjia et al. (Dec. 2018). "The Disk Substructures at High Angular Resolution Project (DSHARP). VII. The Planet-Disk Interactions Interpretation". In: *The Astrophysical Journal Letters* 869(2), L47, p. L47. DOI: 10.3847/2041-8213/aaf744. arXiv: 1812.04045 [astro-ph.EP].

Zhu, Zhaohuan and James M. Stone (Nov. 2014). "Dust Trapping by Vortices in Transitional Disks: Evidence for Non-ideal Magnetohydrodynamic Effects in Protoplanetary Disks". In: *The Astrophysical Journal* 795(1), 53, p. 53. DOI: 10.1088/0004-637X/795/1/53. arXiv: 1405.2790 [astro-ph.SR].

Zhu, Zhaohuan et al. (Apr. 2014). "Particle Concentration at Planet-induced Gap Edges and Vortices. I. Inviscid Three-dimensional Hydro Disks". In: *The Astrophysical Journal* 785(2), 122, p. 122. DOI: 10.1088/0004-637X/785/2/122. arXiv: 1308.0648 [astro-ph.EP].

Zhu, Zhaohuan et al. (June 2019). "One Solution to the Mass Budget Problem for Planet Formation: Optically Thick Disks with Dust Scattering". In: *The*

Astrophysical Journal Letters 877(2), L18, p. L18. DOI: 10.3847/2041-8213/ab1f8c. arXiv: 1904.02127 [astro-ph.EP].

Zsom, A. et al. (Apr. 2010). "The outcome of protoplanetary dust growth: pebbles, boulders, or planetesimals? II. Introducing the bouncing barrier". In: *Astronomy and Astrophysics* 513, A57, A57. DOI: 10.1051/0004-6361/200912976. arXiv: 1001.0488 [astro-ph.EP].

Zsom, A. et al. (Oct. 2011). "The outcome of protoplanetary dust growth: pebbles, boulders, or planetesimals?. III. Sedimentation driven coagulation inside the snowline". In: *Astronomy and Astrophysics* 534, A73, A73. DOI: 10.1051/0004-6361/201116515. arXiv: 1107.5198 [astro-ph.EP].